学位論文

X-ray Studies of Highly Magnetized Neutron Stars in Binary Systems with *Suzaku*

(連星をなす強磁場中性子星の「すざく」衛星による X 線観測)

平成 26 年 12 月博士（理学）申請

東京大学大学院理学系研究科

物理学専攻

笹野　理

Abstract

Magnetic field strengths of neutron stars can be estimated from the pulse periods and period derivatives of rotation-powered objects, or through detection of Cyclotron Resonance Scattering Features (CRSFs) in accretion-powered objects. The measured field values are distributed widely, from 10^8 G to 10^{15} G with three prominent peaks; at $\sim 10^8$ G (millisecond pulsars and low-mass X-ray binaries), $\sim 10^{12}$ G (ordinary radio pulsars and binary X-ray pulsars), and $\sim 10^{15}$ G (magnetars). However, the origin of the tree peaks is unknown, and it is not clear, either, whether the gap between 10^{13} and 10^{14} G is real or due to selection effects.

To clarify the nature of the above distribution gap, we analyzed 42 data sets of a sample of 25 binary X-ray pulsars (BXPs), acquired with the *Suzaku* observatory over its $\sim$ 10 years of continuous operation in orbit. The sample consists of 7 Be-type binaries, 8 objects with OB-supergiant primaries, 5 having low-mass companions, and 5 Long-Period Pulsars (LPPs) that are defined as those with pulse periods $> 10^3$ sec. Although many of these objects exhibit CRSFs, the CRSF detection is still missing in 1, 2, 2, and all 5 sources of these subcategories, respectively. The data are all available from the archive, and allowed us to study broad-band (1-100 keV) properties of the sample BXPs from various aspects including the luminosity, pulse profiles, spectral continuum shapes, and the Fe line properties.

From the analysis, the 5 LPPs were found to differ from the others in several aspects, including their considerably lower luminosity, weaker energy dependence of their pulse fraction, much flatter and harder spectra with two broad peaks (at 20 keV and 80 keV), and more spherical matter distribution around them as indicated by the behavior of their Fe-K line equivalent width. We also calibrated how various properties of the CRSF-detected BXPs depend on their magnetic field strengths, and found that major properties of the LPPs can be explained *empirically* by extrapolating these dependences towards stronger magnetic field to $\sim 10^{13}$ G. In such a strong magnetic field, Alfven radius becomes larger than the Bondi radius, so that the stellar wind capture becomes intrinsically suppressed. Conversely, starting from this simple condition, the essential properties of LPPs can be all explained consistently and in a natural way.

Since the 5 objects in our sample represent a major fraction of the presently known LPPs, it is inferred that LPPs generally have a stronger magnetic fields, 10^{13} G or higher, and fill up the gap between 10^{13} and 10^{14} G. We therefore conclude that the distribution gap is caused mainly by the selection effect, arising from the difficulty of detecting LPPs which are intrinsically low-luminosity objects. We also discussed a scenario which describes that magnetars and LPPs are both born with 10^{15} G magnetic fields, but evolve under their different environment to acquire their different observational appearance.

Contents

List of Figures

List of Tables

Chapter 1

INTRODUCTION

Since the first discovery in 1967 (HEWISH et al. 1968), about 10^4 neutron stars (NSs) have been catalogued so far. Their study provides a unique opportunity to investigate physics of high-density nuclear matter, and to clarify various high-energy astrophysical phenomena. In this respect, the important quantities of NSs are not only their masses and radii, but also their magnetic field strength, B. The most dominant NS population, radio pulsars, have magnetic fields distributed over $B = 10^8 - 10^{13}$ G, with a strong concentration at 10^{12} G, as determined from their pulse periods and period derivatives assuming rotational energy loss via magnetic dipole radiation.

Another important population of NSs is binary X-ray pulsars (hereafter BXPs), each consisting of a strongly magnetized NS and a mass-donating star, and emits X-rays via mass accretion. Through X-ray observations over the past half a century, about 50 BXPs have been found (Giacconi et al. 1971). The magnetic fields of BXPs can be determined very accurately, utilizing a spectral feature called "Cyclotron Resonance Scattering Feature" (CRSF), which arise at an X-ray energy of $E_{\rm cycle} = 11.6 \times B/(10^{12}$ G) keV due to the cyclotron motion of electrons. As first discovered by Truemper et al. (1978) from Her X-1, and then from many more BXPs with the Japanese *Ginga* mission (Makishima et al. 1999), CRSF are now confirmed from about 20 BXPs, at energies of 10-70 keV. Although this translates to a rather narrow field distribution over B=(1-6)$\times 10^{12}$ G, X-ray observations revealed the presence of yet another NS population called magnetars (Duncan & Thompson 1992). These are isolated NSs, which are considered to have extremely strong fields as B=10^{14-15} G and emit X-rays by consuming these huge magnetic energies.

Figure 1.1 summarizes the most up-to-date results of the magnetic-field measurements of NSs as described above. Thus, the B distribution has three clear peaks, at 10^8, 10^{12}, and 10^{15} G, of which the origin of these peaks is not yet understood. Although the high field end of the radio pulsar distribution (blue) extends to $\sim 10^{14}$ G, X-ray emitting NSs exhibit a clear gap between $\sim 10^{12}$ G (red; BXPs with CRSFs) and 10^{14-15} G (green; magnetars). At present we do not

know whether this apparent gap in the X-ray band is real, or simply caused by a selection effect that the detection of CRSF becomes difficult at >100 keV due to the decreasing source flux and poorer detection sensitivity. In the present thesis, we observationally address the possibility whether the distribution gap between B=10^{12} and B=10^{15} is due to observational selection effects. More specifically, we investigate whether NSs with B~10^{13} G lurk among those BXPs (about 50%) of which the value of B is still unknown because their lack of detectable CRSFs in energies from a few keV to ~100 keV.

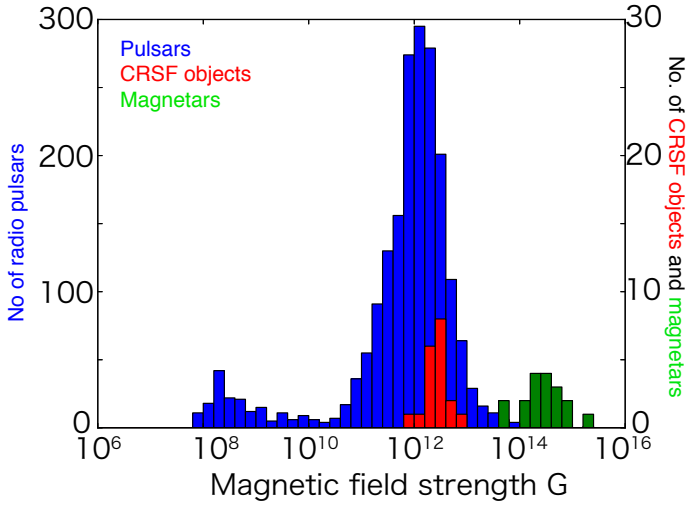

Figure 1.1: Distributions of NS magnetic field strengths. Blue one means radio pulsars, red one CRSF objects and green magnetars (ATNF database).

For the above purpose, we utilize the archival data of BXPs from the *Suzaku* Observatory. This is based on the following three reasons. First, we can study wide-band (1-100 keV) spectra of BXPs, with the two onboard detectors, the X-ray Imaging Spectrometer (XIS) and the Hard X-ray Detector (HXD). Their combined use will allow us to accurately quantify the wide-band spectral shapes of BXPs, and to study the CRSFs mainly using the HXD. Second, the XIS provides a good energy resolution in soft X-rays (<10 keV), and enable the study of Fe-K emission lines 6-7 keV. Third, through its operation for nearly a decade since its launch in 2005 July, *Suzaku* has so far observed about 30 BXPs, and accumulated the data in its archive.

In the present study, we analyze 42 data sets of the 25 BXPs in a unified way, from various aspects including the luminosity, pulse period, pulse shapes, continuum spectra, and the Fe-K line properties. Among the BXPs, Long Period Pulsars (LPPs), characterized by long (> 10^3) pulse periods, are of particular importance as promising candidates for objects with B~10^{13} G. In these studies, the already confirmed CRSFs are utilized as an important fiducial to calibrate how various properties of BXPs depend on B. Finally, considering the results of these data analyses, we attempt to deepen our understanding of the distribution of magnetic field strengths of NSs.

Chapter 2

REVIEW

2.1 Review of Neutron Stars

2.1.1 An over view of NSs

Historically, neutron stars (NSs) have been discovered by radio observation in 1967 (HEWISH et al. 1968). NSs are though to be born when high-mass stars which experienced CNO-cycle and have formed on Fe core collapse due to gravity, producing so called "Type-II supernova". Most masses are blown out by supernova, to produce diffuse energetic structure which are observed as supernova remnants (SNRs) while the remaining masses become NSs or black holes. Actually, some NSs are associated with SNRs, and this fact provides clear evidence for the birth of NSs in supernovae.

Theoretically, masses $M_{\rm NS}$ and radii $R_{\rm NS}$ of NSs are predicted. In the simplest case, we assume that ideal degenerate gas of fermions construct a NS, wherein the temperature is zero and pressure is generated by degeneration. Assuming spherical symmetry, $M_{\rm NS}$ and $R_{\rm NS}$ are then estimated as $\sim$10 km and 1.4 $M_\odot$ ($M_\odot$ being the solar mass), respectively. However, the current accuracies of the $M_{\rm NS}$ and $R_{\rm NS}$ measurements are not yet high enough to distinguish subtle differences in the $M_{\rm NS}$-$R_{\rm NS}$ relation depending on different equations of state of nuclear matter.

As aother parameter of NSs, we consider pulse period $P_{\rm s}$. Actually, NSs that have so far been discovered show pulsations, and are called pulsars. Their $P_{\rm s}$ are roughly limited by a balance between gravity and centrifugal force at the NS surface and the necessary is written as

$$R_{\rm NS}\left(\frac{2\pi}{P_{\rm s}}\right)^2 < \frac{GM_{\rm NS}}{R_{\rm NS}} \tag{2.1}$$

where G is gravitational constant. Considering the typical values of the mass and radius, 2.1

yields $P_s > 0.5$ ms. The fastest spinning NS known to date have P_s=1.5 ms, whereas mass-accreting NSs generally have longer P_s, up to 10^4 s, because of (negative or positive) accretion torques.

The magnetic field strength B is also a very important information of NS. Magnetic field strengths of the Sun has been measured precisely with the Zeeman effects, and the results typical indicate $B \sim$1 kG locally, and $B \sim 100$ G globally. From this, we can roughly calculate B of NSs assuming the conservation of magnetic flux. Assuming that a progenitor star with a radius $\sim R_\odot$ and dipole field ~ 100 G collapses into a NS of radius $R_{\rm NS} \sim 10$ km, the magnetic field will be compressed to

$$B_{\rm NS} \sim 0.5 \times 10^{12} {\rm G} \ . \tag{2.2}$$

Thus, NSs are expected to have typically $B_{\rm NS} \sim 10^{12}$ G.

Figure 1.1 shows a distribution of B of NSs, measured with several techniques described in §2.1.2. Thus, the values of B are widely distributed from 10^8 to 10^{15} G, forming three peaks at 10^8, 10^{12} and 10^{15} G. The peak at 10^{12} G means that the rough estimation of B with eq. 2.2 is correct. However, the nature of other peaks and the possible two gaps between the peaks are still unclear. While a significant fraction of the measurements in Figure 2.12 have been done in radio frequencies, X-ray observations also provide important information on NSs and their magnetism. Weakly magnetized (10^{8-10} G) NSs with mass-donating companion stars, i.e., system called Low-Mass X-ray Binaries (LMXBs), have been observed extensively in X-rays. When NSs with $B \sim 10^{12}$ G form binaries with (mainly massive) companions, the system become Binary X-ray Pulsars (BXPs). They exhibit clear pulsations, and often cyclotron resonance scattering features (CRSFs) in their X-ray spectra. Below, we classify the NS as isolated, LMXBs and BXPs, and review their properties.

2.1.2 Isolated neutron stars

Isolated NS are observed mainly in the radio band, and their P_s have been measured accurately. As shown in Figure 2.1, the values of P_s measured from NSs are all above the limit of eq. 2.2, and are distributed widely, from 10^{-3} to 1 s. Although the value of P_s of each NS is relatively constant, it can vary with both signs (spin up and spin down). As shown in Figure 2.1, the rate of period change is typically $\dot{P}_s \sim 10^{-15}$ s s^{-1}, with a distribution from 10^{-21} to 10^{-9} s s^{-1}.

With P_s and $\dot{P}_s$, we can estimate the dipole magnetic field strength B. When a magnetized objects is accelerated, electromagnetic waves via magnetic dipole radiation, with a luminosity L of

$$L = \frac{2}{3c^3} |\ddot{\boldsymbol{m}}|^2 \tag{2.3}$$

in tedms of the second order derivative of the magnetic dipole momentum $\boldsymbol{m}$. Here, cgs-Gauss unit is employed. Considering a rotating pulsar with P_s, $|\boldsymbol{m}|$ is expressed as $\frac{1}{2} B R_{\rm NS}^3$, and hence

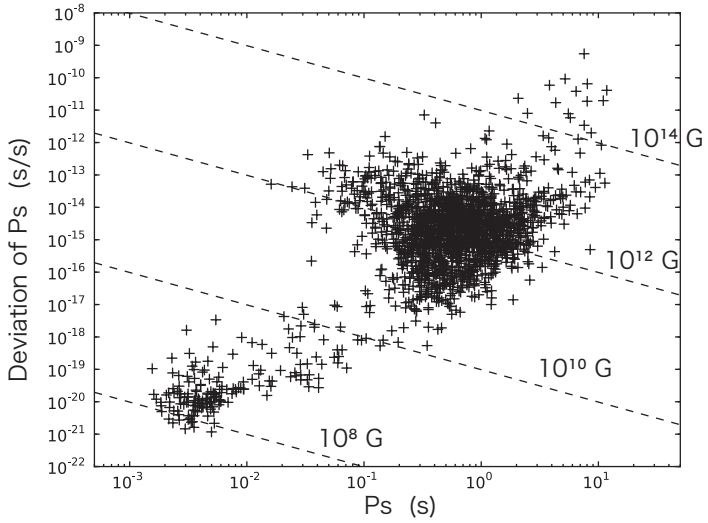

Figure 2.1: $P_{\rm s}$-$\dot{P}_{\rm s}$ diagram for radio pulsars plotted from the ATNF data-base.

L is described as

$$L = \frac{2}{3c^3} \cdot \left(\frac{1}{2} B R_{\rm NS}^3\right)^2 \cdot \left(\frac{2\pi}{P_{\rm s}}\right)^4 \quad . \tag{2.4}$$

On the other hand, the rotational energy of the NS is given as

$$E_{\rm rot} = \frac{1}{2} I \cdot \left(\frac{2\pi}{P_{\rm s}}\right)^2 \tag{2.5}$$

where I is the moment of inertia. Therefore, the decrease of $E_{\rm rot}$ is written as

$$L_{\rm rot} = -\frac{dE_{\rm rot}}{dt} = 4\pi^2 I P_{\rm s}^{-3} \dot{P}_{\rm s} \quad . \tag{2.6}$$

Assuming 2.4 equals to 2.6, we are able to estimate B as

$$B = \left(\frac{3c^3}{2\pi^2}\right)^{1/2} \left(\frac{I}{R_{\rm NS}^6}\right) (P_{\rm s}\dot{P}_{\rm s})^{1/2} \quad . \tag{2.7}$$

The dashed lines in Figure 2.1 give the values of B of radio pulsars calculated via eq. 2.7. Indeed, a majority exhibit $B \sim 10^{12}$ G, thus forming the highest peak in Figure 1.1.

In Figure 2.1, some objects show long $P_{\rm s}$ (1-10 s) and large $\dot{P}_{\rm s}$ (10^{-12}-10^{-9} s s^{-1}). They hence have very strong fields as B=10^{14-15} G, and are called "magnetars" (Duncan & Thompson 1992). Sometimes, magnetars occur short burst ($L \sim 10^{38}$ erg s^{-1}) and giant flares ($L \sim 10^{44}$ erg s^{-1}). Although they are plotted in Figure 2.1 together with radio pulsars, the radiate predominantly in X-rays. Their X-ray luminousities are higher than those of typical radio pulsars, and are event exceeding their spin-down luminosity of eq. 2.6. Therefore, the source energy of

their emission is considered as magnetic field.

2.1.3 Neutron stars with low-mass companion stars (LMXBs)

In binary systems involving NSs, the energy source of radiations is the gravity. In such a system, matters transferred from the companion star emits X-rays while accreting onto the NS. The mass of the star makes difference to mechanism of the accretion. In an LMXB (i.e., a binary composed of a low-mass star and an NS), the two components are so close to each other that the gravitational potential has a structure as we calculated and show in Figure 2.2. If radius of the star becomes larger than the separatrix which is called Roche lobe, the mass transfer occur persistently. The Roche-lobe radius is approximately specified by the stellar mass $M_{\rm s}$ and, the NS $M_{\rm NS}$, the mass ratio $q = M_{\rm NS}/M_{\rm s}$, and the orbital period $P_{\rm orb}$ as

$$R_{\rm R} = \frac{0.49q^{2/3}}{0.6q^{2/3} + ln(1+q^{1/3})} \cdot \left(\frac{G \cdot (M_{\rm NS} + M_{\rm s})}{4\pi^2}\right)^{1/3} \cdot P_{\rm orb}^{2/3} \quad . \tag{2.8}$$

Considering their typical values, $M_{\rm NS}$=1.4 $M_{\odot}$, $M_{\rm s}$=0.5$M_{\rm odor}$, and $P_{\rm orb}$=10 hr, eq. 2.8 gives $R_{\rm R} \simeq 0.8R_{\odot}$. This mode of mass transfer is called ,“Roche-lobe overflow”, and is considered to lead to the formation of an accretion disk around the NS.

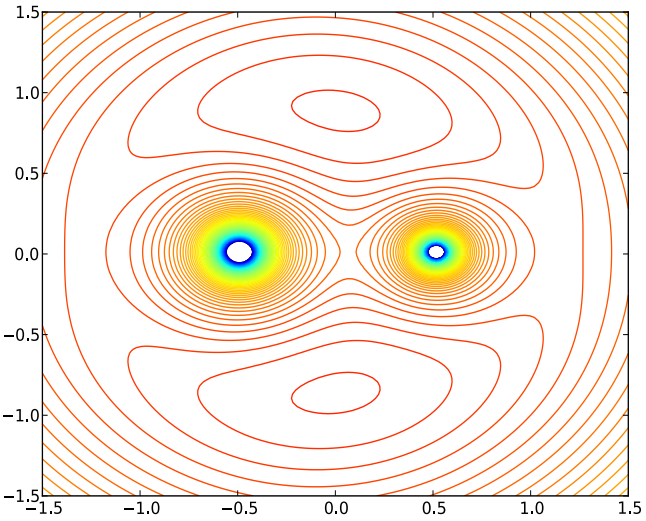

Figure 2.2: Contour map of the potential in a close binary system.

Generally, LMXBs are old systems from the life times of the stars. Since NSs in such systems should be old as well, their B is considered to have decayed to 10^{8-10} G. In reality, B of NSs in LMXBs cannot be measured directly and it is difficult to evaluate their B in most cases. This is because we are not able to apply eq. 2.7 to mass-accreting systems in which $P_{\rm s}$ and $\dot{P}_{\rm s}$, are affected by the accretion torque. However, several indirect pieces of evidence support

their weak-field nature: the X-ray pulsation has been detected only from a minor fraction of LMXBs, and such cases, the detected periods are very short, $P_s \sim 10$ ms, which are close to those of "millisecond radio pulsars" located at the bottom-left corner of Figure 2.1.

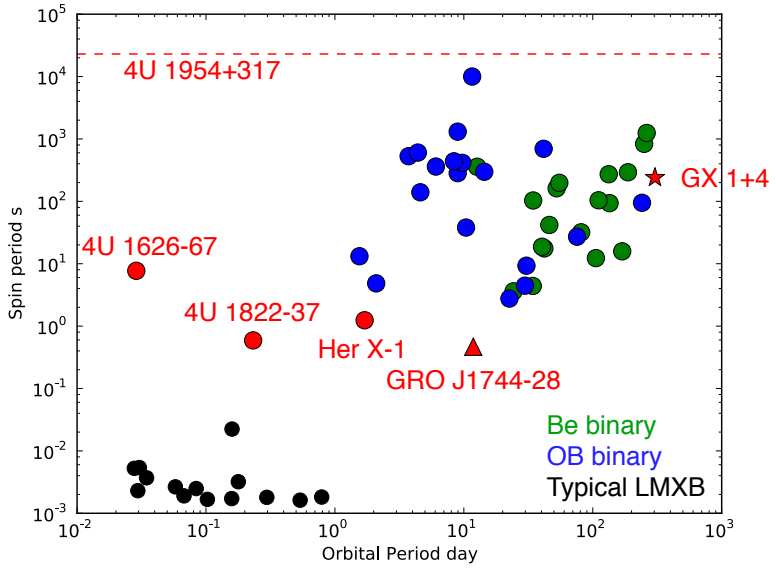

Figure 2.3: P_{orb}-P_s diagram (so-called Corbet diagram) of LMXBs and BXPs.

As shown in Figure 2.4, many LMXBs show large flares in X-ray, so called X-ray bursts, wherein the X-ray intensity rises in 2 s and decay, in ~50 s. These events are thought to arise when a certain amount of hydrogen and helium, accumulated on the NS surface, make unstable nuclear fusion. Actually, the time-average burst luminosity of an LMXB is ~1/100 of its persistent luminosity, in agreement with the ratio of nuclear to gravitational energies of nucleons. In Figure 2.4, the hard X-ray intensity falls more rapidly, reflecting cooling after the nuclear flash.

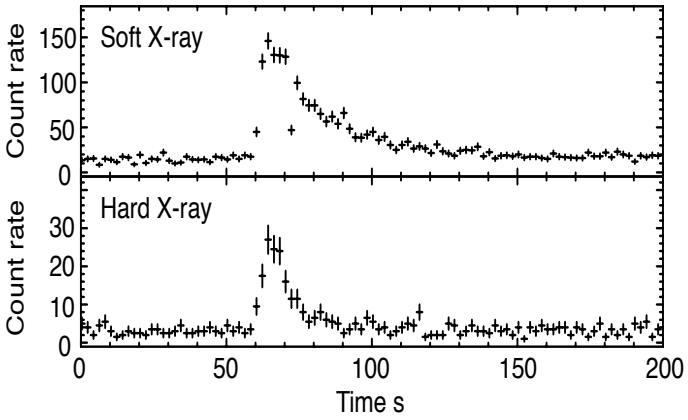

Figure 2.4: An X-ray burst from 4U 1705−44 detected with *Suzaku*, In a soft X-ray band (top; 1-10 keV) and hard X-ray band (bottom; 15-60 keV).

In LMXBs, a few objects, Her X-1, 4U 1626−67, 4U 1822−37, GRO J1744−28 ,GX 1+4,

and 4U 1954+317 have strong B exceptionally. Especially, B of Her X-1, 4U 1626-67, and 4U 1822−37 have been measured with CRSFs. Their features including P_s and X-ray spectra are similar to those of BXPs. Their P_s are typically ∼1 s and much longer than 10 ms, typical P_s of LMXBs. As described in §2.3.3, BXPs have long P_s, 1-1000 s and they are similar to those of the five objects. In the case of GX 1+4, type of the primary star is M type star and binary systems with M-type star are called symbiotic X-ray binaries (SyXBs). They are different from other LMXBs because Roche-lobe over flow does not occur in SyXBs. In the systems, accretions to NSs occur by wind capture described in §2.1.4 and they are close to BXPs. In Figure 2.3, we show P_{orb} and P_s diagram, so called "Corbet-diagram". On the diagram, the six objects are clearly different from typical LMXBs

2.1.4 Binary systems of neutron star and high-mass stars

In most cases, BXPs have massive ($> 10M_\odot$) primary stars with spectral types of O and B, and their orbital separations and P_s are longer than those of LMXBs (Figure 2.3). From e.q.2.8, these massive primaries are considered to fill their Roche lobes. Therefore, their gasses can not be transferred to the NS via Roche-lobe overflow. Instead, these massive stars launch dense stellar winds, which the NS can capture as illustrated in Figure 2.5. The mass transfer mechanisms is clearly different between LMXBs and high-mass BXPs. The amount of mass which is blown out by the high-mass star, so called mass-loss rate, is typically $\sim 10^{-6}$ s yr^{-1}. The mass accretion rate $\dot{M}$ onto the NSs depends on the mass-loss rate of the star, and the relative wind velocity as seen from the NS. Considering a balance of the gravity of the NS and kinetic energy of the winds, namely

$$\frac{1}{2}(v_w^2 + v_{NS}^2) = \frac{GM_{NS}}{r_B} \tag{2.9}$$

where v_w is the wind velocity and v_{NS} is the velocity of the NS motion. we can evaluate a radius from the NS within wind which are captured by the NS, so called Bondi-radius r_B, as

$$r_B = \frac{2GM_{NS}}{v_w^2 + v_{NS}^2} \quad . \tag{2.10}$$

Since v_w is of the order of 1000-2000 km s^{-1} and v_{NS} is considerably lower, r_B is estimated as $\sim 10^{10}$ cm. The mass accretion rate is described with r_B, v_w, and density of the winds ρ_w as

$$\dot{M} = \pi r_B^2 \rho_w v_w \quad . \tag{2.11}$$

Since the stellar winds are generally inhomogeneous ρ_w, $\dot{M}$ fluctuates largely, thus making BXPs with massive primaries highly time variable.

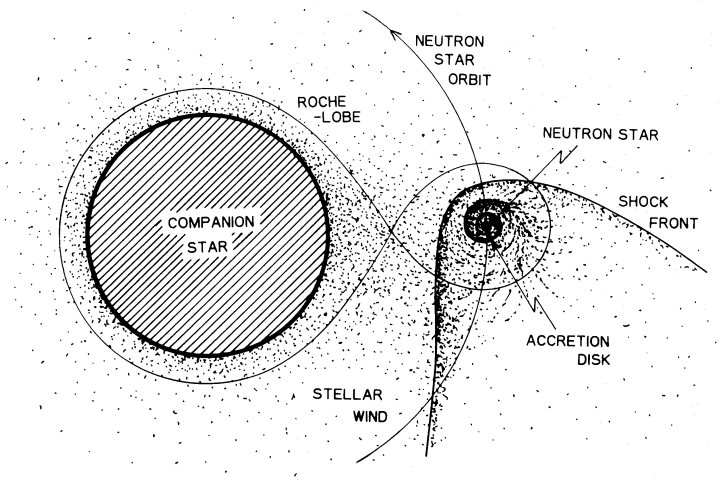

Figure 2.5: A schematic view of the capture of stellar winds from a high-mass companion by an NS (Nagase 1989).

Some B-type stars show optical emission lines and are classified as Be star. They are different from other O or B-type stars, because they have circumstellar disks which emit the lines. About ~30% of the currently known BXPs actuallyy have Be-type primaries, and are known as "Be binaries". As shown in Figure 2.3, their $P_{\rm orb}$ are longer than those of O,B-type binaries, and their eccentricities are large (> 0.3). In these systems, $\dot{M}$ is very low when the NS is far from the primary star. When the NS passes through circumstellar disk near the periastron, $\dot{M}$ goes up and a large flare, so called X-ray outburst, takes place. In Figure 2.6, we show a long-term light curve of a Be binary. Thus, it produces strong X-ray outbursts synchronized with $P_{\rm orb}$, while it is very faint (usually below the detection limit) when it is away from the periastron.

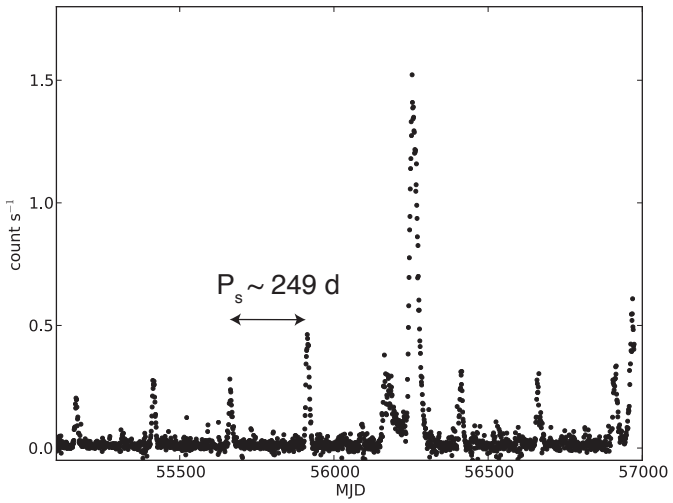

Figure 2.6: An example long-term light curve of the Be binary system, GRO J1008−57, obtained by MAXI-GSC in 2 to 20 keV (from the *MAXI* Website http://http://maxi.riken.jp/).

Most of BXPs are considered to have strong magnetic fields, $B \sim 10^{12}$ G, because they show (by definition) strong pulsations: As seen in Figure 2.3, the have considerably longer $P_{\rm s}$ than LMXBs, because they receive stronger torque from the accreting matter through the stronger magnetic field lines. A more direct support to the strong magnetization of the NSs can be provided by electron-cyclotron resonance features, described in §2.3.2. The strong B is consistent with the youth of these systems, because the stellar life time shortens as $\sim M^{-2.5}$ with the mass M.

2.2 X-rays from Accreting Neutron Stars

As described in §2.1.1, radii of NSs are very small, $\sim 10^6$ cm, and the gravitational potential at the surface of NSs is very deep. When electrons and protons fall onto the NS surface, they release an energy of ~100 keV and 200 MeV each, respectively. Near the NS surface, accreting matters becomes hot enough to emit in the X-ray or γ-ray. The X-ray bolometric luminosity of an accreting NS, written as

$$L_{\rm X} = \frac{GM_{\rm NS}\dot{M}}{R_{\rm NS}} \ , \tag{2.12}$$

typically becomes $\sim 10^{36-37}$ erg s^{-1}. Thus, L is considered to be directly proportional to $\dot{M}$.

As L becomes higher, the radiation pressure increase. At certain L, the radiation pressure equals to gravity and the accretion stops. The L is called Eddington luminosity, $L_{\rm Edd}$, and is calculated as

$$L_{\rm Edd} = \frac{4\pi c G M_{\rm NS} m_p}{\sigma_{\rm T}} \tag{2.13}$$

where $m_{\rm p}$ and $\sigma_{\rm T}$ are the proton mass and the Thomson cross section, respectively. $L_{\rm Edd}$ ~2×10^{38} erg s^{-1} for the typical value of $M_{\rm NS} \sim 1.4 M_\odot$.

Accreting neutron stars emit many energy X-ray photons over a broad energy band, so that the observed X-ray spectra include rich information. In Figure 2.7, we show *Suzaku* spectra of LMXBs in the soft (black) and hard (red) state, and that of a typical BXP (blue). Thus, LMXBs show clear state transitions, involving drastic spectral shape changes. The spectrum takes soft thermal shape because the matter is radiatively cooled while that in the hard state extends to ~100 keV, as a result of thermal Comptonization by hot accretion coronae. The transitions are caused by changes in the accretion geometry near the NS. Spectra of BXPs are clearly different from those of LMXBs.

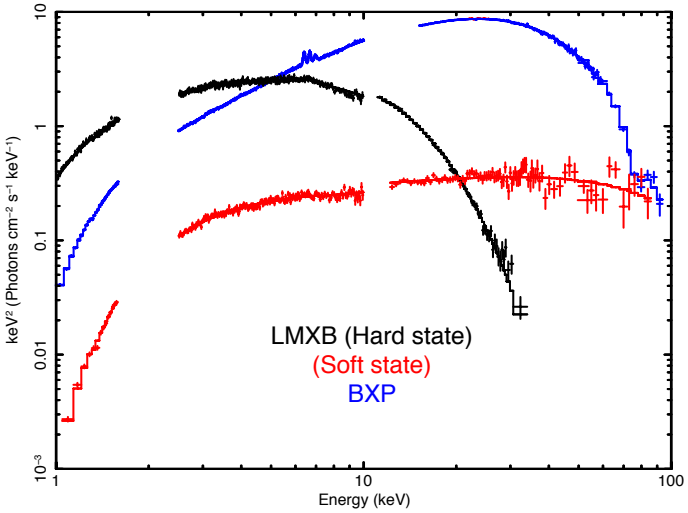

Figure 2.7: X-ray spectra in $\nu F\nu$ form obtained from three NS binaries with *Suzaku*. black ones are those of LMXB with soft state, red ones LMXB with hard state, and blue one BXP.

2.3 Properties of Strongly Magnetized Neutron Stars in Binaries

2.3.1 X-ray spectra

In a close binary system involving a strongly magnetized NS, matters from the companion star accretes along the field lines to the NS surface. Near the surface of the NS, the matters are squeezed by the magnetic fields and form accretion column as shown in Figure 2.8. In the accretion column, matters falls with high velocities, ∼20% of the light speed, and shock occurs at a certain height as described in Figure 2.8. The electron temperature in the column becomes as high as ∼10 keV, and the density is also very high ($n_{\rm e}$∼10^{22} cm^{-3}). As a results, X-ray photons are emitted with bremsstrahlung and other processes.

Since an accretion column has a typical size of $r \sim 1$ km, its optical depth for the Thomson scattering becomes $\tau \sim n_{\rm e} r \sigma_{\rm T} \gtrsim 1$. Therefore, photons in an accretion column will be strongly Compton-scattered by electrons, which have both high bulk and random (thermal) motions. The process of inverse-comptonization is presented by the Kompaneets equation. In terms of the photon distribution function f, the electron density n_e, and the electron temperature T_e, the equation is written as

$$\frac{\partial f}{\partial t} = \left[n_e \sigma_{\rm T} c \left(\frac{k T_e}{m_e c^2} \right) \right] \frac{1}{x^2} \frac{\partial}{\partial x} \left\{ x^4 \left(\frac{\partial f}{\partial x} + f + f^2 \right) \right\} \tag{2.14}$$

where x ≡ $h\nu/m_e c^2$ is the means photon energy in units of the electron rest-mass energy. Under the steady-stat condition, the left hand side of eq. 2.14 vanishes and f becomes the Bose-Einstein distribution as

$$f = \frac{1}{\exp(x + \mu) - 1} \tag{2.15}$$

where μ is a constant corresponding to the chemical potential. Because the Compton scattering conserves the photon number, the distribution is approximated by a classical Boltzman distribution as Approximately,

$$f \propto \exp\left(-\frac{h\nu}{m_e c^2} \right) \ . \tag{2.16}$$

Then, the emitted photon flux density is given as

$$I_\nu \propto (h\nu)^2 \exp\left(-\frac{h\nu}{m_e c^2} \right) \ , \tag{2.17}$$

which is called Wien hump.

X-ray spectra of BXPs are generally more complicated than can be reproduced by eq. 2.17. As an empirical model for the spectra, Negative-Positive EXponential cutoff power-law

(**NPEX**) has been adopted. The model has two power-law components with a common cutoff factor as

$$\mathrm{NPEX} = \left[N_p \cdot E^{\Gamma_\mathrm{p}} + N_n \cdot E^{-\Gamma_\mathrm{n}}\right] \exp\left(-\frac{E}{kT}\right) \tag{2.18}$$

where Γ_p and Γ_n are photon indices of positive and negative components, respectively, and $E \equiv h\nu$ is the emitted photon energy. From Eq. 2.17, Γ_p is generally fixed to 2.0 to reproduce the Wien hump. In the case of $\nu F\nu$ spectra, eq. 2.19 is rewritten as

$$\mathrm{NPEX}_{\nu F\nu} = \left[N_p \cdot E^{2+\Gamma_\mathrm{p}} + N_n \cdot E^{2-\Gamma_\mathrm{n}}\right] \exp\left(-\frac{E}{kT}\right). \tag{2.19}$$

The intrinsic validity of this model have been confirmed by Odaka et al. (2013) and Odaka et al. (2014) via Monte-Carlo simulations.

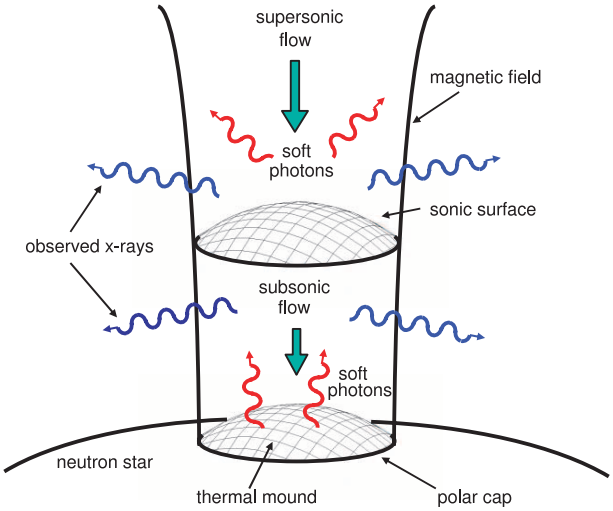

Figure 2.8: A schematic picture of an accretion column on the NS surface (Becker et al. 2012).

In low energies (< 3 keV), X-ray photons are absorbed by interstellar medium (ISM), as well as local stellar gas in a binary system. Heavy elements, C, N, O, Ne, Mg, and Fe, contribute to the absorption because they have large cross sections against X-rays. Although H and He has much smaller cross section, the attenuation due to absorption is usually expressed as $\exp[-N_\mathrm{H}\sigma(E)]$, where N_H is the equivalent hydrogen column density, while $\sigma(E)$ is photoelectric cross section composed of contributions from various heavy elements, weighed by their abundance. Since the ISM has a typical density of $\sim$1 cm^{-3}, BXPs located at distance of 1-10 kpc are expected to have N_H=(1-10)$\times10^{21}$ cm^{-2}. Locally, NSs are surrounded by dense stellar winds, so that the local column density often exceeds the ISM contribution. In Figure2.9, we show some spectra which are simulated with for different N_H values. Thus, the effects of absorption first appear in lower energies, and proceed to higher energies as N_H increases.

The photoelectric absorption is inevitably followed by emission of fluorescent X-ray lines photons, particularly, K-lines. When the absorption occurs in the line-of-sight ISM, the produced line photons are scattered into 4π steradian, and does not reach us. However, if the

absorber is local to the source, and subtends a large solid angle, the line photons reach us. Actually, from many BXPs, Fe K-α (6.4 keV) and K-β (7.05 keV) lines have been detected in X-ray spectra as shown in Figure2.10(a). The ratio between Fe K-α and K-β line intensities is theoretically $\sim$ 15%, with which observations are consistent.

In some BXP spectra, not only the neutral Fe K-line but also ionized lines have been detected (Ebisawa et al. 1996). In the example of Figure 2.10(b), two lines, namely, Kα lines from helium like (6.7 keV) and hydrogen like (6.93 keV) Fe ions, are clearly detected. Generally, those ionized lines are detected from white dwarfs in binaries. In some X-ray sources, including accreting white dwarfs and stellar coronae, ionized heavy-ion lines are emitted from collision ally ionized plasmas. However, the ionized lines from BXPs are emitted by a different mechanism known as photoionization: strong continuum X-rays photoionize surrounding materials to high ionization states, and these ions recombine with free electrons to emit line photons which have higher energies than the neutral fluorescence line. The effect of photoionization is usually evaluated by so-called ionization parameter ξ, which is written as

$$\xi \equiv \frac{L}{n \cdot r^2} \tag{2.20}$$

where n is the matter density and r is distance between the NS and the matters. As shown in Figure2.11, ξ specifies relative populations of different ionization states of the same element. Particularly, He-like lines appear at ξ>300 and H-like above ~1000. Measuring ξ, we can study n and/or r.

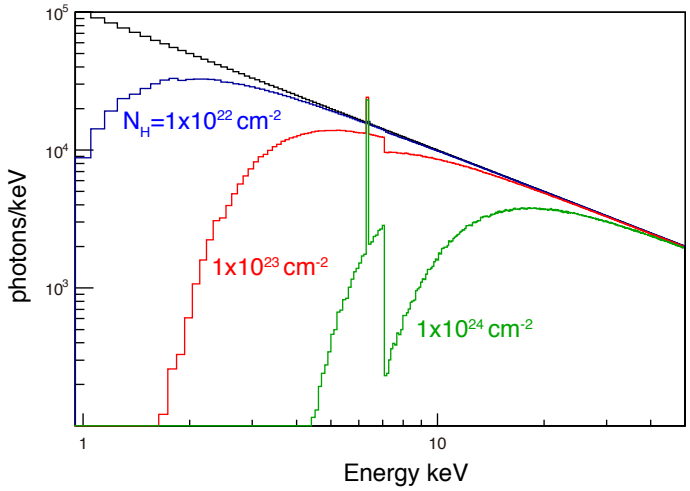

Figure 2.9: Calculated effects of photoelectric absorption on a model spectra (black), which is power-law of photon index 1.0. Blue, red, and green represent the absorption cause by $N_{\rm H}$=1×10^{22}, 1×10^{23}, and 1×10^{24}, respectively. The absorber is assumed to have cosmic abundance.

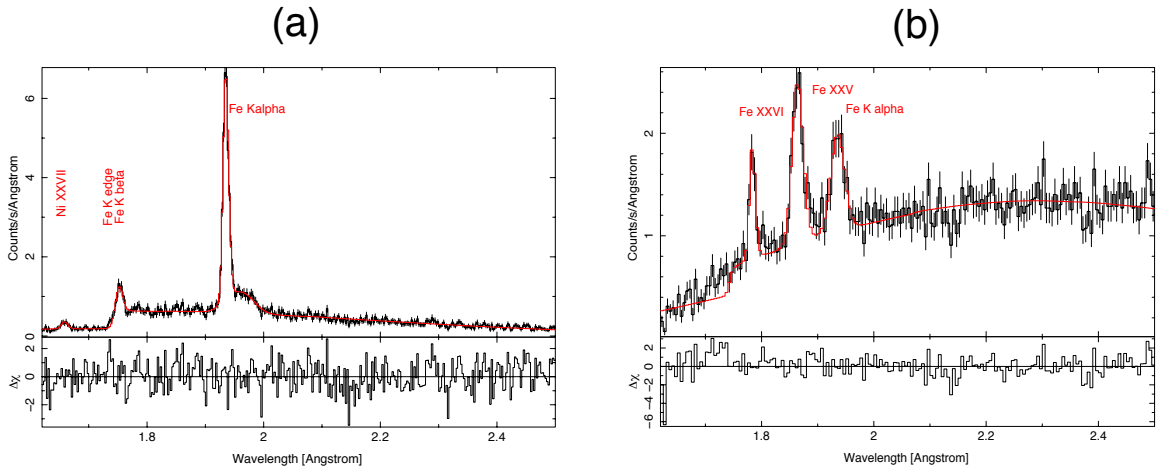

Figure 2.10: Spectra around iron lines obtained by the *Chandra*-HETEG (Torrejón et al. 2010) from GX 301−2 (panel a) and Cyg X-3 (panel b).

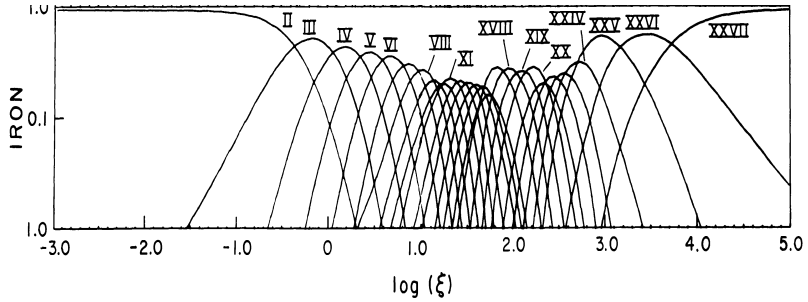

Figure 2.11: Abundance of ionized Fe lines against the ionization parameter ξ (Kallman & McCray 1982).

2.3.2 Cyclotron resonance scattering features

A charged particle in magnetic fields B, the particle is forced by the Lorentz force to rotate around the field lines, with an angular frequency given as

$$\omega = \frac{q \cdot B}{m} \tag{2.21}$$

with m and q are the mass and charge of the particle. This is called cyclotron motion or Larmour motion. When this motion is treated in quantum physics, the kinetic energy of the particle perpendicular to the field lines is quantized into Landau levels, which are written as

$$E_n = \hbar\omega\left(n + \frac{1}{2}\right) \tag{2.22}$$

where n=0,1,2,... is the quantum number. As a result, X-ray spectra are expected to show prominent features (either in absorption or emission) at transition energies among these levels

of electrons, that is,

$$E_{\rm cycl} = \frac{11.6}{(1+z)} \times B_{12} \quad ({\rm keV}) \tag{2.23}$$

and its higher harmonics, where B_{12} is B in unit 10^{12} G, and z is gravitational redshift at the NS surface. This is the concept of CRSF (Cyclotron Resonance Scattering Feature; Makishima et al. 1999), which was already mentioned in §2.1.1. As mention in §2.1.1, BXPs have typically $\sim 10^{12}$ G. Hence from eq. 2.23, their CRSFs are expected to appear at $E_{\rm cycl} \sim 10$ keV, namely, in the hard X-ray band. Therfore, broad-band X-ray observations of BXPs are expected to provide the most accurate measurements of B of a particular subclass of NSs.

The CRSF was first detected from Her X-1 at ∼30 keV in a ballon flight (Truemper et al. 1978, Voges et al. 1982). Then, from 4U 0115+63, a CRSF was found at ∼20 keV (Wheaton et al. 1979), which later turned out to be the second harmonics resonance (White et al. 1983). These pioneering works have established that CRSFs can actually appear in BXP spectra, and in absorption rather than emission. With *Ginga*, CRSFs were discovered by many more BXPs, 4U 1538−52 at ∼22 keV (Clark et al. 1990), X 0331+53 at 28.5 keV(Makishima et al. 1990), Cep X-4 at ∼30 keV (Mihara et al. 1991), 4U 1907+09 at ∼20 keV (Makishima et al. 1999), Vela X-1 at ∼25 keV (Makishima et al. 1999), and GX 301-2 (Mihara 1995). As a result, it have been discovered that the CRSF-measured B of BXP is distributed over a narrow range of (1-7)$\times 10^{12}$ G (Makishima et al. 1999), as presented in Figure 1.1 in red. Further studies of CRSF have been carries out with *BeppoSAX* (e.g., Santangelo et al. 1998 for Cen X-3 at 30 keV and Orlandini et al. 1998 for 4U 1626−67 at 35 keV), *RXTE* (e.g, Heindl et al. 2001 for XTE J1946+274 at 30 keV), and *Suzaku* (Terada et al. 2006 for A 0535+26 at 45 keV, Enoto et al. 2008 for Her X-1 at 70 keV, Suchy et al. 2011 for 1A 1118−61 at 50 keV, and Sasano et al. 2014 for 4U 1822−37 at 30 keV), sometimes in collaboration with *MAXI* (Yamamoto et al. 2011 for GX 304−1 at 50 keV and Yamamoto et al. 2014 for GRO J1008−57 at 70 keV). The resonance energy $E_{\rm cycl}$ has been found to depend to some extent on the luminosity (Nakajima et al. 2006, Nakajima et al. 2010, and Staubert et al. 2007). The strongest B has been detected from GRO J1008−57 at B=7$\times 10^{12}$ G (Yamamoto et al. 2014).

The structure of CRSFs was calculated by many authors (e.g., Meszaros & Nagel 1985), who predicted the presence of higher harmonic features. Actually, higher harmonics have been observed in some objects as shown in Figure 2.12(b). To reproduce the CRSF structure in X-ray spectra, the most appropriate form is so called **cyclabs** model, given as

$$\text{cyclabs} = \exp\left[-D \cdot \frac{(W \cdot (E/E_{\rm cycl}))^2}{((E - E_{\rm cycl})^2 + W^2)}\right] \tag{2.24}$$

where D is the depth and W is the width of CRSF. The factor inside exponential in eq. 2.24 is based on a classical cyclotron resonance formula. Although the CRSF effect has so far been considered to appear all in absorption, Iwakiri et al. (2012) found possible evidence of cyclotron

emission at a particular pulse phase of 4U 1626−67 observed with *Suzaku*.

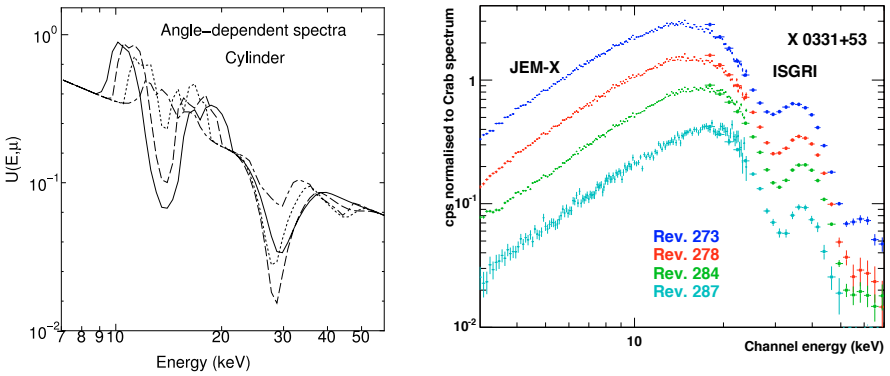

Figure 2.12: (a) Simulation results of CRSF shape by Nishimura (2008). The colors are the same as Figure 5.24. . (b) Observed CRSF in X-ray spectra obtained by *INTEGRAL* (Mowlavi et al. 2006).

2.3.3 X-ray pulsations

Since the X-ray emission of a BXP is considered to arise from the two accretion columns, the X-ray intensity observed from this type of objects periodically change synchronized with the NS rotation. This phenomenon, called X-ray pulsation provides one evidence of strong B. As shown in Figure 2.13, the shapes of pulses vary among BXPs. The pulse profiles depend also on energies and luminosities (Figure 2.13).

As shown in Figure 2.14, periods of the pulsations $P_{\rm s}$ of BXPs distribute widely from 1 s to 10000 s, than those of LMXBs, because their stronger magnetic filed interact with the accretion matter at farther distances from the NS and allows a more efficient angular momentum transfer between the NS and the accreting matter. When the NS has a higher B, the angular momentum transfer occurs at a larger radius, where the Keplerian angular frequency is low, thus causing the NS to have a long $P_{\rm s}$.

We can estimate the point of the angular moment transfer, so called Alfven radius $r_{\rm A}$, based on a balance between magnetic and gas pressures. In terms of the Keplerian gas velocity v and density ρ at distance r from a NS, the balance is described as

$$\frac{B^2(r)}{8\pi} = \frac{1}{2}\rho(r)\cdot v^2(r) \tag{2.25}$$

where the dipole magnetic field outside the NS is related to the magnetic dipole moment μ as

$B{=}\mu \cdot r^{-3}$. Assuming free-fall condition, the velocity and density are described as

$$v(r) = \left(\frac{2GM}{r}\right)^{1/2}$$
$$\rho(r) = \frac{\dot{M}}{4\pi v(r) \cdot r^2} \ , \tag{2.26}$$

respectively. Using eq.2.25 and eq.2.26, the distance r is written as

$$r_{\rm A} = \left(\frac{\mu^4}{2GM\dot{M}^2}\right)^{1/7} , \tag{2.27}$$

and substituting eq.2.12 into eq.2.27 yields

$$r_{\rm A} = \left(\frac{\mu^4 GM}{2L^2R^2}\right)^{1/7} . \tag{2.28}$$

Considering typical luminosities and the NS masss, we obtain

$$r_{\rm A} = 3.5 \times 10^8 \ L_{37}^{-2/7} \mu_{30}^{4/7} \left(\frac{M}{M_\odot}\right)^{1/7} R_6^{-2/7} \quad {\rm cm} \tag{2.29}$$

where L_{37} is the luminosity in units of 10^{37} erg s^{-1}, μ_{30} means the value of μ in units of 10^{30} G cm^{-3} and R_6 is the radius in units of 10^6 cm. The typical Alfven radius becomes $\sim 10^8$ cm.

Since $P_{\rm s}$ is strongly correlated with B as described above, we can predict B to some extent from $P_{\rm s}$. Assuming that the accreting matter, rotates around the NS with the Keplerian velocity, so-called co-rotation radius $r_{\rm co}$ is described as

$$r_{\rm co} = \left(\frac{GM_{\rm NS}}{4\pi^2}\right)^{1/3} \cdot P_{\rm s}^{2/3} = 1.68 \times 10^8 \cdot P_{\rm s}^{2/3} \quad {\rm cm} \ . \tag{2.30}$$

If $r_{\rm A}$ equals to $r_{\rm co}$, i.e., if the NS and the accretion matter is in a torque equilibrium, $P_{\rm eq}$ is estimated as

$$P_{\rm eq} = 3.0 \times L_{37}^{-3/7} \cdot \mu_{30}^{6/7} \ . \tag{2.31}$$

Therefore, a BXP can rotate faster as L increases and B decreases. when we consider the typical NS radius and mass. With the same assumption, alternatively B is estimated as

$$B = 0.25 \times P_{\rm s}^{7/6} L_{37}^{1/2} \times 10^{12} \quad {\rm G} \tag{2.32}$$

This mean that longer-period pulsars can have higher values of B, though depending on the assumption of torque equilibrium.

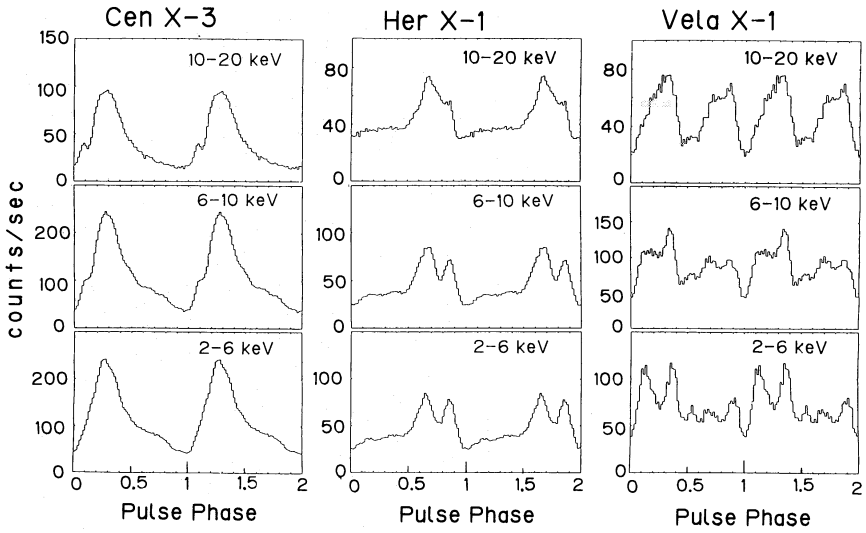

Figure 2.13: Pulse profiles of Cen X-3 (left), Her X-1 (center) and Vela X-1 (right) obtained by *Tenma* (Nagase et al. 1989).

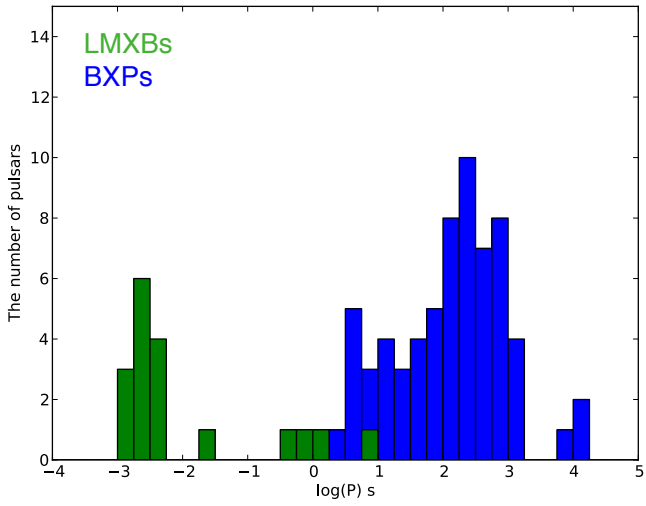

Figure 2.14: The distribution of pulse periods. Green data means P_s of LMXBs and blue ones those of BXPs.

Chapter 3

INSTRUMENTS

3.1 Overview of Suzaku

The fifth Japanese X-ray satellite *Suzaku* carry five X-Ray Telescopes (XRT) and three main detector, the X-Ray Spectrometer (XRS), the X-ray Imaging Spectrometer (XIS), and the Hard X-ray Detector (HXD). *Suzaku* is the biggest among the Japanese X-ray satellites and weights 1706 kg. The satellite was launched on 10 July, 2005, from Uchinoura Space Center (USC) with M5 rocket. It was launched into quasi-circular orbit with altitude ∼560 km and revolves its orbit in 96 min. The orbital inclination is ∼30°. Figure 3.2 shows the particle counts observed in the *Suzaku* orbit. A high count region, the South Atlantic Anomaly (SAA) is evident. Effect of geomagnetic cut-off rigidity is also visible. Since the satellite ceases the observation when passing the SAA and while the target is hidden behind the earth, its typical observing efficiency is ∼46%. Generally, it is contacted 4 or 5 times in a day from USC interval in each contact is ∼15 min and the gross contact time is about 1 hr in a day. After one month from launching, one of the main detector, the XRS, lost helium gas from its dewer and became unusable. However, the other two, the XIS and HXD are in good condition. *Suzaku* have been alive for ∼10 years and observed many types of X-ray sources, which are published as archive data for the most of part.

As shown in Figure 3.1, 4 sets of XRT-I and XIS are onboard and the HXD is mounted next to the XISs. By combining these detectors, *Suzaku* has several advantages of covering wide energy range from 0.5 to 600 keV, good energy resolution at the soft X-ray band, and good sensitivity at the hard X-ray band. The two detectors, the XIS and HXD, cover between 0.5 and 10.0 keV and 10.0 and 600 keV, respectively. As a properties of the XIS, energy resolution ∼160 eV (in FWHM) at ∼ 6 keV is the best score comparing the other X-ray observatories. At the hard X-ray band (10-70 keV), HXD-PIN has the best sensitivity and can detect signals from faint sources. Especially, those advantages in spectroscopy are very effective to study

BXPs because CRSF appear at high energies and multiple iron lines are detectable at 6-7 keV.

Suzaku has two nominal position, XIS nominal and HXD nominal, because the XIS and HXD are misaligned after launching. This is caused by the slight shift in the XRT optical bench and the HXD fine collimator alignment. Effect of this shift is ∼10% decrease in the effective area for each detector which in not in the nominal position. Thus, the default response files are prepared for both positions.

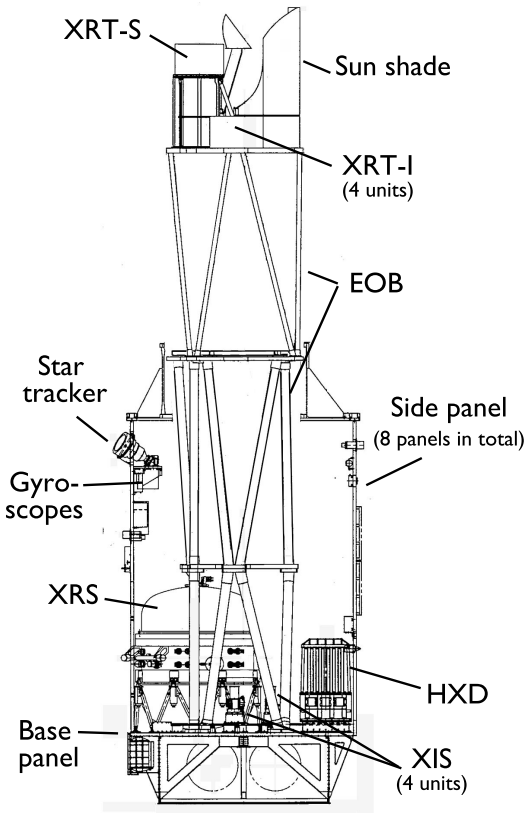

Figure 3.1: Internal structures view of *Suzaku* (Mitsuda et al. 2007).

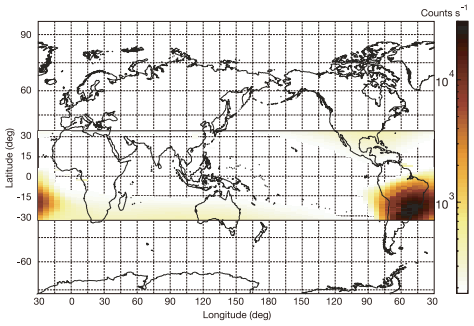

Figure 3.2: Particle counts measured with the HXD in the *Suzaku* orbit (Kokubun et al. 2007).

3.2 X-ray Telescope (XRT)

The XRT is a Wolter-I type telescope and is mounted on top of the *Suzaku* optical bench. As shown in Figure 3.3, five telescopes are mounted and 4 of them are paired with the four XIS cameras. The focal length of the mirror is 4.75 m. In total 1400 sheets of a reflector made of thin aluminum foil, coated with thin gold layer are used in the XRT. To avoid multiple reflection of photons from out of line of site, pre-collimators are mounted on the telescope. In Table 3.1, the specifications of the XRT are listed up.

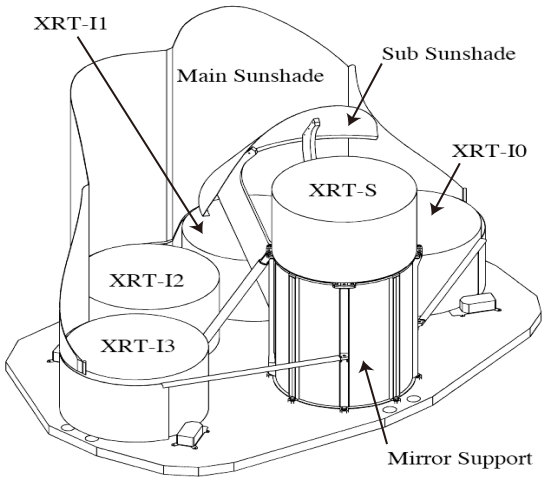

Figure 3.3: A schematic view of the XRT on *Suzaku*. (Serlemitsos et al. 2007)

Table 3.1: Specifications of XRTs taken from Serlemitsos et al. (2007)

Geometric area (cm^2)	873
Weight (kg)	19.3
Field of view (1 keV/7 keV)	$20'/14'$
Effective area (1.5 keV/7.0 keV)	450/250 cm^2
Spatial resolution (HPD)	$2'.0$

In Figure 3.4, the effective area of the XRT is shown. Around 2.0 keV, decrease of the area appear because of K-edge of Al (1.56 keV) and M-edge of Au (2.3 keV). When we analyze bright sources, those structure generate uncertainty. Above ~10 keV, the mirror cannot reflect X-ray photons and their effective area decrease drastically. As another important property, we show Point Spread Functions (PSFs) of the XRT. All of the XRT have very similar PSF and their spacial resolutions are evaluated as $2'.0$ with half of power diameter.

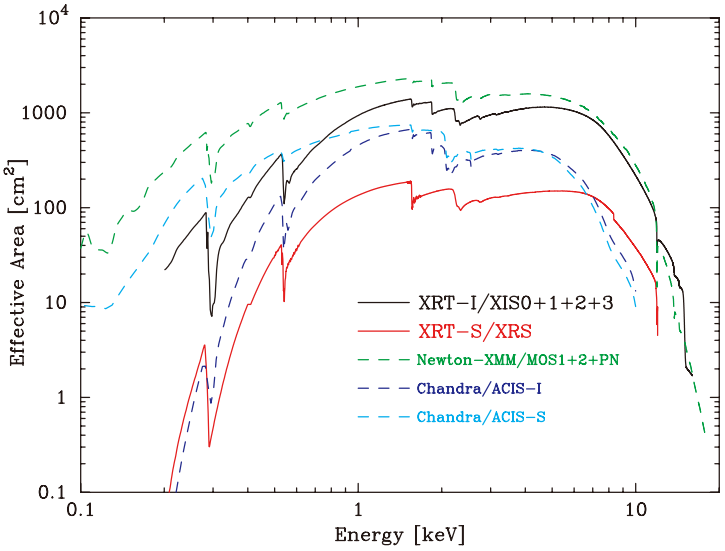

Figure 3.4: Effective areas of the XRT. The dashed lines are those of the other satellites. (Serlemitsos et al. 2007)

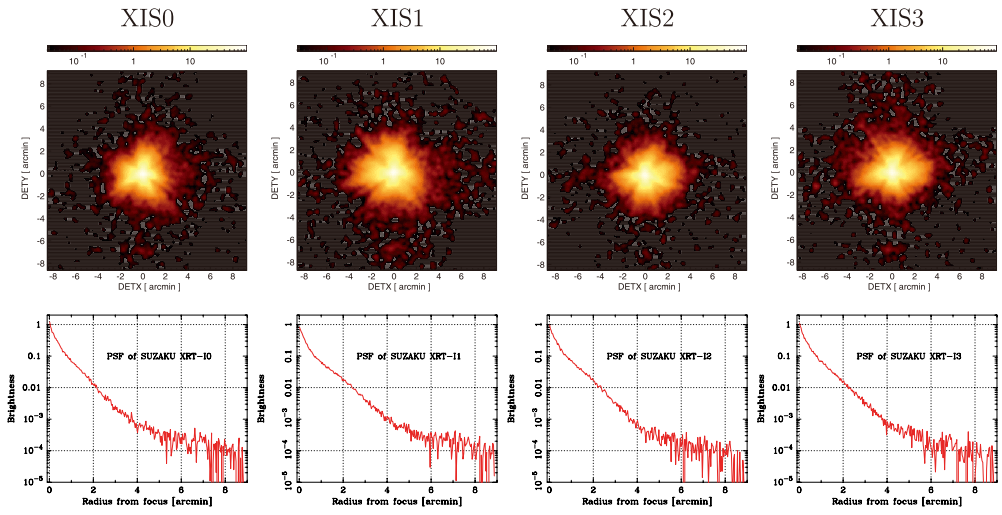

Figure 3.5: XIS images (top) and PSF (bottom) of four piesces (Serlemitsos et al. 2007)

3.3 X-ray Imaging Spectrometer (XIS)

To cover soft X-ray band, four X-ray CCD cameras, XIS0, XIS1, XIS2, and XIS3, are mounted. Among them, XIS1 are back illumination type, while the other three are front illumination type. The cameras are cooled by thermal electric cooler and kept at ~50°C to achieve low noise and good energy resolution. In this analysis, we utilize only front illuminated cameras because background level of XIS1 is higher than those of the other camera. In Figure 3.7, we show raw image of XIS0 and the source (blue) and background (green), 2' circle or box, region .

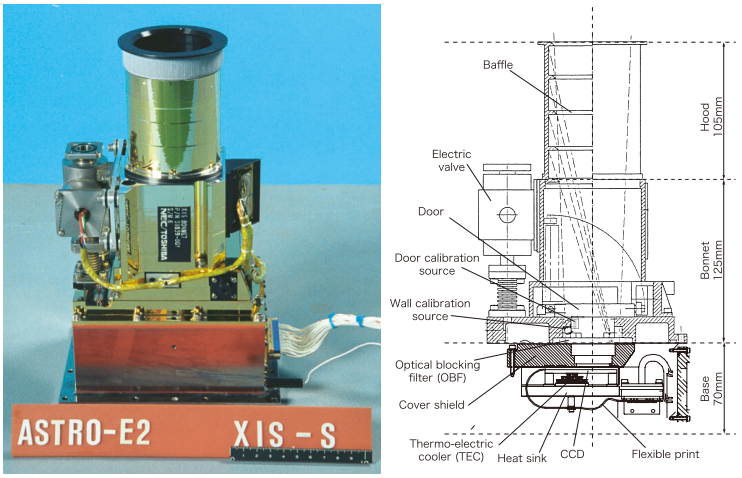

Figure 3.6: (a) A picture of XIS sensor part. (b) XIS cross section. Koyama et al. (2007)

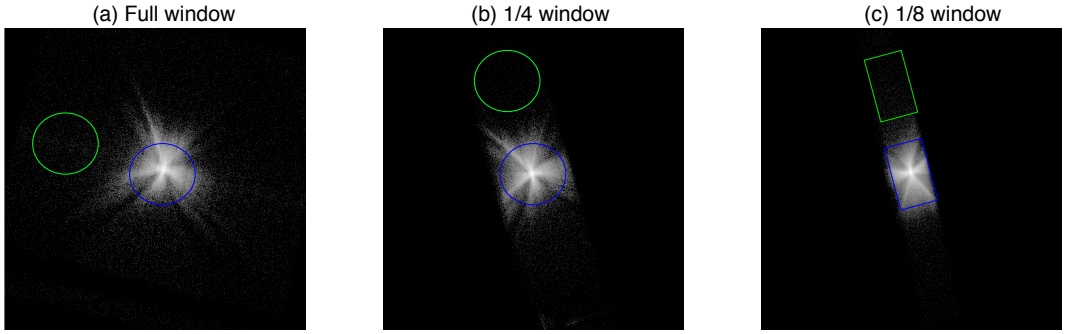

Figure 3.7: (a) An image obtained with the full window mode. (b) The 1/4 window mode. (c) The 1/8 window mode.

The XIS have some operation mode, full window, 1/4, and 1/8 modes, to accept efficiently observe many types of X-ray sources. In Figure 3.7, we show three images, which are obtained with full, 1/4, and 1/8 window mode respectively. Although the detection regions decrease in the 1/4 and 1/8 window mode, time resolution become 4 and 8 times higher, respectively. The window modes are suitable for BXP observations because they typically have 10-100 s pulse periods (§2.3.3) and are bright sources. In the case of the full window mode, the time resolution is 8 sec. When we use the 1/4 or 1/8 window modes, time resolution become 2 and 1 sec, respectively and are fast enough to detect typical BXP pulses. As another merit, pile-up

effects are decreased by the window mode because the data taking life time becomes 1/4 or 1/8 of normal mode. In some observations of BXPs, the source fluxes become very high and make pile up even with the special window mode. In such cases, the XIS are often operated with burst clock options. When we use the option, the data taking life time becomes shorter than those of the window modes and reduce pile up effects by discarding the photons observed in the remaining exposure.

Some of BXPs have short pulse periods so that a high time resolution is needed to detect the pulsation. To detect such a fast variability, the timing mode (P-sum mode) is prepared. With the P-sum mode, signals from whole 1024 channel of one side is added, making the readout time $\sim$ 1000 times faster. As the cost, we cannot obtain two dimentional image but only one dimentional positional information. The energy resolution also significantly degrades. In that case, readout time becomes much shorter as 7.8 ms and the time resolution is fast enough to detect pulsations of the BXPs. In Figure 3.8(a), we show image obtained with the P-sum mode. In this plot, the horizontal distribution is the 1D positional information, while the vertical distribution is the timing information. The projection results are shown in Figure 3.8(b) and have some spiky structures by thermal noises so that those structure lanes are excluded in our analysis.

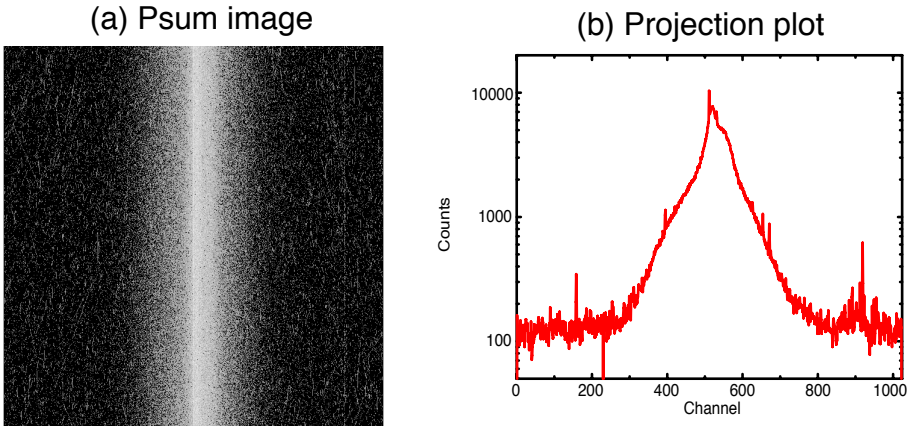

Figure 3.8: (a) The image of the P-sum mode, which is extended to vertical axis. (b) The vertical projection of Figure 3.8(a).

3.4 Hard X-ray Detector (HXD)

The Hard X-ray Detector covers very wide energy band from 10 to 600 keV by combining with the semiconductor, Si-PIN diode (PIN) and the inorganic scintillator, Gd_2SiO_5 (GSO). To reduce the background level, they are putted on the bottom of wells made of the inorganic scintillator, $Bi_4Ge_3O_{12}$ (BGO) glued to a Photo-Multiplier Tube (PMT). This main units are called "Well units", as shown in Figure 3.9. In the each BGO Well unit, 4 PINs and GSO scintillators are stored and GSO are glued with BGO scintillator. The BGO well is utilized for an active shield to reduce background events including photons from out of the field of view. As shown in Figure 3.11(a), the BGO wells are packed by white reflector, Gore-Tex, to keep good light outputs from the scintillator. Totally, the HXD is made of 16 BGO Well units, namely 64 PIN and GSO. As shown in Figure 3.10(b), effective areas summed up 64 PIN diodes are ∼150 cm^2 at 20 keV, and those of the GSO in 100 keV is ∼ 250 cm^2. The 16 Well units are surrounded by "Anti unit", which is composed by only BGO. The Anti units are adopted for only reduction of the background. By the well-shaped active deep shield and combining multiple unit to not only ti increase the are but also to use one-another as an additional deep active shield, the HXD has proven to have the lowest background especially in the PIN band compared to any other existing hard X-ray instruments as shown in Figure 3.10(a).

In the Well units, the fine collimators, which are made of 50μm thick phosphor brozen and meshed 8×8 square channel with a length of 320 mm in 3.2 mm pitch, define a FOV 34'×34' in full-width at half maximum square (FWHM). The fine collimator is valid below 100 keV while it can not stop photons above 100 keV because phosphor brozen have less cross-section at high energy. Above 100 keV, the maximum FOV is defined by the size of the BGO Well-unit as 4°.5×4°.5. After launch, one of the tow heat pipes have a trouble and it do not work well. From this reason, the HXD is operated at ∼ −15−−12°C, which is higher that the original plan (∼-20°C), in the orbit. Operating with ∼-12°C, thermal noise excesses signal too much in lower energy (<15 keV) and make difficult to utilize PIN data below 15 keV. As shown in Fiugre 3.2, the HXD has large count rates of high energy particles in the SAA. To avoid PMTs damaged in SAA, high voltage supplies to PMTs are stopped in the period.

To detect 10-70 keV photons effectively, the PIN diodes are much thicker (∼2 mm) than general PIN photo diodes. The HXD-PIN needs to be applied very high voltage (∼500 V) to be fully depleted while typical PIN diodes are applied only a few ten volts. Their size is 21.5×21.5 mm^2, which is smaller than that of HXD-GSO (Figure 3.11) to be fitted within the bottom of the fine collimator. Their energy resolution is (∼4 keV). Bothe the GSO and PIN signals shares the same trigger system and the event has a time resolution of μs (Takahashi et al. 2007).

The signals from the GSO scintillators are read out by the PMT glued to the Well unit BGO so that GSO and BGO signals are mixed out from the PMT. To divide the signals, they are filtered with pulse shape discrimination (PSD). HXD-GSO have faster decay time than BGO

and the different decay time make the difference between pulse height of two shapers, fast (∼150 ns shaping time) and slow (∼1 μs). In Figure 3.12, we show a 2 dimensional plot of the fast and slow shaper pulse heights. There are two branches caused by the GSO and BGO signals, and those signals are clearly divided. The GSO scintillators emit a certain amount of high energy particles and photons by themselves because it is exposed to heavy cosmic ray particles and activated, and background level becomes gradually high after launch. When the satellite passes through the SAA, the HXD-GSO shows large background level (Fukazawa et al. 2009). Non X-ray backgrounds of HXD-GSO are also provided by *Suzaku*-HXD team and estimated including the radioactivation (Fukazawa et al. 2009).

Non X-ray background is caused by activations, neutron reactions and a small leakage of the Cosmic X-ray background and earth albedo gamma-rays. Since the orbital environment in view of Cosmic ray changes with the geo-magnetic cut off rigidity as well as the SAA, the non X-ray background it self is time variable. The HXD-team provides the background model based on the real data obtained within the earth occultation, sorted with a few major orbital parameters. The background thus estimated is distributed via the web-site in ISAS/JAXA to the whole globe (Fukazawa et al. 2009).

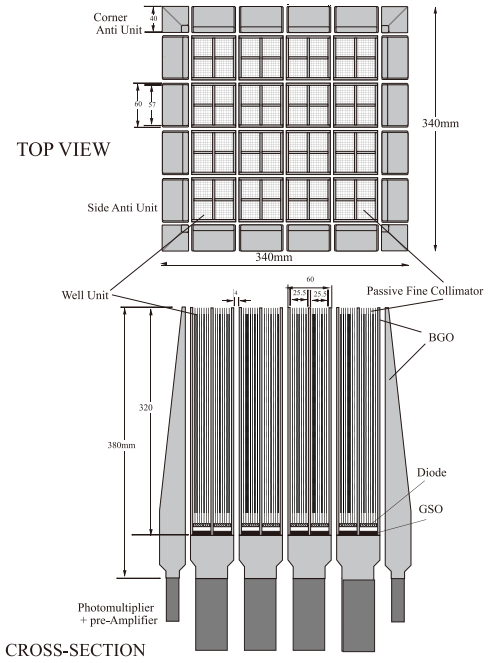

Figure 3.9: A schematic view of the HXD (Takahashi et al. 2007)

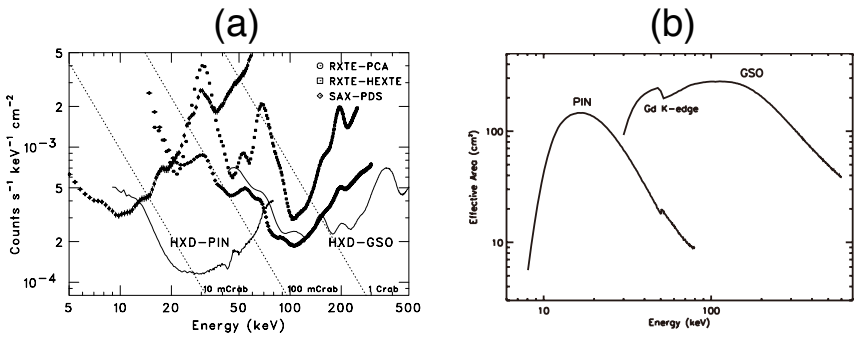

Figure 3.10: (a) The sensitivity of the HXD, Kokubun et al. 2007. (b) Effective areas of HXD-PIN and GSO. (Takahashi et al. 2007)

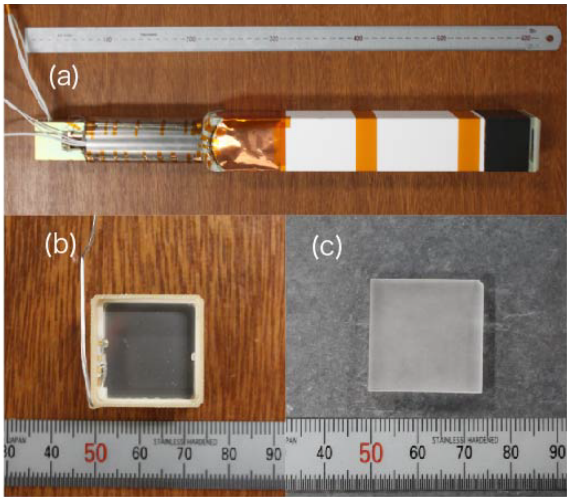

Figure 3.11: (a) A flight spare Well unit of the HXD. (b) A PIN detector. (c) A GSO scintillator for the HXD.

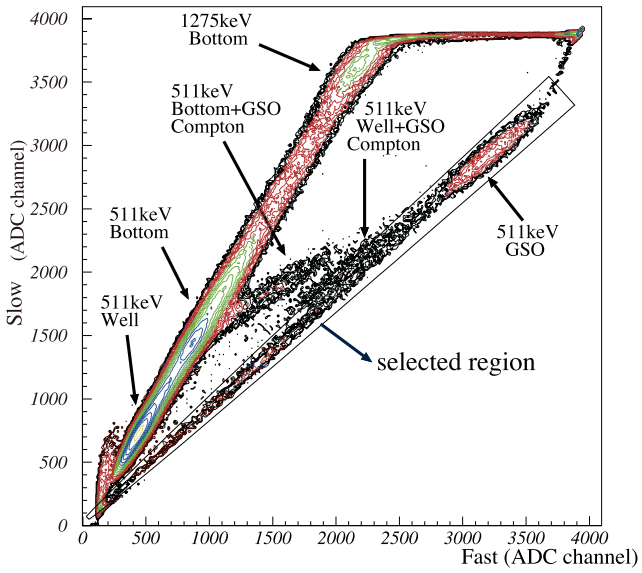

Figure 3.12: The plot between pulse height of fast shaper and that of slow shaper.

Chapter 4

OBSERVATION

As of 2014 December, more than 30 BXPs have been observed with *Suzaku*, more than 60 times in total, and the acquired data are mostly available in archive. The present thesis utilizes these available data sets 42 in number after excluding those which are too short (< 10 ks), and in which the target source was too faint (< 0.5 count s^{-1} with each XIS). Each observation lasted typically for ∼1 to ∼2 days, depending on the objective. However, the orbit of *Suzaku* is almost circular with an altitude is of ∼ 550 km. Therefore, the sight of *Suzaku* is interrupted by the earth, typically for ∼30% of each orbit (∼30 min; so called earth occultation). In addition, data acquisition must be stopped when the satellite pass through SAA (§3.4). Thus, the net exposures become ∼50% of the gross exposures, and the data suffer periodic gaps. Below, we described how those data sets have been acquired. Since the observation strategy differs among Be pulsars (§2.1.4), OB pulsars (§2.1.4) and others (§2.1.3), these 3 classes are described separately.

4.1 Be Pulsars

4.1.1 Observations in X-ray outbursts

As described in §2.1.4, Be pulsars (binaries with Be-type primaries and strongly magnetized NSs) show X-ray outbursts which are synchronized with $P_{\rm orb}$, and remain in quiescence when the NSs are away from their periastron phases. So far 7 BXPs have been observed with *Suzaku* on 13 occations in total, of which 5 were Target of Opportunity (ToO) observations to catch the top of an X-ray outburst. Most of these ToO observations were triggered based on alerts from the operating X-ray all sky monitors, *MAXI*, *RXTE*, and *Swift*. In Figure 4.1, we show long term light curves of these Be binaries obtained by *MAXI* and *Swift*, together with the dates of *Suzaku* observations. Table 4.1 summarizes the information of these observations of Be pulsars.

As shown in Table 4.1 and Figure 4.1, nine observations of six objects, A 0535+26, 1A 1118−61, GX 304−1, GRO J1008−57, EXO 2030+375, and KS 1947+300, have been conducted in X-ray outbursts. Three (GX 304−1, EXO 2030+375, and GRO J1008−57) of the six objects were observed twice in outbursts. In all of those observations, the XIS employed the one-fourth window mode, to avoid pile up effects and to realize a better time resolution (2 sec), which are both needed for pulsating bright sources like Be pulsars in outbursts. An XIS0 (1-10 keV) light curve of a typical Be binary is shown in Figure 4.2, in which the average count rate was $\sim$ 180 count s^{-1}. Including this case, eleven observations utilized the XIS burst mode (§3.3) with various snap times (Table 4.1), to further reduce pile ups under high count rates.

Count rates varied rapidly in observations as shown in Figure 4.2, because of the X-ray pulsations. Including in this particular case, Be pulsars thus exhibit relatively constant pulse amplitudes, in contrast to OB binaries (§4.2). The Be pulsars in our sample have pulse periods of P_s=10-400 s, so that the time resolutions of the XIS (2.0 s) and HXD (67 μs) are both high enough to resolve the pulses. For the timing and spectral analysis, we adopt 2.0 arcmin circle on each XIS image as a source and a background region, except in some bright source for which we need to exclude the center of the source image to discard those photons which can be affected by the CCD pile up.

As already reported by previous works using the same *Suzaku* data, spectra of these objects were obtained by the XIS and HXD-PIN with good statisticcs. In addition, they were mostly bright enough to detect with HXD-GSO and allow a construction of wide-band spectra (1-100 keV). With the spectra obtained by the HXD, some previously known CRSFs were confirmed, and new CRSFs have been discovered from 1A 1118−61, GX 304−1, and GRO J1008−57 at $\sim$ 50 keV and 70 keV, respectively (Suchy et al. 2011, Yamamoto et al. 2011, Yamamoto et al. 2014).

Table 4.1: Suzaku observation lists of Be binaries

Object	ObsID	Start Date	Exposure	Nominal	ObsMode	Reference
1A 1118−61	403049010	2009-01-15 12:20:47	24.66/46.81	HXD	1.0 s-burst,1/4-win	a
	403050010	2009-01-28 05:37:35	21.95/30.78	HXD	1.0 s-burst,1/4-win	a
A 0535+26	100021010	2005-09-14 13:40:04	21.76/21.01	—	normal,1/4-win	b,c
	404054010	2009-08-24 23:06:11	25.75/41.88	HXD	1.0 s-burst,1/4-win	d
	404055010	2010-04-06 12:03:28	3.18/34.39	HXD	0.1 s-burst,1/4-win	—
EXO 2030+375	402068010	2007-05-14 20:37:12	28.6/53.4	HXD	1.0 s-burst,1/4-win	e
	407089010	2012-05-23 20:12:35	77.95/72.4	XIS	normal,1/4-win	—
GRO J1008−57	902003010	2007-11-30 11:32:46	23.71/42.1	XIS	1.0 s-burst,1/4-win	f
	907006010	2012-11-20 14:44:31	9.06/52.87	XIS	0.3 s-burst,1/4-win	g
GX 304−1	406060010	2012-01-31 10:29:20	16.69/58.72	XIS	0.5 s-burst,1/4-win	—
	905002010	2010-08-13 16:18:49	5.13/12.87	HXD	0.5 s-burst,1/4-win	h
KS 1947+300	908001010	2013-10-22 05:12:52	29.0/29.46	XIS	0.14 s-burst,1/4-win	—
XTE J1946+274	405041010	2010-10-11 21:48:30	50.73/45.65	HXD	normal,1/4-win	i

(a) Suchy et al. (2011), (b) Terada et al. (2006), (c) Naik et al. (2008), (d) Yamada et al. (2011), (e) Naik et al. (2013), (f) Naik et al. (2013), (g) Yamamoto et al. (2014), (h) Yamamoto et al. (2011), (i) Maitra & Paul (2013a)

4.1.2 Low luminosity observations

To study dependence of timing and spectral properties on the luminosity, three Be pulsars were observed also in quiescence, namely, in orbital phases far away from the periastron, or when the overall activity was rather low. These are A 0535+26, 1A 1118−61, and X 0331+53. As shown in Figure 4.1, the first two sources were detected in quiescence (in addition to the outburst observations), when they were two orders of magnitude fainter than in outbursts. Although X 0331+53 was observed in a minor outburst and was detected with the XIS, it was too faint to detect with HXD-PIN. Therefore, this data set is excluded from the present study.

Among these quiescence observations of Be binaries, particularly noteworthy ones in that of A 0535+26, conducted in 2005 September just 2 months after the *Suzaku* launch. In spite of the source faintness (only ∼50 mCrab), the signals were detected, not only with the XIs and HXD-PIN, but also with HXD-GSO up to ∼100 keV. As quoted in Figure 4.4, the HXD data allowed a clear detection of the CRSF (§2.3.2) at ∼45 keV, which had been suggested by Kendziorra et al. (1994) with relatively low significance. This result demonstrated the power of the HXD, and was published in Terada et al. (2006) as one of the very first *Suzaku* papers. As described in §4.2 of Kokubun et al. (2007), the CRSF of A 0535+26 also contributed to the energy cross calibration between HXD-PIN and HXD-GSO.

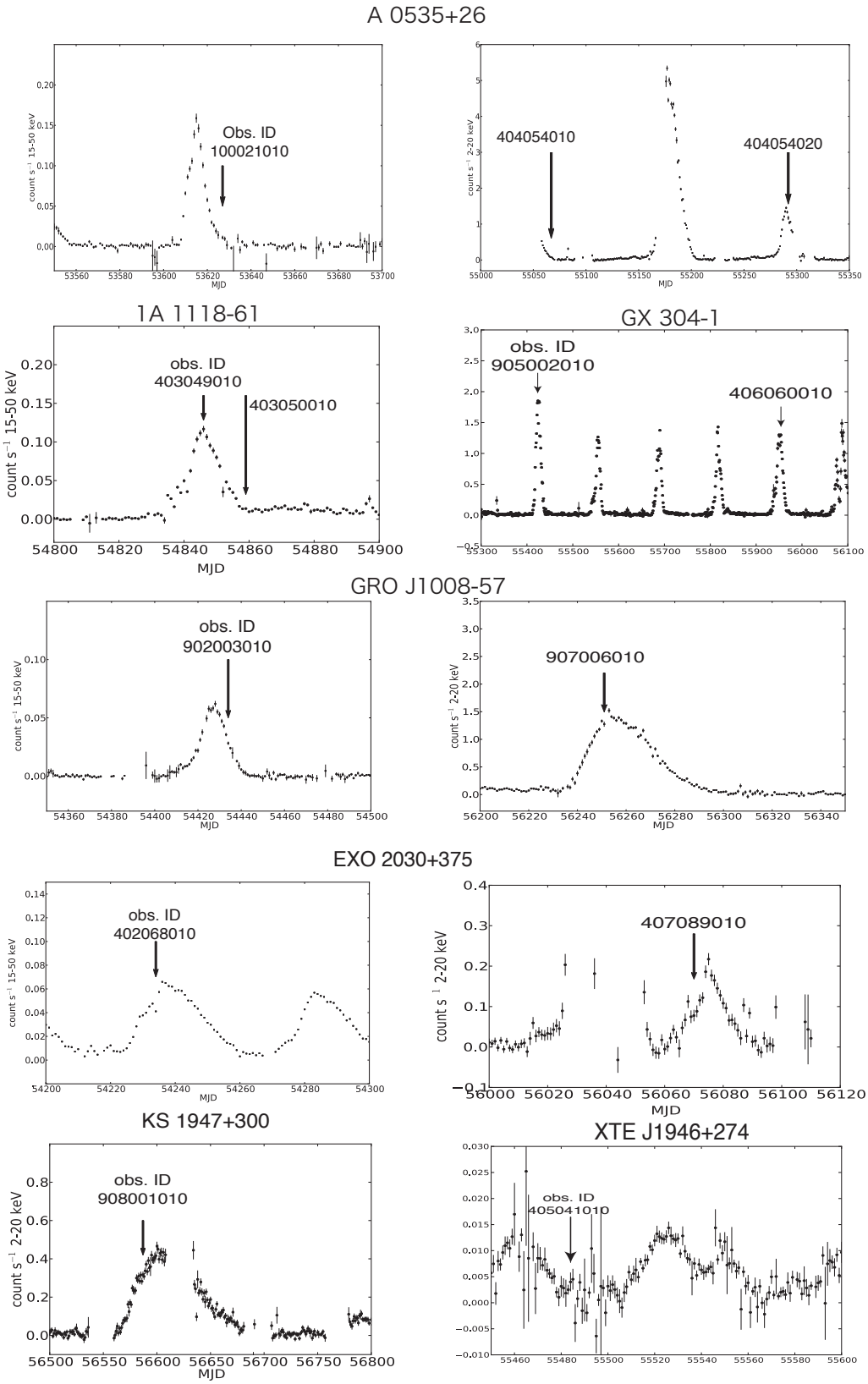

Figure 4.1: Long term light curves of the Be pulsars analyzed in the present thesis, obtained by *MAXI*-GSC (2-20 keV) and *Swift*-BAT (15-50 keV). The arrows indicate the dates of *Suzaku* observations.

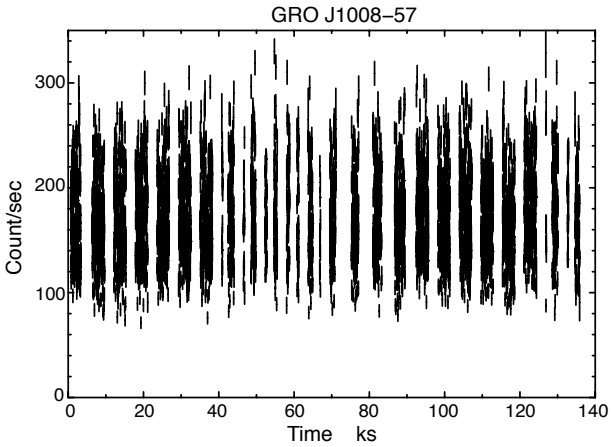

Figure 4.2: A 1-10 keV light curve of the Be pulsars, GRO J1008−57, obtained by the *Suzaku* XIS0. The data are binned into 16 seconds.

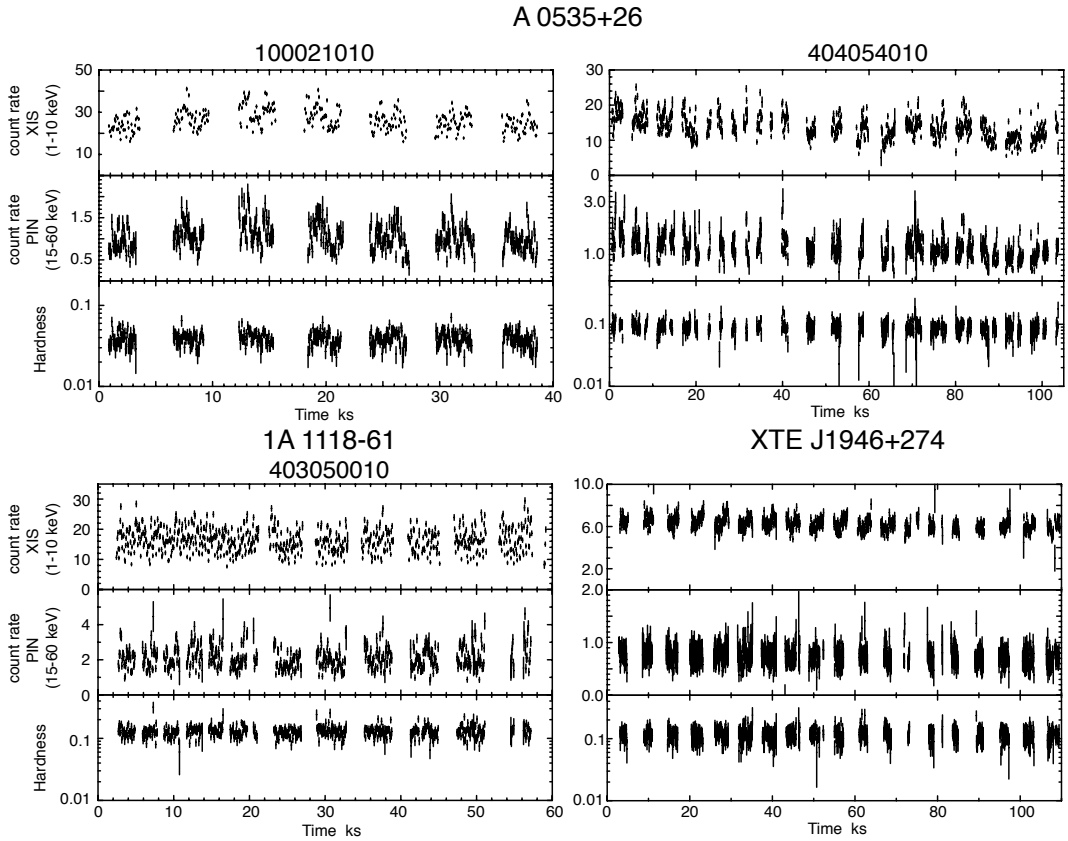

Figure 4.3: Backgournd-subtracted light curves of three Be pulsars in quiescence: A 0535+26 (top), 1A 1118−61 (bottom left), and XTE J1946+274 (bottom right). In each data set top shows the XIS (1-10 keV) data, middle is the HXD-PIN (15-60 keV) data, and bottom is hardness ratio between them.

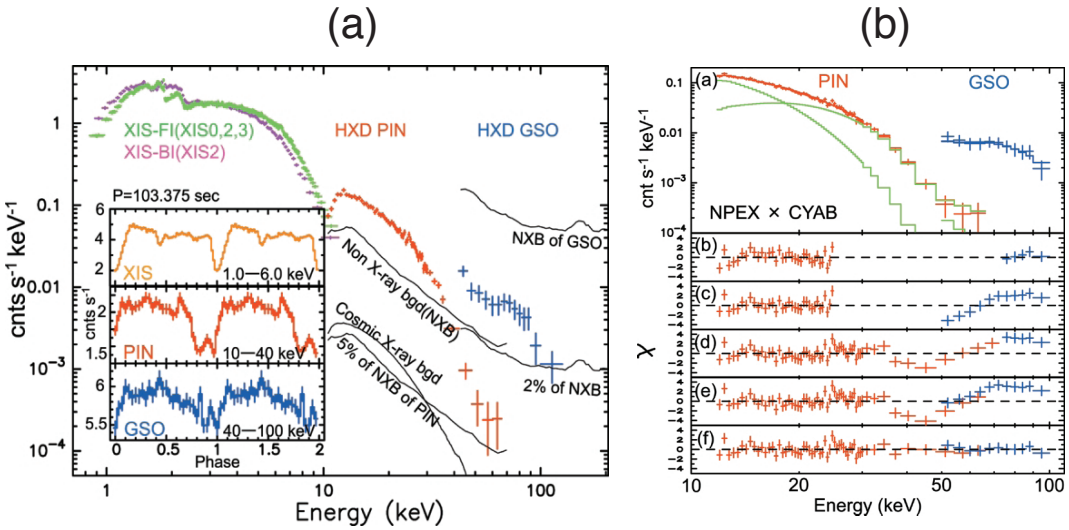

Figure 4.4: (a) Raw X-ray spectra of A 0535+26, obtained with *Suzaku* in a low luminosity state (Terada et al. 2006). (b) Fitting of the HXD data with different spectral models. The bottom 5 panels show how the fit residuals diminish as the model is improved, finally including the CRSF factor at 45 keV (also Terada et al. 2006)

4.2 BXPs with OB Type Supergiant Primaries

Another major subclass of BXPs is those with OB type supergiant primaries, to be called "OB pulsars". These objects show rapid flares randomly, while Be pulsars produce periodic outbursts as described in §2.1.4 and §4.1. Twelve OB pulsars have been observed by *Suzaku*, as summarized in Table4.2. Eight of the 12 sources were extensively studied by other satellites, so that they are classified as classical objects in this study. The remaining four OB pulsars, 4U 0352+30 (X-per), 4U 0114+65, 4U 2206+54, and 4U 1909+07 have longer pulse period than the other 8 objects, and remain much less understood, even though they have been catalogued from the 1970's as their names suggest. Therefore, we categorized them as a separate class, long period pulsars (LPPs; details in §4.2.2).

Table 4.2: Same as Table 4.1 but for O,B binaries.

Object	ObsID	Start Date	Exposure	Nominal	ObsMode	Reference
4U 1907+09	401057010	2006-05-02 06:11:34	58.44/37.94	XIS	normal,1/4-win	a
	402067010	2007-04-19 10:03:36	80.63/72.98	HXD	normal,Full-win	a
4U 1538−52	407068010	2012-08-10 00:04:29	45.96/38.99	XIS	normal,1/4-win	b
Vela X-1	403045010	2008-06-17 04:45:17	104.72/95.79	XIS	normal,1/4-win	c,d
GX 301−2	403044010	2008-08-25 13:15:17	11.43/10.56	HXD	normal,1/4-win	e
	403044020	2009-01-05 10:33:04	61.81/54.69	HXD	normal,1/4-win	e
Cen X-3	403046010	2008-12-08 06:55:36	48.45/79.32	HXD	1.0 s-burst,1/4-win	f
OAO1657−415	406011010	2011-09-26 09:34:20	84.73/74.24	XIS	normal,1/4-win	—
LMC X-4	702036020	2008-04-05 13:15:26	25.34/24.02	XIS	normal,1/8-win	g
	702037010	2008-02-11 00:42:25	23.39/20.04	XIS	normal,1/8-win	g
	702038010	2008-01-15 08:39:26	21.67/22.88	XIS	normal,1/8-win	g
SMC X-1	706030010	2011-04-07 20:45:08	18.47/15.47	XIS	normal,1/4-win,P-sum	—
	706030020	2011-04-18 06:08:54	17.28/16.98	XIS	normal,1/4-win,P-sum	—
	706030030	2011-04-22 15:34:39	15.65/21.26	XIS	normal,Full-win,P-sum	—
	706030040	2011-05-10 00:28:25	17.92/16.81	XIS	normal,Full-win,P-sum	—
	706030050	2011-05-25 02:02:40	17.85/16.27	XIS	normal,1/4-win,P-sum	—
	706030070	2011-09-21 04:07:49	18.28/16.62	XIS	normal,1/4-win,P-sum	—
	706030080	2011-11-10 01:50:36	19.89/19.25	XIS	normal,1/4-win,P-sum	—
	706030090	2011-12-12 21:33:51	17.41/18.41	XIS	normal,Full-win,P-sum	—
	706030100	2012-03-19 06:14:12	18.63/20.29	XIS	normal,Full-win,P-sum	—
4U 0352+30†	407088010	2012-08-27 08:38:37	153.49/140.6	XIS	normal,1/4-win	—
4U 0114+65†	406017010	2011-07-21 10:20:15	106.55/88.22	XIS	normal,1/4-win	—
4U 2206+54†	402069010	2007-05-16 03:53:25	103.86/99.66	HXD	normal,1/4-win	h
4U 1909+07†	405073010	2010-11-02 16:53:27	29.3/21.3	XIS	normal,1/4-win	—

(a) Rivers et al. (2010), (b) Hemphill et al. (2014), (c) Doroshenko et al. (2011), (d) Maitra & Paul (2013b), (e) Suchy et al. (2012), (f) Naik et al. (2011a), (g) Hung et al. (2010), (h) Finger et al. (2010), (i) Fürst et al. (2012)
† Long period pulsars.

4.2.1 Classical objects

Objects in this class have been discovered basically by the oldest satellite *Uhuru*. Most of them are located in our galaxy (<8 kpc), while LMC X-4 and SMC X-1 are in the Large Magellanic Cloud (∼60 kpc) and, the Small Magellanic Cloud (∼55 kpc), respectively. As described in §2.1.4, their orbital periods are typically 10 d, shorter than those of Be pulsars (a few weeks to

months). The NSs are close to the primary stars and they are usually luminous, because they persistently capture stellar winds from the companion stars. Thus, their observations do not need to be triggered by other all sky monitors, and hence their observation have never been conducted as a ToO.

In these observations of OB pulsars, the XIS was mostly operated in the one-fourth window mode for the same reason for the Be pulsars. The pulse periods of the objects are typically $\sim$ 100 s, which are long enough to detect with the 1/4-window mode. In addition to the longer $P_{\rm s}$, the sources are lower luminous than Be pulsars in outbursts, so that the 1/4-window mode is sufficient to prevent pile ups. In the LMC X-4 observations, the one-eighth window mode was adopted because $P_{\rm s}$ is short. In the case of SMC X-1, $P_{\rm s}$ is too short ($\sim$0.7 s) for usual XIS window mode, so that XIS3 was operated in the P-sum mode (§3.3).

In Figure 4.5 and 4.6, we show background subtracted light curves of several OB pulsars, obtained by the XIS (1-10 keV) and HXD-PIN (15-60 keV). Individual pulses are visible in some sources (e.g., 4U 0114+65 and 4U 2206+54) with long pulse periods As described in §2.1.4, these sources exhibit rapid and violent variability. The XIS intensity of Vela X-1, OAO 1657−415, and Cen X-3 varied by 1-2 order of magnitudes, while those of LMC X-4 and SMC X-1 were almost constant. The light curves of OAO 1657−415 and Cen X-3 exhibit eclipses. The hardness of some sources also changed by a factor 5 - 10, implying significant spectral changes.

Most of these classical objects show CRSFs in their spectra. The spectra of Vela X-1 exhibit a weak fundamental structure at $\sim$25 keV, and a strong 2nd harmonic at 50 keV (Doroshenko et al. 2011). Cyclotron absorptions of Cen X-3, 4U 1538−52, 4U 1907+09, and GX 301−2 were detected at 30 keV, 20 keV, 18 keV, and 37 keV, respectively (Naik et al. 2011a, Hemphill et al. 2014, Rivers et al. 2010, and Suchy et al. 2012). The other sources in our sample (e.g., OAO 1657-415, LMC X-4, SMC X-1) do not show clear cyclotron structures, and hence their magnetic field strengths remain unknown.

As described in §2.1.4, OB pulsars show strong photoelectric absorption and Fe fluorescence line in their spectra. Especially, These features have been studied for many decades (Inoue 1985, Makishima et al. 1986). From *Tenma* observations, it have been cleared that equivalent widths, EWs, of Fe line are proportional to the column density when the absorption is strong (Inoue 1985), while it becomes nearly constant in low-absorption conditions. In the very luminous source, Cen X-3, not only a neutral Fe line but also ionized lines have been detected (§2.3.1).

4.2.2 Long period pulsars (LPPs)

Among about 20 OB pulsars that lack the reported CRSFs, some have very long P_s, exceeding ~1000 s. These are the LPPs (Long Period Pulsars) which we introduced in the beginning of the present section. In the present thesis, we more specifically define LPPs as BXPs which have Ps > 600 seconds and no CRSF detection from past observations, regardless of their companion type. According to this definition, four OB pulsars, 4U 0352+30, 4U 0114+65, 4U 2206+54, and 4U 1909+07, can be classified as LPPs. They are all persistent sources, and have been observed with Suzaku. Although 4U 1954+319 is a binary with a low-mass companion (i.e., an LM-BXPs), it also has an extremely long P_s (~ 20000 s), and no CRSF has ever been detection (§4.3.3). Therefore, it is included as the LPP class. These 5 sources, namely the four OB pulsars and one LM-BXPs, form a nearly complete sample of this class, although a few are missing.

In the observations, the XIS was operated with 1/4-window mode. Excluding the observation of 4U 1909+07, the net exposures were long (> 100 ks). As shown in Figure 4.6, the light curves of 4U 0114+65 and 4U 2206 show clear X-ray pulsations, for 14 cycles and ~ 26 cycles, respectively. In addition to the pulsation, the four objects show time variability like OB binaries, and pulse-by-pulse amplitude variations. Although some LPPs have been studied over relatively wide energy ranges (e.g., Di Salvo et al. 1998 and Doroshenko et al. 2012), their spectra are not yet described in a uniform manner, because of considerable differences from those of typical BXPs. No CRSF has been detected convincingly from any LPP.

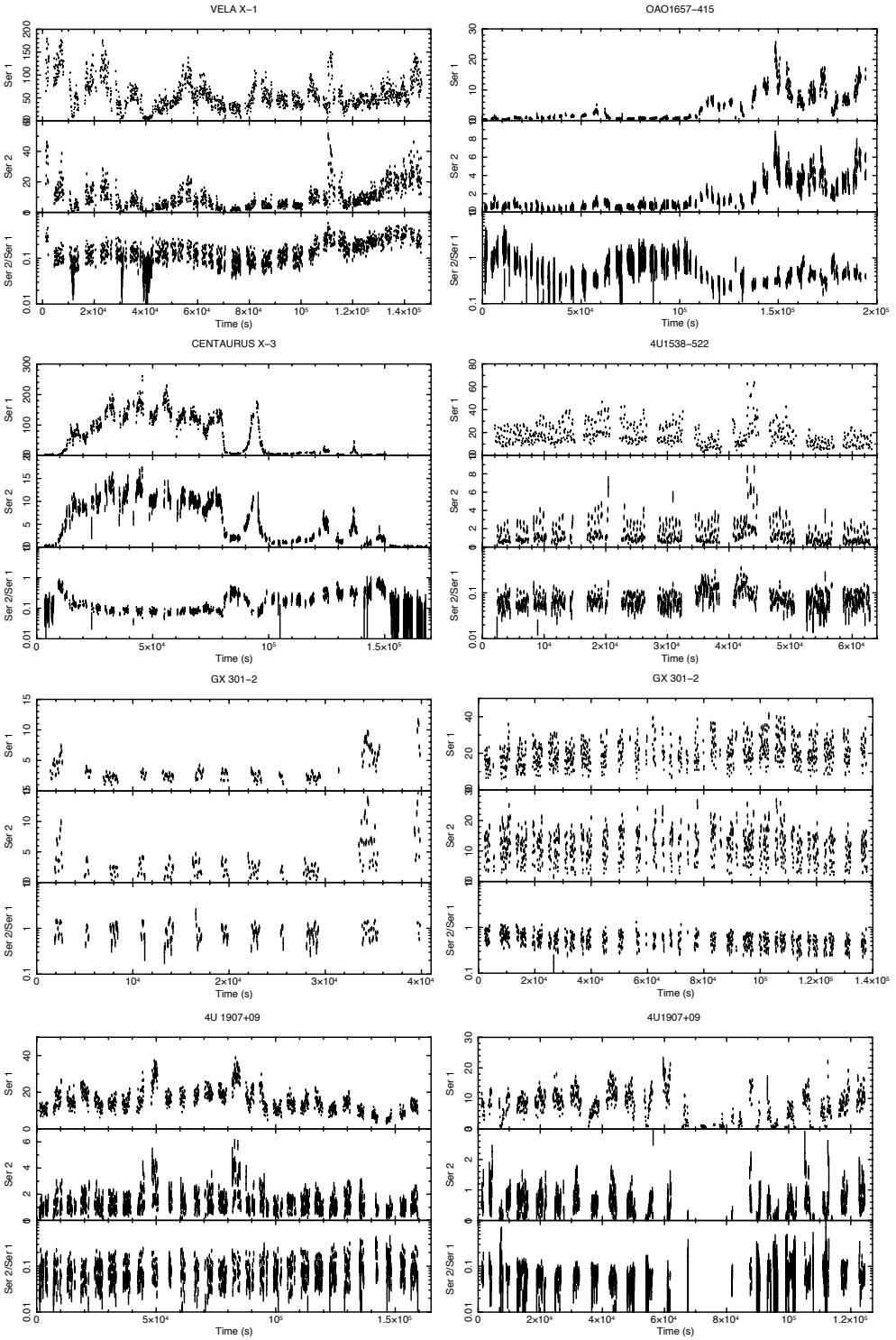

Figure 4.5: Light curves of OB pulsars.

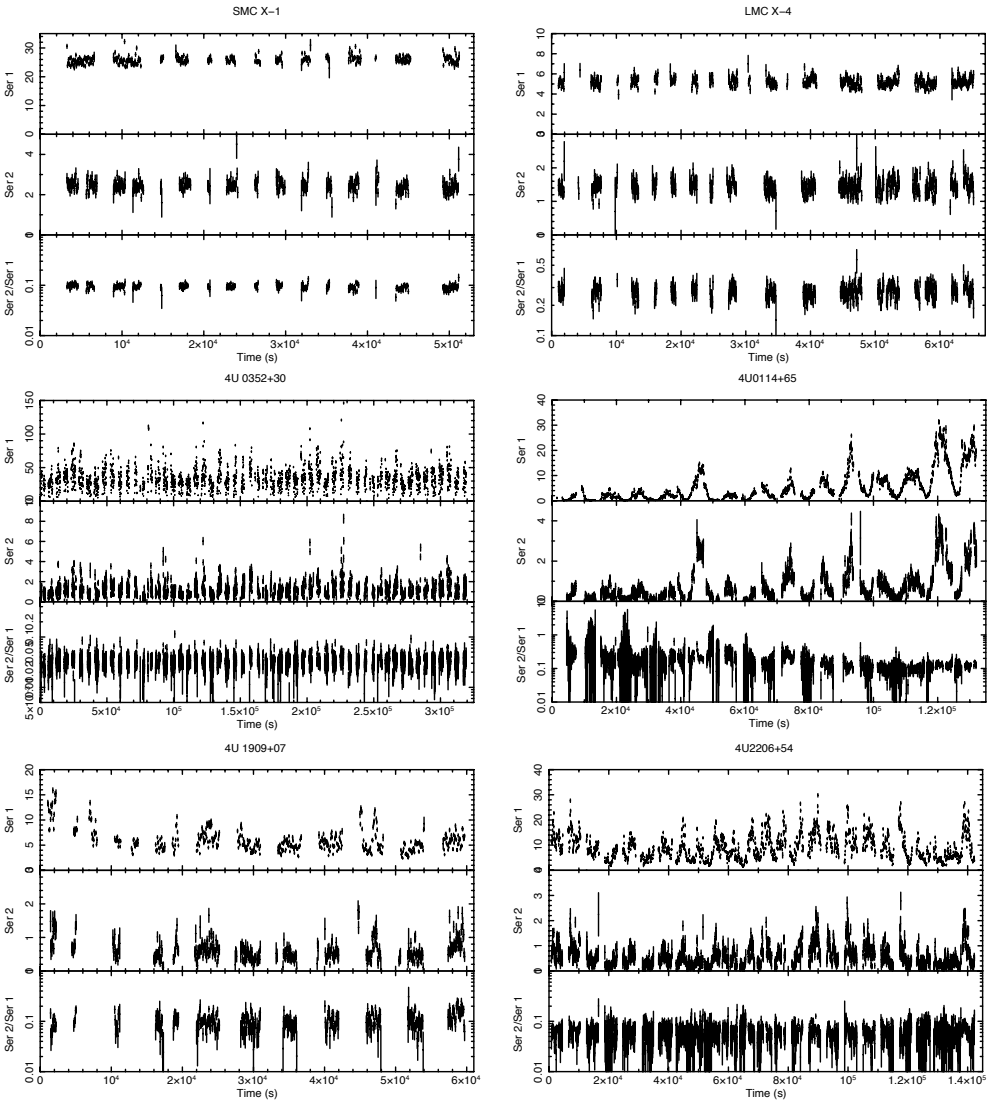

Figure 4.6: Same as Figure 4.5 but for the other 6 OB pulsars including LPPs.

4.3 X-ray Pulsars with Low-mass Stars

X-ray pulsations are seldom detected from LMXBs (§2.1.3), and if any,we found at very short period ($P_{\rm s} \simeq$ a few msec to a few tens msec). Only 6 exceptional LMXBs have $P_{\rm s}$ >0.1 s. The six objects, all included in our sample, are Her X-1, 4U 1626−67, 4U 1822−37, GRO J1744−28, GX 1+4, and 4U 1954+319. The three of the six, Her X-1, 4U 1626−67, and 4U 1822−37 are persistent sources while GRO J1744−28 is a transient. Companions of GX 1+4 and 4U 1954+319 are M-type giant stars, and the binaries are called, symbiotic X-ray binaries (SyXBs). We collectively call these objects BXPs with low-mass companions, or LM-BXPs

4.3.1 Persistent LM-BXPs

Since these three objects possess short $P_{\rm s}$, their observations require relatively high time resolution. Therefore, the XIS was operated in high-time-resolution modes in some of these observation (Table4.3). The three persistent sources are considered to have accretion disks like typical LMXBs (§2.1.3). As shown in Figure 4.7(a), Her X-1 shows long time variability with the ∼35 d period, which is usually ascribed to disk precession. Actually, as shown in Figure 4.7(b) and (c), significantly different intensities were observed in two *Suzaku* observations of Her X-1, conducted at different phase of the 35-d cycles. In contrast, 4U 1822−37 has such a high orbital inclination and dip that periodic dips were observed as shown in Fiugre 4.8. 4U 1626−67 was observed two times and it did not show notable time variability.

The three objects all show CRSFs. Actually, Her X-1 yielded the first detection of CRSFs (Truemper et al. 1978) at 35 keV. The feature was also studied with *Suzaku* (Enoto et al. 2008 and Asami et al. 2014), in which a 2nd harmonic. The CRSF of 4U 1626−67 was discovered at ∼30 keV by Orlandini et al. (1998), and then studied with *Suzaku*: Iwakiri et al. (2012) found evidence of cyclotron emission at a particular pulse phase. We detected the CRSF at 33 keV from 4U 1822−37, and established this object as a fourth LM-BXP.

4.3.2 GRO J1744−28

GRO J1744−28 was discovered by *CGRO* in 1995 and its pulsation was detected at ∼ 0.46 s (Finger et al. 1996). Since then, this source showed several outburst from 1995 to 1998, and was observed with *RXTE* and *ASCA* (Giles et al. 1996, Nishiuchi et al. 1999). From 1999, GRO J1744−28 became undetectable with its luminosity was below 10^{33} erg s^{-1}. On 2014 January 18,, it suddenly woke up, and brightened to ∼ 1 Crab on 2014 March 20 as presented is Figure 4.9.

The flare in 2014 was caught by MAXI on 2014 January 18, (Negoro et al. 2014), and followed by Suzaku ToO observation at the top of the flare (Figure4.9). To detect the pulsation

Table 4.3: Suzaku observation lists of high-B LMXBs

Object	ObsID	Start Date	Exposure	Nominal	ObsMode	Reference
Her X-1	100035010	2005-10-05 15:28:52	36.92/80.14	—	normal,1/8-win	a,b,c
	102024010	2008-02-21 15:03:51	0.49/34.31	XIS	0.1 s-burst,Full-win	a,b,c
	405058010	2010-09-28 18:47:33	21.36/18.92	HXD	normal,1/4-win,P-sum	c
	405058020	2010-09-29 16:48:29	24.3/22.33	HXD	normal,1/4-win,P-sum	c
	405058030	2010-09-22 00:00:18	19.92/17.43	HXD	normal,1/4-win,P-sum	c
	405058040	2010-09-22 19:02:56	21.74/19.54	HXD	normal,1/4-win,P-sum	c
	407051010	2012-09-19 08:29:31	25.54/24.8	XIS	normal,1/4-win	—
	407051020	2012-09-22 04:20:50	22.6/19.95	XIS	normal,1/4-win	—
	407051030	2012-09-24 10:21:45	23.59/23.13	XIS	normal,1/4-win	—
4U 1626−67	400015010	2006-03-09 01:18:16	102.65/93.37	XIS	normal,1/8-win	d
	405044010	2010-09-06 12:58:56	20.03/19.44	XIS	normal,1/4-win	d
4U 1822−37	401051010	2006-10-02 10:57:12	37.77/33.18	XIS	normal,1/4-win,Full-win	e
GRO J1744−28	908004010	2014-03-24 04:24:17	4.2/54.51	XIS	0.1 s-burst,1/4-win	—
GX 1+4	405077010	2010-10-02 06:43:23	99.67/95.66	HXD	normal,1/4-win	—
4U 1954+319	907005010	2012-11-01 02:39:49	60.84/53.88	XIS	normal,Full-win	f

(a) Terada et al. (2008), (b) Enoto et al. (2008), (c) Asami et al. (2014), (d) Iwakiri et al. (2012), (e) Sasano et al. (2014), (f) Enoto et al. (2014)

at low energy band and exclude the pile-up effects, the XIS were all operated with 0.1 s burst mode and 1/4 window option. The gross exposure was 150 ks and a net exposure of the XIS and HXD were 4.1 and 54 ks, respectively. This object is a second and very rare Type-II burster. As shown in Figure 4.9, about 20 Type-II bursts whose durations are ∼10 s were detected during the observation, just like the previous *ASCA* result by Nishiuchi et al. (1999). In our analysis in chapter5, we exclude these bursts and dips, and utilized only the persistent emission.

From the *CGRO* observation, not only $P_{\rm s}$ but also $\dot{P}_{\rm s}$ were measured, which yielded B=2-6×10^{11} G with the parameters (Finger et al. 1996). The estimation suggested that the magnetic field of this source is stronger than those of typical LMXBs. However, the exact value of B is not yet known, since no CRSF has been detected by the past observations. On the Corbet diagram of Figure 2.3, this source is located close to other BXPs, far from typical LMXBs, Be pulsars, and OB pulsars.

4.3.3 Symbiotic X-ray binaries (SyXBs)

Symbiotic X-ray binaries (SyXBs) are X-ray emitting binaries consisting of NSs and evolved (e.g. M-type) low-mass giant, latter having mass-loss rate close to those of high-mass stars. Two SyXBs, GX 1+4 and 4U 1954+319, both in our sample, are considered to involve strongly magnetized NSs. They show pulse period of ∼240 s and ∼20000 s, respectively, which are much longer than those of persistent sources and GRO J1744−28. In fact, 4U 1954+319 has the longest $P_{\rm s}$ all the BXPs known to date. GX 1+4 is suggested to have $B > 10^{13}$ G, as judging from its $P_{\rm s}$, $\dot{P}_{\rm s}$, and L (Makishima et al. 1988). Its X-ray spectrum is very hard, extendng to high energies like other BXPs. 4U 1954+319, which is transient source , was observed twice with *Suzaku*, one in a quiescence and the in an outburst. We do not utilize the data in a

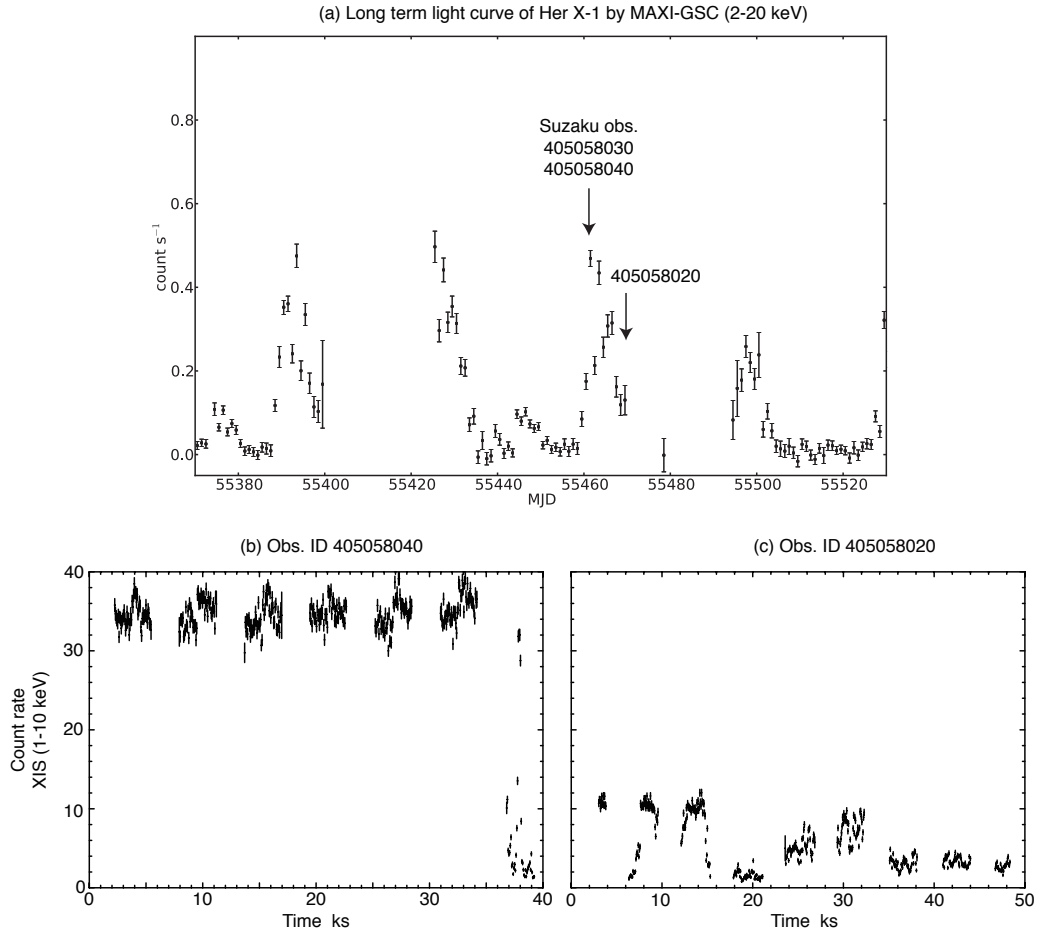

Figure 4.7: (a) A long term light curve of Her X-1 with MAXI in 2 to 20 keV band. (b) A light curve of obs. ID 405058040 obtained by *Suzaku* XIS (1-10 keV). (c) Same as panel (b) but for obs. ID 405058020.

quiescence because it was too faint to detect with HXD-PIN. Enoto et al. (2014) suggest that 4U 1954+319 have $B \sim 10^{13}$, based on it time variability and spectral properties observed on the two occasions.

In the *Suzaku* observations of the two SyXBs, the XIS was operated with the 1/4-window mode. Figure 4.10 shows their light curves and hardness obtained on these occasions. GX 1+4 was almost constant in the observation while 4U 1954+319 showed violent time variability like OB pulsars, which suggests that this source is powered by wind cature rather than disk accretion (§2.1.4). The hardness of both objects were constant during the observation. In this, we categorize 4U 1954+319 as LM-BXPs. However, it is also classified as an LPP because of its extremely long $P_{\rm s}$. Hereafter, we consider 4U 1954+319 as an LPPs.

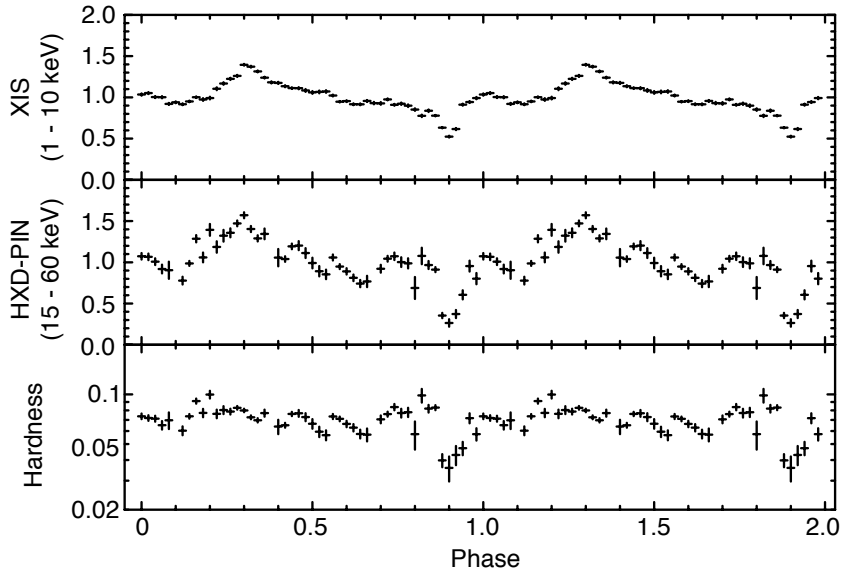

Figure 4.8: The same figure as 4.6 but for light curve of 4U 1822−37 folded with its orbital period. A dip is shown at phase∼0.9.

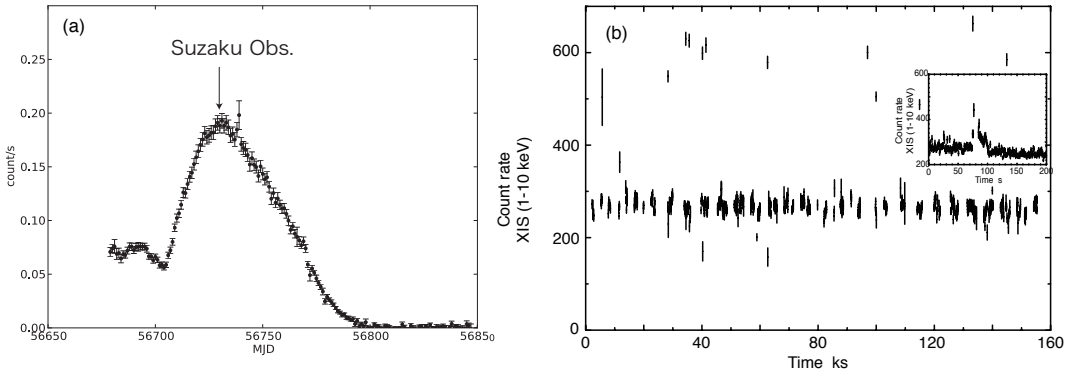

Figure 4.9: (a) A long term light curve of GRO J1744-28 with *Swift-BAT*. (b) light curve obtained with the XIS and the inset show expanded view of a Type-II burst.

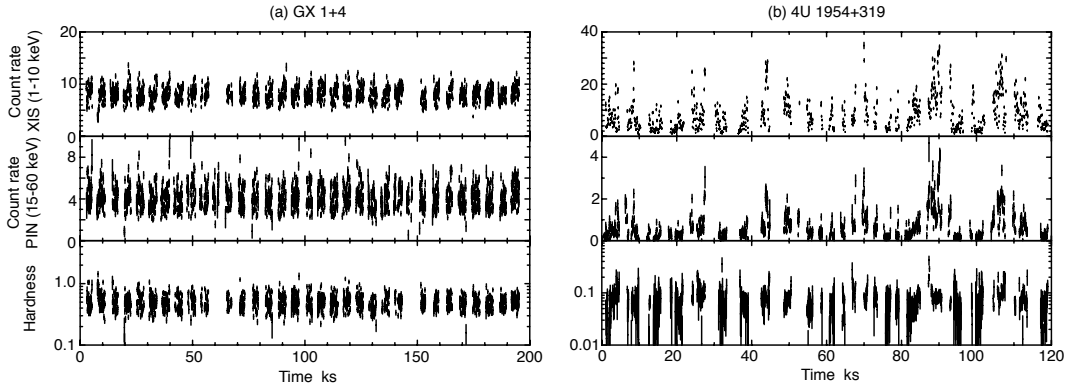

Figure 4.10: (a) light curve of GX 1+4. (b) that of 4U 1954+319. The panels are same as Figure 4.6

Chapter 5

ANALYSIS AND RESULTS

5.1 Luminosity

X-ray luminosity is one of the most fundamental parameters of an X-ray source, and is strongly connected with the mass accretion rate (e.q. 2.12). Satellite observations give energy fluxes f from objects in a certain energy band, and their L in the same band can be estimated, assuming an isotropic radiation, as

$$L = 4\pi D^2 \times f \tag{5.1}$$

where D is the distance to the object. To evaluate f, we fitted spectra with an acceptable model, and took values of D from literature. We measured f of the twenty-five BXPs (§4) and show in Table 5.1. Adopting eq.5.1, their values of L were estimated and were found to indicate a distribution shown in Figure 5.1. From the distribution, the average L of the BXPs is suggested as $\sim 10^{37}$ erg s^{-1}, and is about one order of magnitude lower than the Eddington luminosity $L_{\rm Edd}$. In the case of Be binaries and GRO J1744−28, L changes over three orders of magnitude, close to $L_{\rm Edd} \sim 10^{38}$ erg s^{-1} in outbursts while lower than 10^{35} erg s^{-1} in quiescence.

As another important parameter of NSs, we adopt $P_{\rm s}$ and study a correlation between L and $P_{\rm s}$. The values of $P_{\rm s}$ were referred from previous observation results. Figure 5.2 show a plot of L vs. $P_{\rm s}$. From the plot, less luminous objects are found to have longer $P_{\rm s}$, with an approximate relation of $P_{\rm s} \propto L^{-1}$. This generally agrees with the idea (e.g., Ghosh & Lamb 1978) that objects with higher L (have with higher accretion rate) can spin up to shorter periods. However, Be binaries have lower luminosity in quiescence than shown here, and we should consider selection bias.

Table 5.1: Observed fluxes and luminosities table of BXPs by Suzaku.

Object	ObsID	MJD	Absorbed flux (10^{-9} erg cm^{-2} s^{-1})	Non-absorbed flux (10^{-9} erg cm^{-2} s^{-1})	Distance (kpc)	Luminosity (10^{37} erg s^{-1})	P_s (s)
Her X-1	102024010	54517	5.7	5.7	6.56[(1)]	2.9	1.23771±0.00001
	405058010	55467	3.9	3.9	6.56	2.0	1.23771±0.00001
	405058020	55468	2.2	2.2	6.56	1.1	1.23771±0.00001
	405058030	55461	9.3	9.3	6.56	4.8	1.23771±0.00001
	405058040	55461	9.4	9.4	6.56	4.9	1.23771±0.00001
	407051010	56189	5.9	5.9	6.56	3.0	1.23771±0.00001
	407051020	56192	10.1	10.1	6.56	5.22	1.23771±0.00001
	407051030	56194	8.4	8.4	6.56	4.3	1.23771±0.00001
4U 1626−67	400015010	53803	0.57	0.57	9.0[(2)]	0.55	7.67795±0.00005
	405044010	55445	1.68	1.68	9.0	1.63	7.67743±0.00003
4U 1822−37	401051010	54010	1.45	1.46	2.3[(3)]	3.0*	0.5924337±0.0000001
GRO J1744−28	908004010	56740	27.4	32.6	8.5[(4)]	28.3	0.467044±0.000001
GX 1+4	405077010	55471	3.19	3.73	4.5[(5)]	0.91	159.95±0.01
4U 1954+319	907005010	56232	0.6	0.62	1.7[(6)]	0.022	20500±1000
1A 1118−61	403049010	54846	13.2	13.4	5.0[(7)]	4.02	407.5±0.5
	403050010	54859	1.63	1.63	5.0	0.52	407.4±0.5
A 0535+26	100021010	53627	0.96	0.99	2.0[(8)]	0.047	103.36±0.04
	404054010	55067	1.05	1.12	2.0	0.054	103.48±0.02
	404055010	55292	28.2	28.2	2.0	1.35	103.31±0.02
EXO 2030+375	402068010	54234	9.66	10.5	7.1[(9)]	6.35	41.410±0.005
	407089010	56070	1.52	2.07	7.1	1.25	41.285±0.005
GRO J1008−57	902003010	54434	3.98	4.17	5.0[(10)]	1.25	93.74±0.015
	907006010	56251	2.76	2.85	5.0	8.55	93.63±0.01
GX 304−1	406060010	55957	14.7	15.2	2.4[(11)]	1.05	274.88±0.04
	905002010	55421	31.2	32.2	2.4	2.23	275.41±0.06
KS 1947+300	908001010	56587	7.18	7.34	9.5[(12)]	7.95	18.809±0.002
XTE J1946+274	405041010	55480	0.55	0.58	9.5[(13)]	0.63	15.75±0.01
4U 1907+09	401057010	53857	1.06	1.21	5.0[(14)]	0.36	441.3±0.2
	402067010	54209	0.41	0.53	5.0	0.16	441.2±0.3
4U 1538−52	407068010	56149	1.25	1.33	6.4[(15)]	0.65	526±2
Vela X-1	403045010	54634	7.35	7.94	1.9[(16)]	0.19	283.2±0.1
GX 301−2	403044010	54703	1.77	2.55	4.1[(17)]	0.51	688±1
	403044020	54836	5.94	7.88	4.1	1.59	685.5±0.5
Cen X-3	403046010	54808	4.6	4.93	10[(18)]	5.92	4.80±0.01
OAO1657−415	406011010	55830	1.29	3.60	7.1[(19)]	2.18	36.94±0.05
LMC X-4	702036020	54561	1.16	1.16	55[(20)]	42.1	13.5096±0.0001*
	702037010	54507	1.16	1.16	55	42.1	13.5091±0.0001*
	702038010	54480	1.16	1.16	55	42.1	13.5087±0.0002*
SMC X-1	706030020	55669	2.40	2.40	60[(20)]	10.4	0.70107±0.00001
	706030050	55706	2.44	2.44	60	10.5	0.70236±0.00001
4U 0352+30	407088010	56166	1.1	1.1	0.7[(21)]	0.0065	835±1
4U 0114+65	406017010	55763	0.61	0.85	4.5[(22)]	0.21	9381±30
4U 2206+54	402069010	54236	0.51	0.51	2.6[(23)]	0.042	5543±20
4U 1909+07	405073010	55502	0.51	0.55	7.0[(24)]	0.36	604±1

$*$ Hung et al. (2010)

$\star$ Sasano et al. (2014)

(1) Reynolds et al. (1997), (2) Chakrabarty (1998), (3) Cowley et al. (2003), (4) Nishiuchi et al. (1999), (5) Hinkle et al. (2006), (6) Masetti et al. (2006), (7) Janot-Pacheco et al. (1981), (8) Steele et al. (1998), (9) Camero Arranz et al. (2005), (10) Riquelme et al. (2012), (11) Parkes et al. (1980), (12) Negueruela et al. (2003), (13) Verrecchia et al. (2002), (14) Cox et al. (2005), (15) Reynolds et al. (1992), (16) Nagase et al. (1986), (17) Kaper et al. (2006), (18) Sherwood & Plaut (1975), (19) Audley et al. (2006), (20) Westerlund (1997), (21) Telting et al. (1998), (22) Reig et al. (1996), (23) Blay et al. (2006), (24) Morel & Grosdidier (2005)

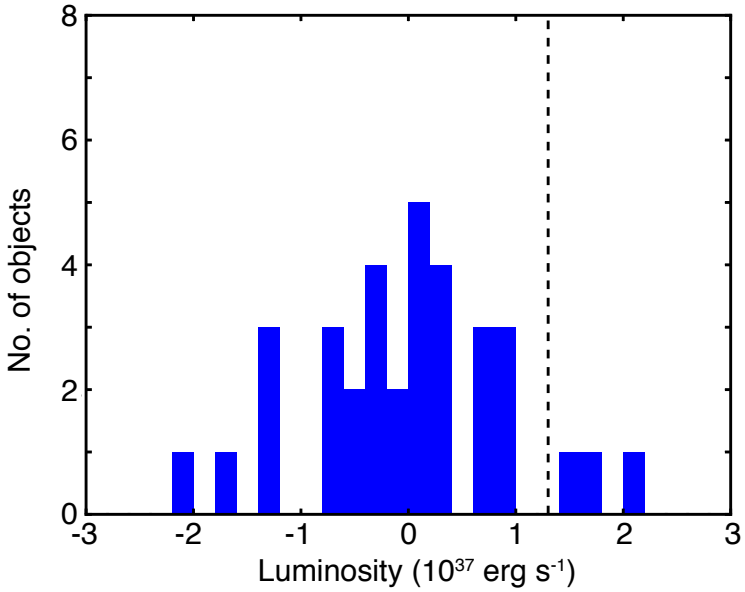

Figure 5.1: Histogram of the 1-60 keV luminosities of our sample. The dotted line means the Eddington luminosity for a 1.4 $M_{\odot}$ objects.

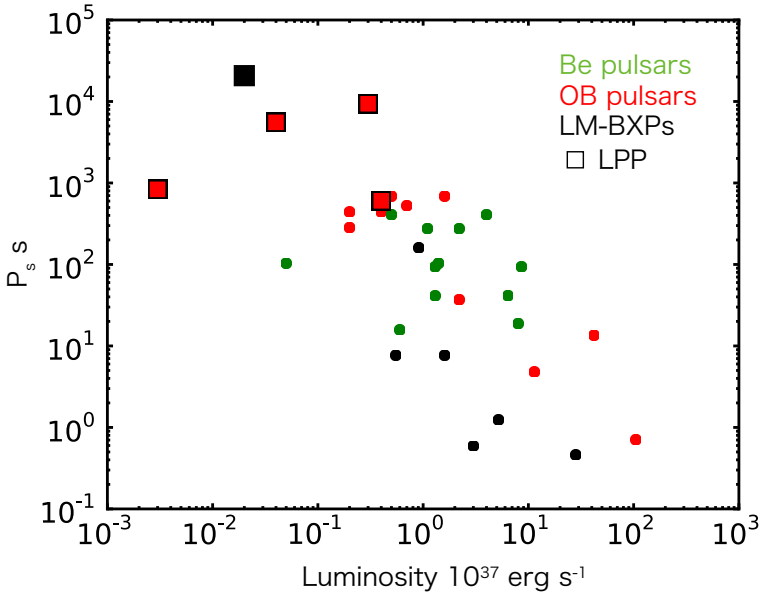

Figure 5.2: A scatter plot between L from 1 to 60 keV obtained by *Suzaku* and P_s. Red points mean OB pulsars, green Be pulsars, black LM-BXPs. The square points mean LPP objects.

5.2 Pulse Properties

At present, about 100 BXPs are known, and their P_s are much longer than those of typical radio pulsars as a result of angular momentum exchange with the accreting matters (§2.1.4). The pulsations are very important to understand not only the accretion physics but also magnetic field strength. In this section, we study pulse properties of our sample BXPs.

5.2.1 How to measure P_s and pulse profiles

Taking as an example the Be-binary 1A1118−61 with $P_s \sim 400$ s, let us described how we analyzed its *Suzaku* data for the pulse properties. After correcting the individual photon arrival times for the motions of the Earth and the spacecraft, a light curve was obtained as in Figure 5.3(a). Thus, the ~ 400 sec pulses are clearly visible. To precisely measure P_s, we calculated a power spectrum from the light curve, and obtained the result as shown in Figure 5.3(b). Thus, four prominent peaks are seen in the power spectrum at $\sim 2.4\times10^{-3}$, 4.8×10^{-3}, 7.2×10^{-3} and 9.6×10^{-3} Hz. Clearly, the strongest peak at 2.4×10^{-3} Hz, corresponding to $P_s \sim 416$ s, is the fundamental with the other three all higher harmonics. Since the interval of the frequency in this power spectrum is 2.5×10^{-5} Hz, P_s has an uncertainty by ~ 40 s.

To determine P_s more precisely, periodograms provide the best way. We hence searched P_s of 1A 1118−61 with a periodogram. As shown in Figure 5.3(c), the sharp peak was detected at 407.5 s, together with several side lobes by the satellite orbit. From the width of the peak, the statistical error of P_s was determined as ± 0.5 s, so that measuring with a periodogram provides a much more accurate determination of P_s than a power spectrum.

Although P_s of 1A 1118−61 remained constant during the observation, sometimes P_s varied in a single observation due to the binary orbital motion. Figure 5.4 show light curve of Her X-1 and deviations of peak P_s obtain with periodograms in each continuous time interval. The values of P_s thus vary according to the pular's orbital motion. After correcting for this effect, the pulse period became constant at ~ 1.23771, as presented in blue in Figure 5.4(b).

Adopting P_s obtained with the periodogram, we study pulse profiles. Since P_s is in the range of 1-10^3 s and a typical observation lasts for 10-100 ks, a folding procedure folds 10-10^5 pulses into a single profile as in Figure 5.3 On the observation of 1A 1118−61, the net exposure is 24 ks for the XIS and P_s is 407.5 s so that ∼60 interval light curves are folded. In Figure 5.3(d), the folded light curve namely, pulse profile is shown.

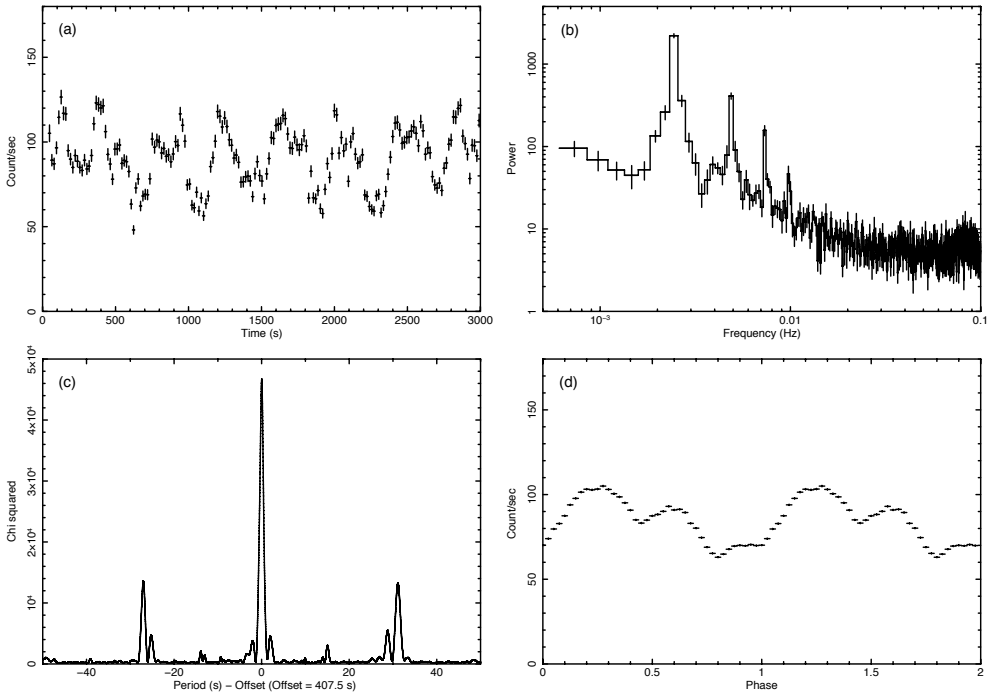

Figure 5.3: (a) A background subtracted light curve of 1A 1118-61 with the XIS (1 - 10 keV). (b) A power-spectrum of the light curve. (c) A periodogram of the light curve. (d) pulse profile of 1A 1118-61 obtained from the light curve.

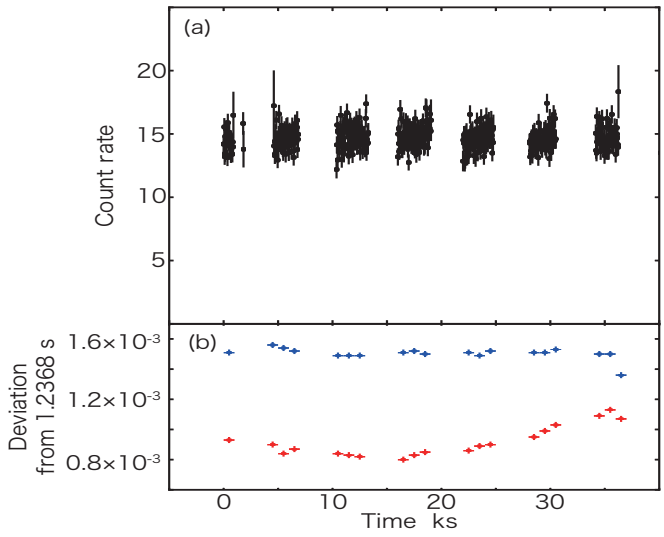

Figure 5.4: (a) A background subtracted 15-60 keV light curve of Her X-1 taken with the HXD-PIN. (b) Variations of P_s in the observations Red points mean raw results while blue those after correcting orbital Doppler effects.

5.2.2 Pulse fraction

To evaluate pulse profiles quantitatively, we define pulse fraction PF with the maximum and minimum count rate, $C_{\max}$ and $C_{\min}$, respectively, as

$$\mathrm{PF} = \frac{C_{\max} - C_{\min}}{C_{\max} + C_{\min}}. \tag{5.2}$$

In the case of Figure 5.3(d), we obtain $C_{\rm max}$=104±0.4 ,$C_{\rm min}$ is 63.0±0.3, and hence PF=0.243±0.003. Table 5.1 shows the values of $P_{\rm s}$ of the 25 BXPs measured with *Suzaku*.

Generally, pulse profiles of BXPs strongly depend on energies. Figure 5.5 presents the folded pulse profiles of 1A 1118−61, obtained with the XIS and HXD on two occasions and shown in 6 energy bands covering 1-60 keV. Thus, the profile is double-peaked at low energies, which become single-peaked towards higher energies. The PF increases from 0.2 at 1-3 keV to 0.5 at 45-60 keV, by a factor of 2.5.

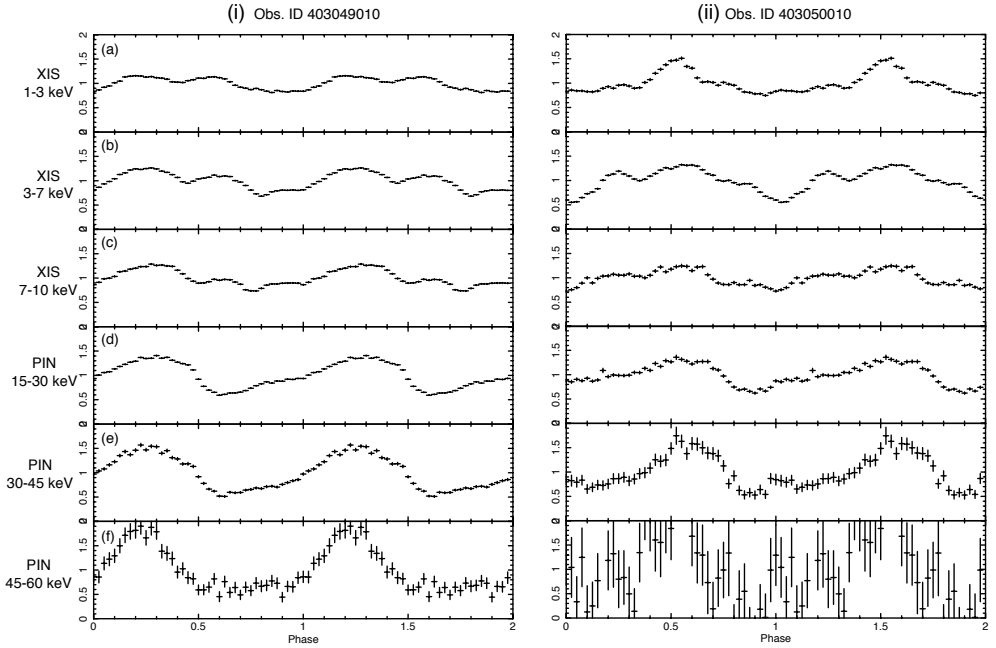

Figure 5.5: (i) Folded pulse profiles of 1A 1118−61 (obs.ID 403049010) in X-ray outburst. (ii) Those of obs. ID 403050010 in a low luminosity. The energy ranges are: (a) 1-3 keV, (b) 3-7 keV, (c) 7-10 keV, (d) 15-30 keV, (e) 30-45 keV, and (f) 45-60 keV. Each profile is normalized by the average intensity.

We studied the pulse profile of 1A 1118−61 with the XIS band (1 - 10 keV) in Figure 5.3. As described in §2.3.3, it is well known that the pulse profiles strongly depend on energies. We divided six energy bands between 1.0 and 60 keV (1.0 to 3.0 keV, 3.0 to 7.0 keV, 7.0 to 10.0 keV, 15 to 30 keV, 30 to 45 keV and 45 to 60 keV) and created six pulse profiles with the energy bands are shown in Figure 5.5. The pulse profiles of Figure 5.5 are normalized with average count rate. As shown in Figure 5.5(i)-(a)∼(c), the pulse profiles at lower energy bands show double peaks at ∼ phase 0.2 and 0.6. On the other hands, only one peak appear at ∼ phase 0.2 in those at higher energy bands and the profiles changed. From the Figure 5.5(i)-(a) and (f) and e.q.5.2, the PF is estimated as ∼0.2 and 0.5, respectively and the PF of the 45 to 60 keV band became 2.5 times larger than that of the 1.0 to 3.0 keV band. Energy dependence of the PF is suggested by the results.

To study energy dependence of pulse profiles more extensively, we analyzed them in 14 ∼ 17 energy bands with the XIS and HXD-PIN. In Figure 5.6 and 5.7, not only the result of 1A 1118−61 but also those of the other BXPs in our sample are shown. The PF depends mostly

on the energy, and generally increase towards higher energies, like in 1A 1118−61. No object shows monotonic decrease of the PF. To evaluate energy dependence of the PF quantitatively, we fitted the PF spectra with constants and obtained deviations between the spectra and the constant χ^2. χ^2 means dependency on energy and it is close to 1.0 when the dependency is small while it become large in a strong dependency. In this analysis, we exclude the spectra of GX 301−2 (obs.ID 403044010) and OAO 1657−415 because they have large errors at 1-4 keV by strong absorption. The plot of PF at 15-30 keV and χ^2 are shown in Figure 5.8. Although most of BXPs exhibit positive correlation between them, LPPs (square mark) show large PF and small χ^2 and deviated from the correlation. LPPs have weak energy dependence of PF and large PF so that pulse properties of LPPs are different from those of other BXPs.

The evaluation with χ^2 largely depends on statistics. As another attempt to study the energy dependence of the PF spectra, we may consider their maxima, PF_{max}, and minima, PF_{min}, and take their ratios. For example, PF_{max} and PF_{min} are 0.31 and 0.75, respectively, for KS 1947+30 from Figure 5.6. Figure 5.8 (b) shows the derived PF_{max}/PF_{min} reties, against the PF value in 15-30 keV (the same as panel a). Although the LPPs have become closer to the other objects than in Figure 5.8(a), they are still distinguished by their small ratios as PF_{max}/PF_{min}, except one object (4U 1909+07), which has the weakest LPP characteristics.

From these two plots, we suggest the LPPs in our sample (or at least 4 of them) can be characterized by their PFs which are considerably less energy dependent, compared to the other BXPs.

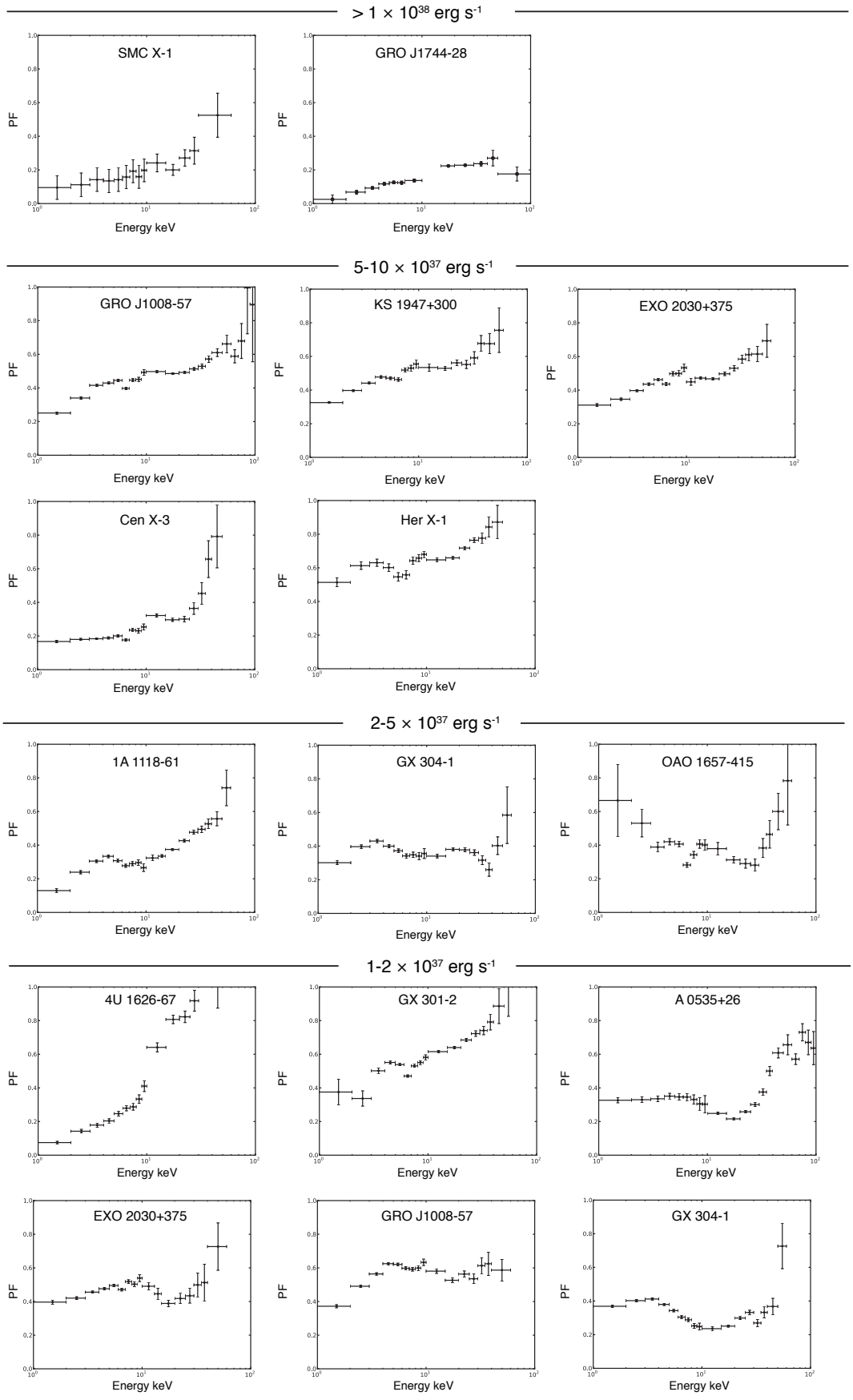

Figure 5.6: Pulse-fraction spectra.

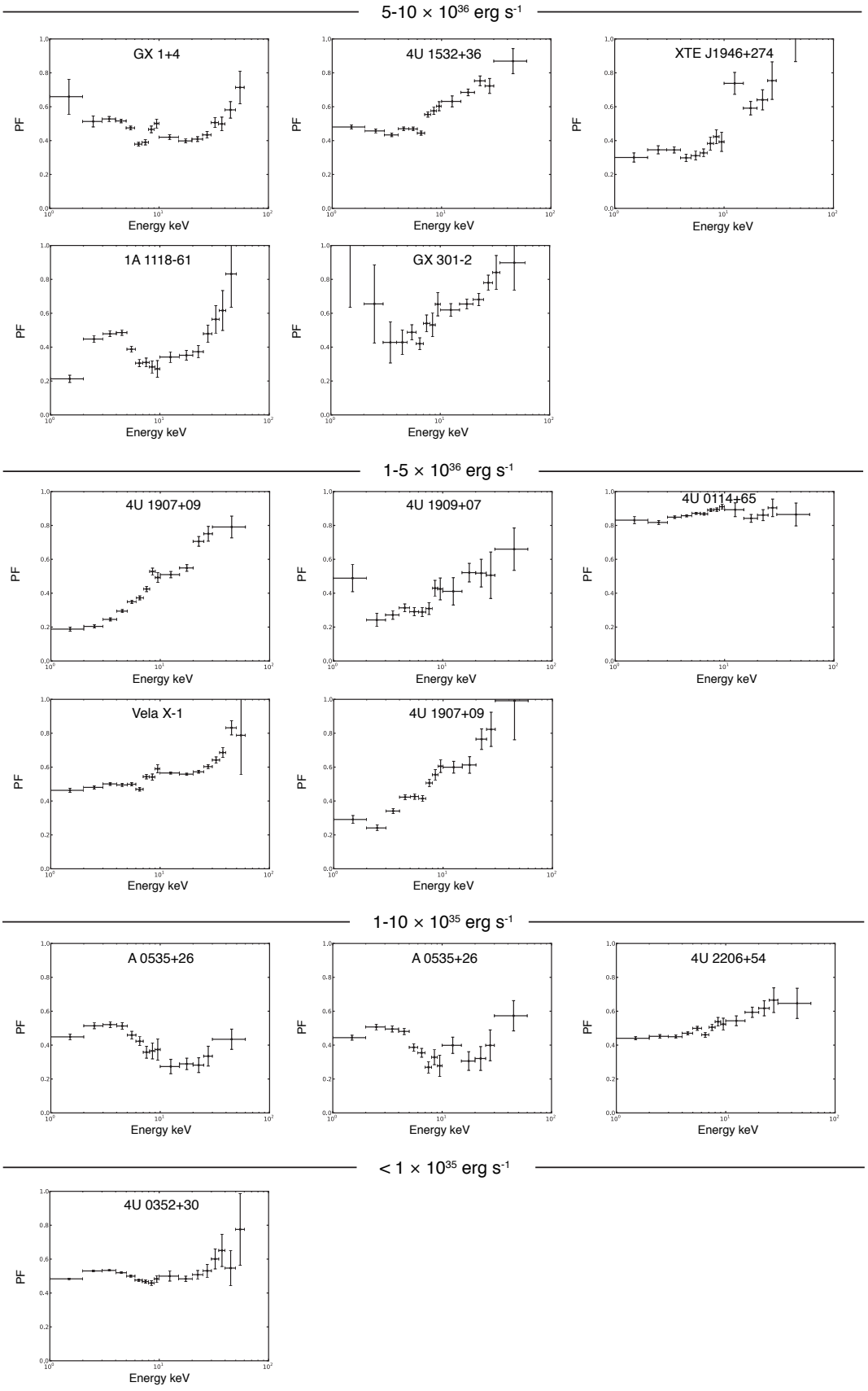

Figure 5.7: The same as Figure 5.6 but pulse-fraction spectra for less luminous samples.

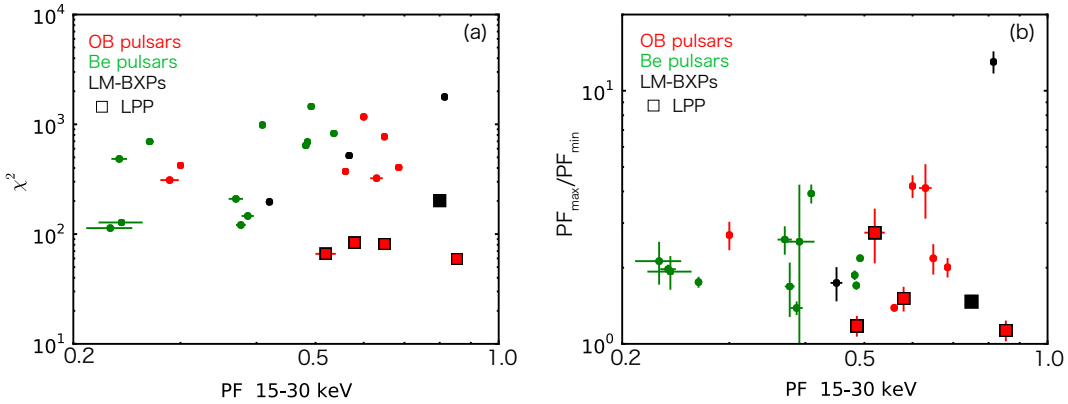

Figure 5.8: (a) The plot of PF at 15-30 keV vs. χ^2. Green points are Be binaries, reds are OB binaries, and blacks LM-BXPs. The square points are LPP. (b) The same as panel (a), but abscissa is replaced with the PF_{max}/PF_{min} ratio.

5.3 Spectral Analysis

As described in §2.4.1, X-ray spectra of BXPs contain important information on various quantities, including B, electron temperature T_e in accretion columns, and distribution of matters which surround the NSs. In this section, we show results of spectral analysis of our sample objects defined in §4

5.3.1 Observed spectra

With the XIS, HXD-PIN and HXD-GSO, we obtained X-ray spectra of our sample BXPs. To approximately remove the instrument responses, ratios between the raw spectra and a power-law model of photon index 2 are shown in Figure 5.9 and 5.10. The XIS data in 1.6-2.5 keV and those of PIN below ∼15 keV were removed, because of the larger calibration uncertainties (§3.2) and the increased thermal noise (§3.4), respectively. We ignored data below 1 keV where X-ray signals are weak in most of the objects.

The observed spectra exhibit three common features. First, X-ray photons are absorbed by interstellar media and circum-source gases, so that the spectra become weaker below ∼3 keV. The interstellar media between the solar system and an observational target, with a typical column density of $\sim 10^{21-22}$ cm^{-2}, photoelectrically absorb low-energy X-ray photons. The local absorption is most prominent in OB binaries, because their massive primaries launch dense stellar winds. For example, GX 301−2 and OAO 1657−415 (Column 5:Row 2 in Figure 5.9, 2:3 in Figure 5.10, and 4:3 in Figure 5.9) are the most absorbed objects. In these objects, the spectra also show a dip above ∼7 keV, which is due to the presence of Fe-K edge at ∼ 7.1 keV. To reproduce effects of absorption on the spectra, we adopt **phabs** as a multiplicative model (§2.3.1,).

As a second feature, emission lines at ∼6-7 keV are observed in the spectra. These are fluorescence Fe-K$_\alpha$ lines, emitted by circum-source materials when they absorb continuum X-rays (with >7.1 keV energies) from the NS. Strengths of the lines are different from object to object. The spectra of GX 301−2 and OAO 1657−415 exhibit very strong Fe-K lines, while the feature is weak in 4U 0352+30 and 4U 2206+54 in contrast. Generally, objects with higher absorption show stronger iron lines. The spectra of Cen X-3 exhibit not only the neutral Fe-K line at 6.4 keV, but also those from ionized iron species; helium-like (He-like; ∼6.7 keV) and hydrogen-like (H-like; ∼6.9 keV) lines (§2.3.1).

The continuum shape,very hard up to ∼20 keV and then falls off steeply above, is the third feature, and is clearly different from those of other classes of NS binaries. More specifically, in <20 keV these BXPs show photon indices (§2.3.1) of Γ=0.5-1.0, which is much harder than those of LMXBs in the hard state (Γ=1.7-2.0; §2.2). At higher energies fluxes decrease rapidly, with the spectral cutoff points at ∼20-30 keV. These cutoff energies are considerably lower than

those of the LMXBs (50-100 keV).

In addition to the above three features, cyclotron absorption (CRSF; §2.3.2) clearly appeared in the hard X-ray band (> 10 keV) of many (if not all) spectra. The minimum and maximum CRSF energies are ∼20 keV in 4U 1907+09 and ∼70 keV in GRO J1008−57, respectively. Thirteen out of the twenty five objects in our sample have been well known to exhibit CRSFs; we select **cyclabs** model to fit the CRSF (§2.3.1).

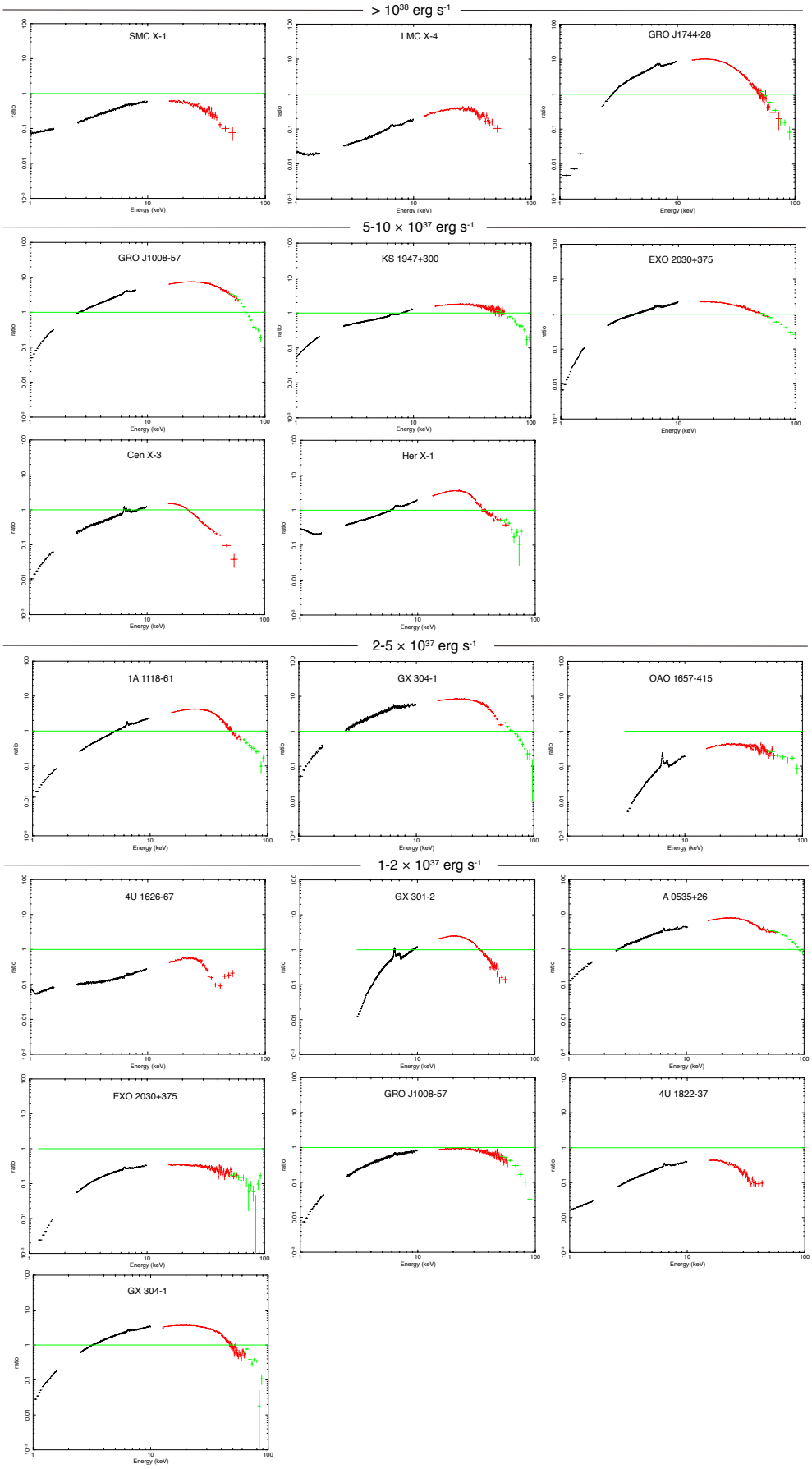

Figure 5.9: Suzaku spectra of BXPs that are more luminous than 10^{37} erg s^{-1} in our sample , shown as a ratio to a power-law model with Γ=2.0. Black, red and green indicate data from the XIS, PIN and GSO, respectively.

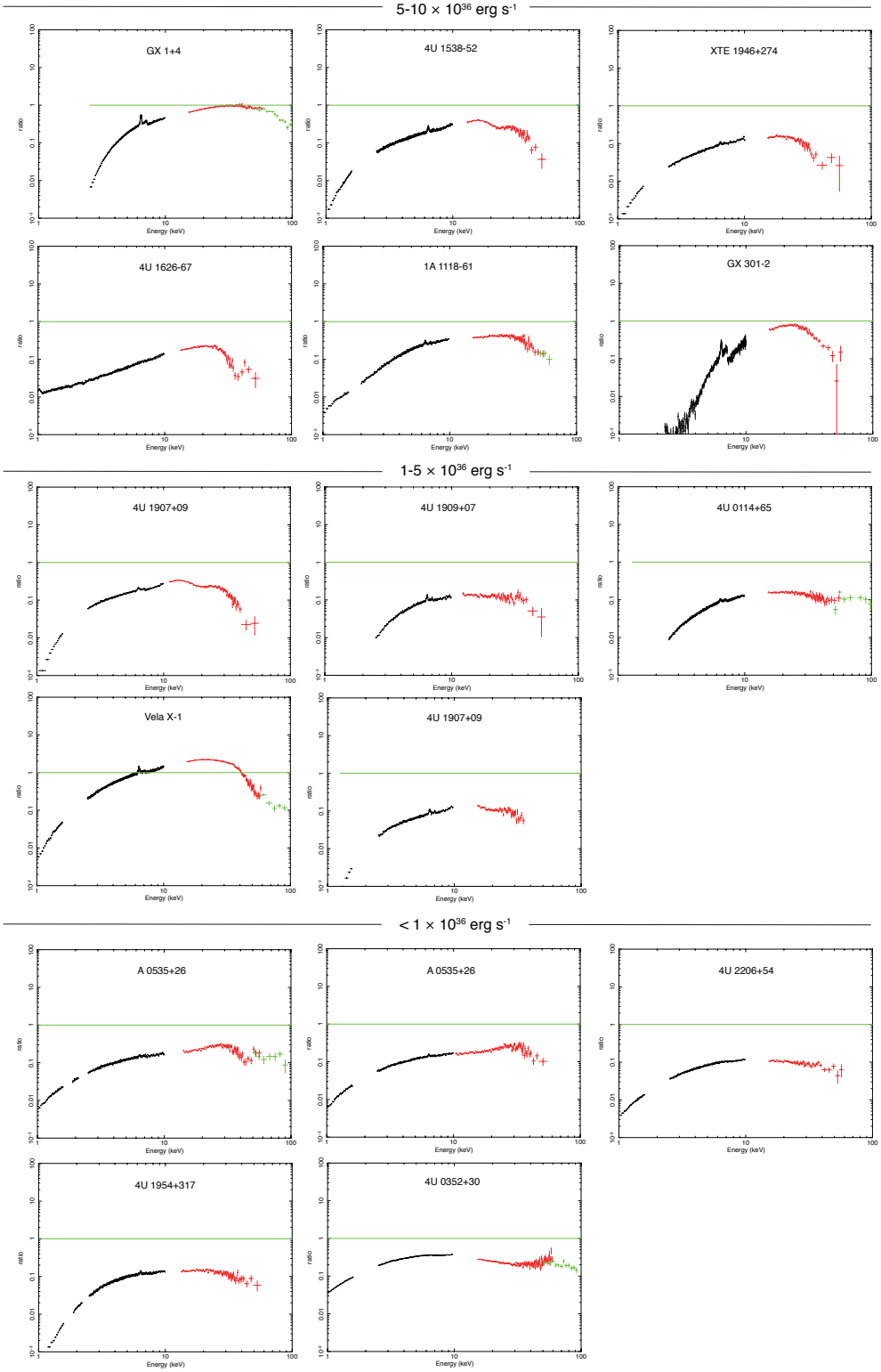

Figure 5.10: The same as Figure 5.9 but for less luminous (<10^{37} erg s^{-1}) sources.

5.3.2 Hardness ratio

To roughly quantify of the spectral shapes in Figures 5.9 and 5.10, we evaluate energy fluxes at several energy bands. Since all objects have been detected with HXD-PIN, their 15-60 keV

fluxes were calculated through spectral model fitting to be described in §5.3.3. Twenty objects were detected also with HXD-GSO, which yielded fluxes between 60 and 100 keV. Thus, we define spectral hardness as ratios between the flux in 15-60 keV and that in 60-100 keV. The reason why we do not use the XIS counts is that the spectra in that energy range is relatively similar, and apparent differences among the sample is mainly due to different absorption.

Figure 5.11(a) show a plot of L vs. the hardness. There, luminous ($> 10^{36}$ erg s^{-1}) objects exhibit rather low hardness below 0.2, as a result of their weak HXD-GSO signals. In contrast, some lower-L objects show significantly higher hardnesses (> 0.2) than the rest of our sample. They are 4U 0352+35, 4U 0114+65, GX 1+4, and A 0535+26 in quiescence. Especially, 4U 0114+65 and 4U 0352+35, which are largely deviated, are also characterized by very long $P_{\rm s}$.

Given these two examples, we considered correlation between $P_{\rm s}$ and the hardness, and show the results in Figure 5.11(b). From the plot, a positive correlation is indeed observed. Furthermore, the BXPs with confirmed CRSFs, indicated in blue, generally exhibit low haddness, < 0.2. This is because their signals get rather weak in energies near and above their cyclotron resonances, possibly due to the presence (confirmed in some cases) of higher harmonics. These effects of the CRSF are studied in §5.3.4.

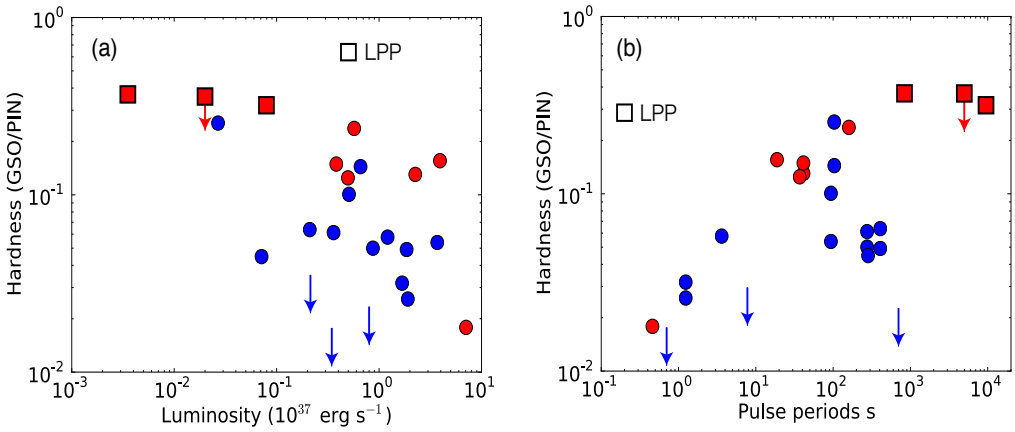

Figure 5.11: The spectral hardness, plotted against L (panel a) and $P_{\rm s}$ (panel b). Blue and red points indicate objects with and without the detected CRSFs, respectively. The square marks represent LPP objects.

5.3.3 Selection of spectral models

To evaluate spectral shapes more quantitatively, we need to fit the spectra with some appropriate models (§2.3.1). Before actually conducting model fitting to the spectra, several technical remarks should be made. First, we fit the XIS and the HXD data simultaneously: we employ a common spectral model, convolved it with the XIS response to be compared with the XIS data, and do the same procedure for the HXD data (both PIN and GSO). Then, the fit goodness is evaluated by summing up chi-squares from the XIS, HXD-PIN, and HXD-GSO fits. For this purpose, the XIS and HXD spectra were accumulated over exactly the same time intervals

for each source. The XIS vs. HXD cross normalization (which originally should by 1.00) were fixed at 1.16 and 1.18, for the "XIS nominal" and "HXD nominal" pointing positions (§3.1), respectively, as determined by in-orbit calibrations in 2005 using the Crab Nebula as a calibration source (Kokubun et al. 2007). Second, we exclude the 1.6-2.5 keV and <15 keV ranges of the XIS and HXD-PIN spectra, respectively, for the reasons described in §5.3.1. Finally, we include systematic errors of 1%, because most of the spectra have high signal statics.

Taking 4U 1538−52 as an example, we explain in Figure 5.12 the procedure of arriving at a correct spectral model. Considering previous works (e.g., White et al. 1983), we started from **phabs×cutoffPL** (§2.3.1) as the simplest empirical continuum model. However, the residuals between the data and the model are so large at $\sim$ 6.4 keV and 8-20 keV that the model is not acceptable. To reproduce the former, to be identified with Fe-Kα (6.4 keV), Fe-Kβ (7.05 keV), and Ni-Kα (7.5 keV) lines, we added to the model three Gaussians, of which all the model parameters, the center energy, the width σ, and normalization are left free (Figure5.12c). However, the residuals are still large at the higher energy band. This source has been know to exhibit a CRSF at $\sim$ 20 keV (Clark et al. 1990). We therefore multiplied the model with a **cyclabs** factor (§2.3.2), with its resonance energy $E_{\rm cyc}$, optical depth D, and width W left free. With **phabs×cutoffPL×cyclabs** including the three Gaussians, the fit was somewhat improved (Figure 5.12d), but the positive residuals are still significant at ∼17 keV.

As described in §2.4.1, §5.1 and §5.3.2, a Wien hump appears in X-ray spectra of BXPs. A s result, the spectrum often has a slightly concave curvature in 5-15 keV, in disagreement with the convex shape of cutoffPL. We hence added a Wien-hump component to the model and improved it model as

$$\textbf{phabs} \times (N_{\rm p} \cdot E^{+\Gamma_{\rm p}} + N_{\rm n} \cdot E^{-\Gamma_{\rm n}}) \times \exp(-E/kT) \times \textbf{cyclabs} \tag{5.3}$$

Here, the new continuum, the sum of two **cutoffPL** components with a common cutoff factor, is the **NPEX** model described in §2.3.1. In this model, $\Gamma_{\rm p}$ is fixed at 2 to present the Wien hump, while $\Gamma_{\rm n}$ is a free parameter. In the $\nu F\nu$ form, square of the energy is multipled to eq. 5.3, and hence **NPEX** is written as

$$\textbf{phabs} \times (N_{\rm p} \cdot E^{2+\Gamma_{\rm p}} + N_{\rm n} \cdot E^{2-\Gamma_{\rm n}}) \times \exp(-E/kT) \times \textbf{cyclabs}. \tag{5.4}$$

As shown in Figure 5.12(a) and (e), this model has successfully reproduced the XIS and HXD-PIN spectra of 4U 1583−52 in a consistent manner, with χ^2_ν=1.01 for ν=312. Hereafter, we adopt the **NPEX** model to represent the continuum component of our sample BXPs.

The model of eq. 5.3 was applied to all the spectra in our sample. (For the data of GX301−2, 1A1118−61, and GRO J1008−57, the width W was fixed at 12 keV because their CRSF struc-

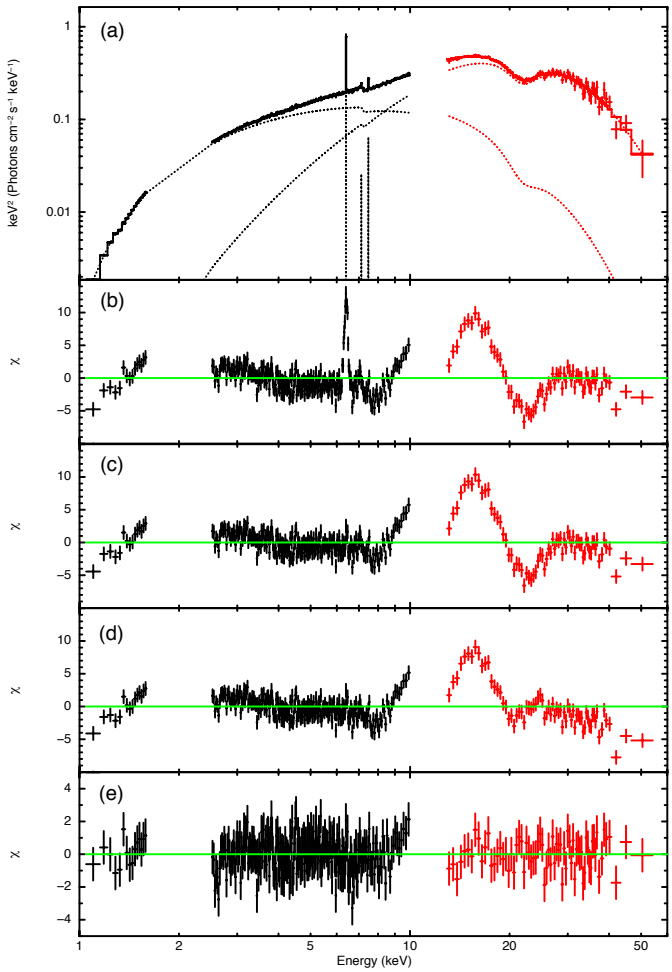

Figure 5.12: (a) $\nu F\nu$ spectra of 4U 1538−52 with phabs×NPEX×cyclabs and three Gaussians. The results are shown after removing the instrumental responses through deconvolution, so that the lines appear narrower than real detecter resolution. (b) Residual with phabs×cutoffPL. (c) When 3 Gaussians are added to explain the Fe and Ni lines. (d) Cyclabs model was added to model (c). (e) Same model as panel (a).

tures are weak.). The fit was mostly acceptable, but it failed in some cases, because a soft excess appeared below ∼2 keV. The best example is the spectra of Her X-1 presented in Figure 5.13. There, panel(b) show residuals against the model of eq. 5.3 which was determined using the energy range of >2.5 keV, where the soft excess is seen very significantly. We hence added a blackbody (**BB**) model, and a broadened Gaussian centered at ∼1 keV, which were both identified by previous works (Endo et al. 2000). For objects which show excesses at low energies, we hereafter adopt the NPEX plus **BB** modeling. Figure 5.14 shows the fit results (in $\nu F\nu$ form) of 18 spectra of the 12 CRSF objects, using eq. 5.3 consisting of the **NPEX** continuum, the low-energy absorption, the **cyclabs** factor, and sometimes the soft **BB**. The model has been successful on all the spectra. For reference, residuals obtained without including the **cyclabs** factor also shown, to visualize the CRSF structure.

Some low-luminosity sources,which are not included in Figure 5.14 show two peaks in their $\nu F\nu$ spectra, as exemplified by 4U 0352+30 (X-per) in Figure 5.15. In such exceptional cases,

the NPEX fit was unsuccessful (Figure 5.15middle), because the two cutoff-PL continua are constrained to have the same exponential factor. Therefore, we modified **NPEX** to a double cutoff form to be called "modified **NPEX** model", expressed as

$$\text{phabs} \times (N_{\rm p} \cdot E^{+\Gamma_{\rm p}} \cdot \exp(-E/kT_{\rm p}) + N_{\rm n} \cdot E^{-\Gamma_{\rm n}} \cdot \exp(-E/kT_{\rm n})), \tag{5.5}$$

where $\Gamma_{\rm p}$ is again fixed to 2 like in **NPEX**. This model was approximately acceptable, as shown in Figure 5.15 (top and bottom). We applied this modified **NPEX** model for all of our sample spectra, including those which were already fitted successfully with **NPEX**. The results of this modified **NPEX** fit are shown in Figure 5.16 and 5.17, covering all the spectra in our sample. (There, residuals from the **NPEX** fit are also shown for comparison.) Thus the modified **NPEX** model is acceptable for all our sample including 4U 0352+30.

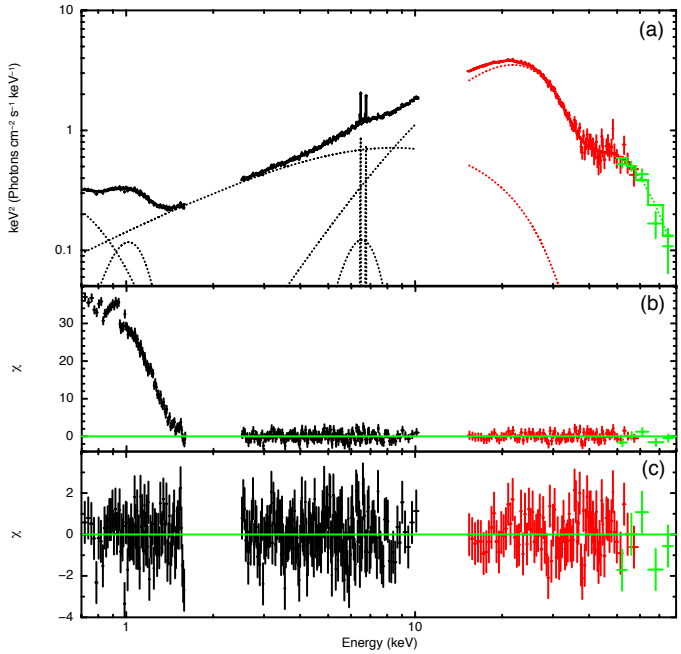

Figure 5.13: (a) $\nu F\nu$ spectra of Her X-1 together with the best-fit model, **phabs**×**NPEX**×**cyclabs** plus **BB** and board Gaussian components. (b) Residuals with phabs×NPEX×cyclabs above 2.5 keV. (c) Those with the model of panel (a).

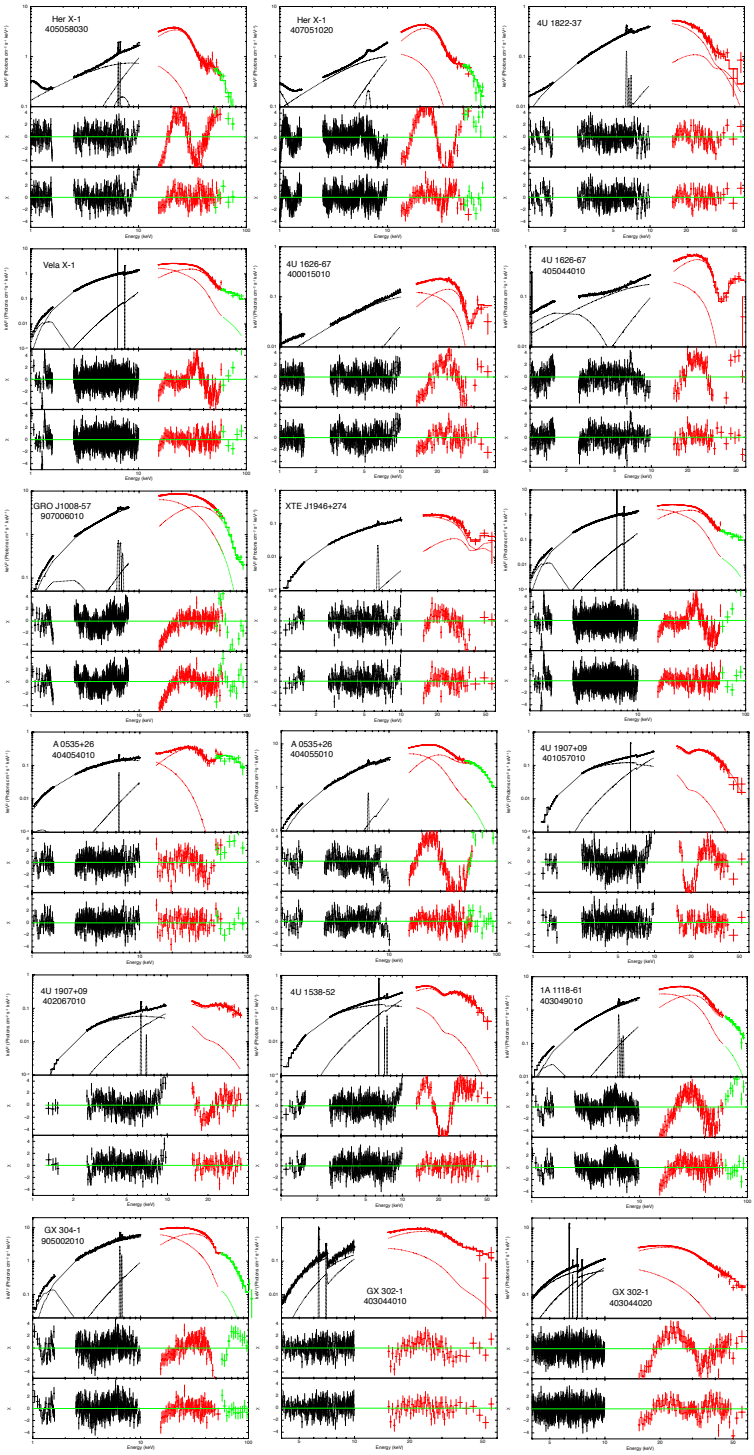

Figure 5.14: $\nu F\nu$ spectra of CRSF sources. middle panels shows residuals against the **phabs**×(**NPEX**+**BB**) mode, without cyclotron absorption factor. Bottom shows those when the **cyclabs**.

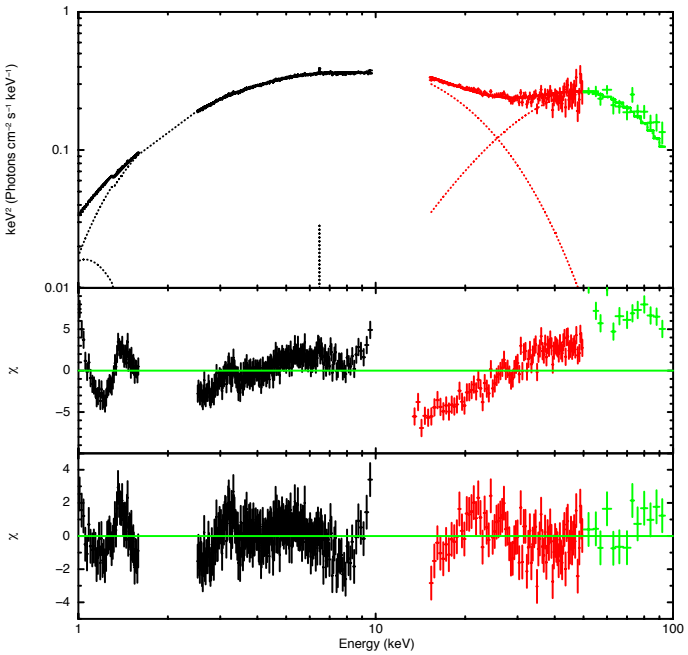

Figure 5.15: Model fitting results of 4U 0352+30. $\nu F\nu$ spectra with acceptable model (top panel), residuals against the **NPEX** model (middle), and those with the modified **NPEX** model (bottom)

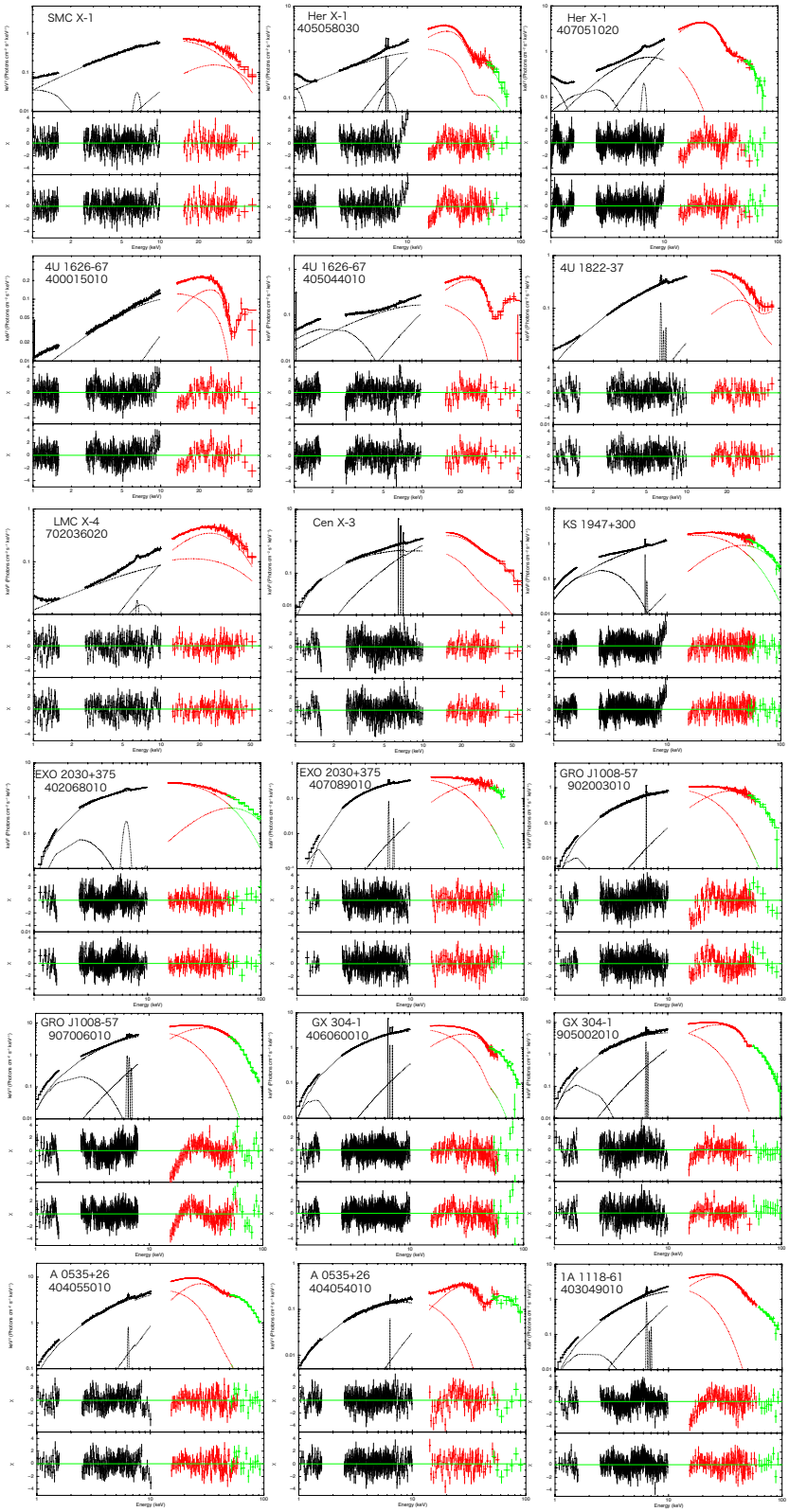

Figure 5.16: *νFν* spectra of all our sample spectra with the best fit model (top), residuals against **NPEX** (middle), and those against modified **NPEX** (bottom). Like in Figure 5.14, the **cyclabs** factor and the soft **BB** are included when necessary.

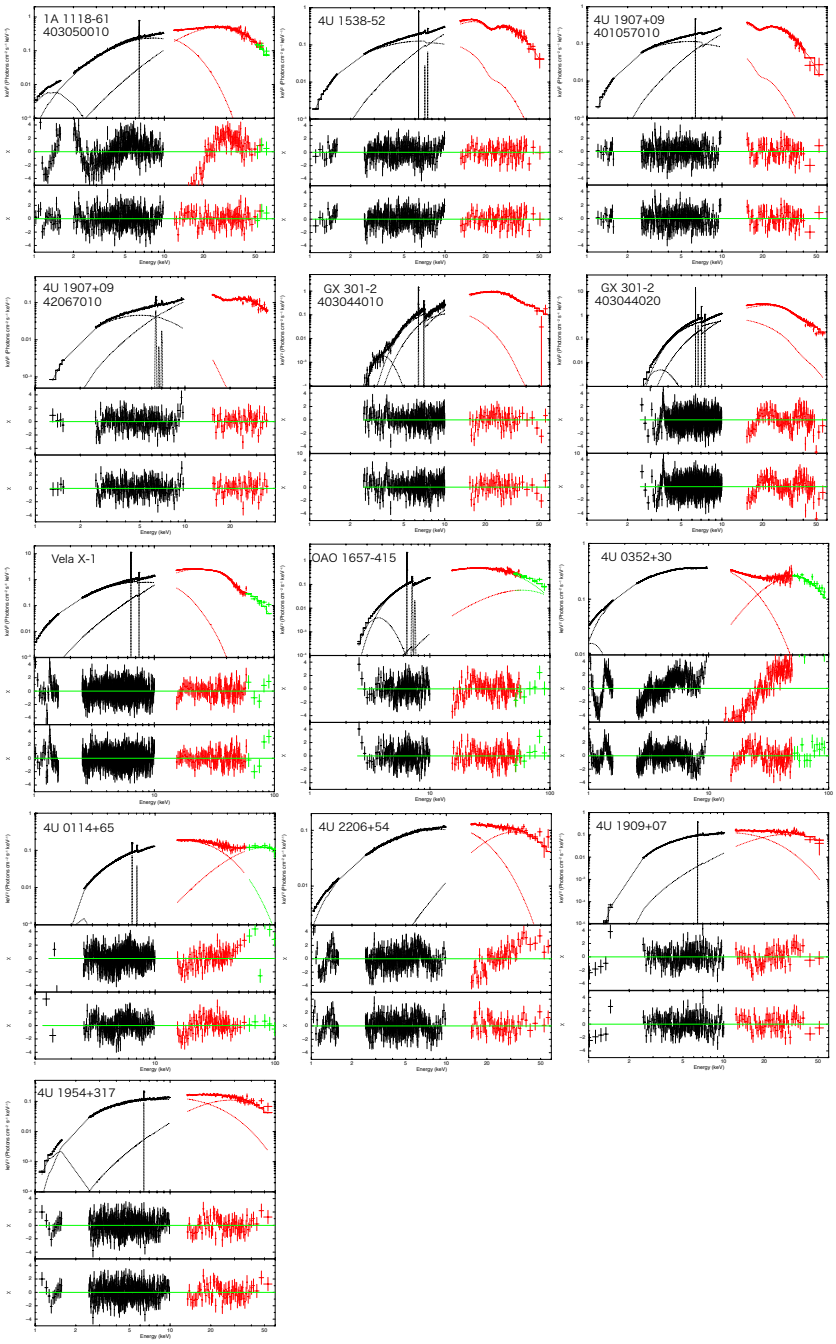

Figure 5.17: Continuous Figure 5.16

5.3.4 Behavior of NPEX parameters

The thirty spectra of the nineteen BXPs were thus fitted in a unified way, using the model, **phabs**×(**BB**+modified **NPEX**+3Gaussians)×**cyclabs**, which we arrived at in §5.3.3. Sometimes, the cyclabs factor or the **BB** component was not needed. (As described in §5.3.3, the modified **NPEX** model was sufficient except to the five spectra, A 0535+26, 1A 1118−61, 4U 0352+30, 4U2206+54 and 4U 0114+65.) The fit was mostly acceptable (typically χ^2_ν <1.15), and all the model parameters were determined with reasonable accuracies. Table 5.2 summarizes the best-fit spectral parameters of the sample BXPs with **NPEX** and the results with modified **NPEX** are shown in Table 5.3. Results on the iron lines are described in the next section, §5.4. Just for confirmation, Figure 5.18 compares kT of the **NPEX** fit with $kT_{\rm p}$ of the modified **NPEX** modeling. They are thus very close to each other, because both are determined by the highest end of the spectrum.

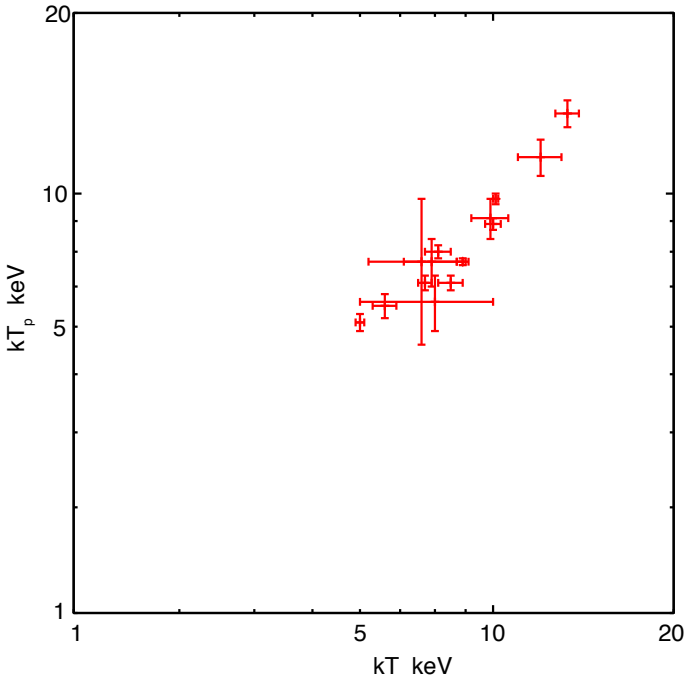

Figure 5.18: A correlation between kT of **NPEX** and modified **NPEX** $kT_{\rm p}$.

Let us recall that the modified **NPEX** model was needed to represent some spectra that have clear double-peaked spectra To quantify these features, let us utilize a schematic $\nu F\nu$ form of an **NPEX** model in Figure 5.19, and define two new characteristic energies, $E_{\rm np}$ and $E_{\rm pp}$, as the peak energies of the negative-index and Wien-hump components in $\nu F\nu$ spectra, respectively. From the model form of eq.5.4, they are readily expressed as

$$E_{\rm pp} = (2 + \Gamma_{\rm p}) \cdot kT = 4 \cdot kT \tag{5.6}$$

$$E_{\rm np} = (2 - \Gamma_{\rm n}) \cdot kT \tag{5.7}$$

where $\Gamma_{\rm p}$ equals to 2 because of Wien-hump for **NPEX**. For the modified **NPEX** model, those energies are written as

$$E_{\rm pp} = (2 + \Gamma_{\rm p}) \cdot kT_{\rm p} = 4 \cdot kT_{\rm p} \tag{5.8}$$

$$E_{\rm np} = (2 - \Gamma_{\rm n}) \cdot kT_{\rm n}. \tag{5.9}$$

As other parameters of the model, we consider the $\nu F\nu$ value, $N_{\rm pp}$ and $N_{\rm np}$, at $E_{\rm pp}$ and $E_{\rm np}$ respectively, as illustrated in Figure 5.19. They are written as

$$N_{\rm pp} = N_{\rm p} \cdot E_{\rm pp}^{2-\Gamma_{\rm p}} \cdot \exp[-(2 - \Gamma_{\rm p})] = e^{-4} \cdot N_{\rm p} \cdot (kT_{\rm p})^4 \tag{5.10}$$

$$N_{\rm np} = N_{\rm n} \cdot E_{\rm np}^{2-\Gamma_{\rm n}} \cdot \exp[-(2 - \Gamma_{\rm n})]. \tag{5.11}$$

Below, correlations among $E_{\rm pp}$, $E_{\rm np}$, $N_{\rm pp}$, and $N_{\rm np}$ are studied. However, they are not direct model parameters, but calculated by combining the direct model parameters, namely $kT_{\rm n}$, $kT_{\rm p}$, $\Gamma_{\rm n}$, $N_{\rm p}$, and $N_{\rm n}$. Therefore, errors to be assigned to these "indirect" parameters must be evaluated carefully. For this purpose, we extensively computed confidence contour plots among the direct parameters. Figure 5.20 and 5.21 shows the 4×3=12 confidence plots among the 4 parameters, for 4U 1538−52 and 4U 0352+30, respectively. There, 90%-confidence limits of the indirect parameters are indicated by dashed lines (e.g., $N_{\rm pp}$ on the $kT_{\rm p}$-$N_{\rm p}$ plane). Plots of the other sources are given in Appendix, while the determined error ranges of the indirect parameters are presented in Table 5.4 (for 11 low-L source on because they need particular caution).

Under these preparations, we consider the correlation between L and the cutoff energies. A plot of L vs. the ratio between $E_{\rm pp}$ and $E_{\rm np}$ is shown in Figure 5.22. As expected from the behavior of low-L objects the ratio is negatively correlated with L, approximately $E_{\rm pp}/E_{\rm np} \propto L^{-1/6}$. That is, as the luminosity decreases, the two **NPEX** components becomes more separated in a spectrum, ending up with the double-peak spectrum of the 5 low-luminosity source. To characterize the NPEX shapes, not only the cutoff energiess but also spectral height, $N_{\rm np}$ and $N_{\rm pp}$, is important. Figure 5.23(a) show a scatter plot of L vs. the ratio $N_{\rm pp}/N_{\rm np}$. Thus, the LPPs are indeed located on one extreme end of the plot. To farther discriminate them from the other low-L objects, Figure 5.23(b) plots all the 11 low-L ($<5\times10^{36}$ erg s^{-1}) objects, including the 5 LPPs, on the $E_{\rm pp}/E_{\rm p}$ vs. $N_{\rm pp}/N_{\rm np}$ plane. Thus, the lops are clearly separated, leading to a conclusion that their peculiar spectral shape is not due to their low luminosity.

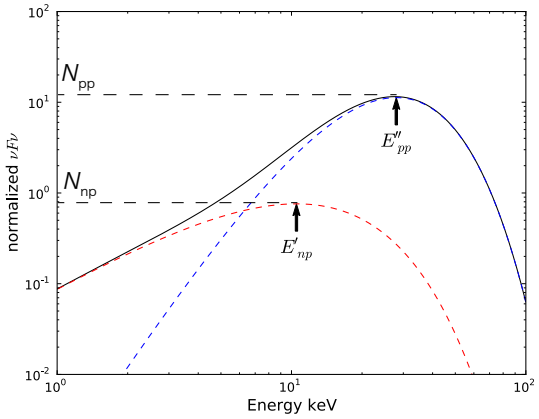

Figure 5.19: An $\nu F\nu$ presentation of a typical **NPEX** model. The dotted red and blue lines mean the negative and Wien-hump component, respectively. Their peak energies are defined as $E_{\rm pp}$ and $E_{\rm np}$, respectively, while the $\nu F\nu$ values at those energies are also defined as $N_{\rm pp}$ and $N_{\rm np}$.

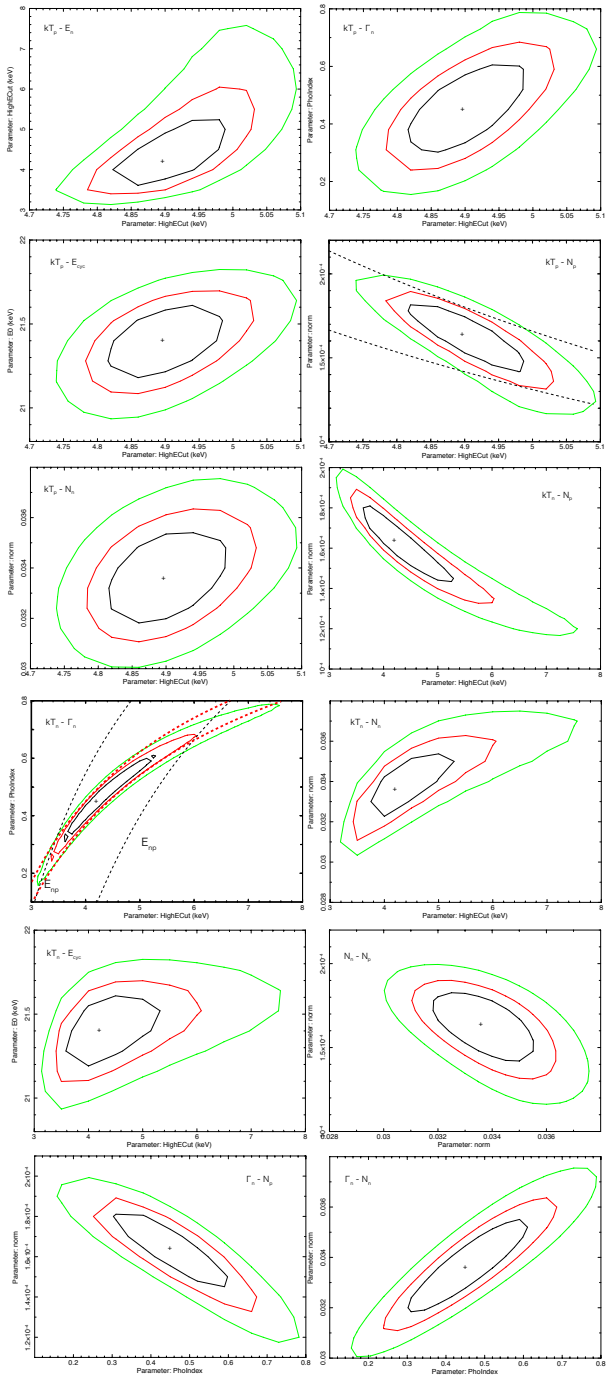

Figure 5.20: Confidence contour maps of χ^2 for various pairs among the modified **NPEX** model fitted to the 4U 1538−52 spectra. Black, red, free show ∼64%, 90%, and 99% confidence levels, respectively. The dashed lines on $kT_{\rm p}$ vs. $N_{\rm p}$ specifies the 90% confidence error ranges of $N_{\rm np}$. Those on $kT_{\rm n}$ vs. $\Gamma_{\rm n}$ are error range of $E_{\rm np}$ The red dashed lines on $kT_{\rm n}$ vs. $\Gamma_{\rm n}$ are nearly error range of $N_{\rm np}$

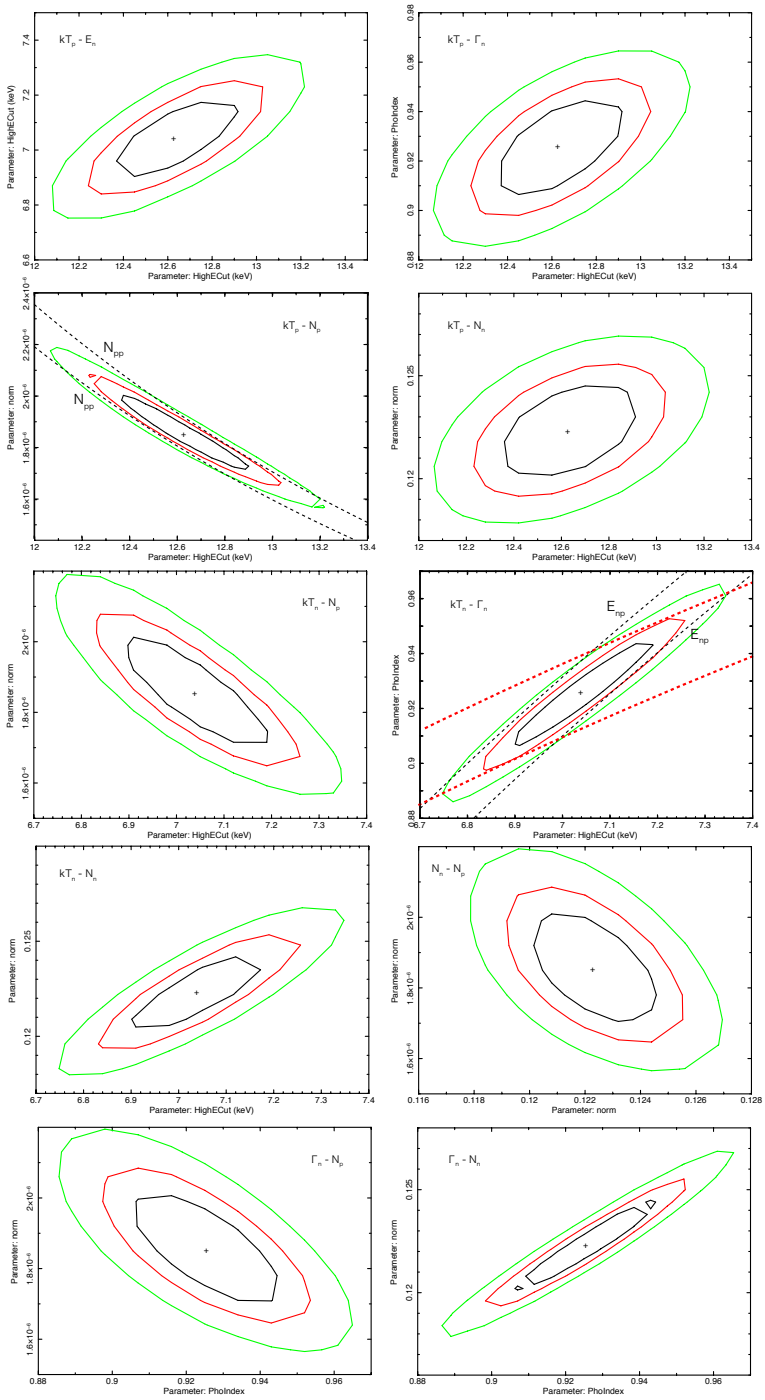

Figure 5.21: Same as Figure 5.20 but for spectra of 4U 0352+30.

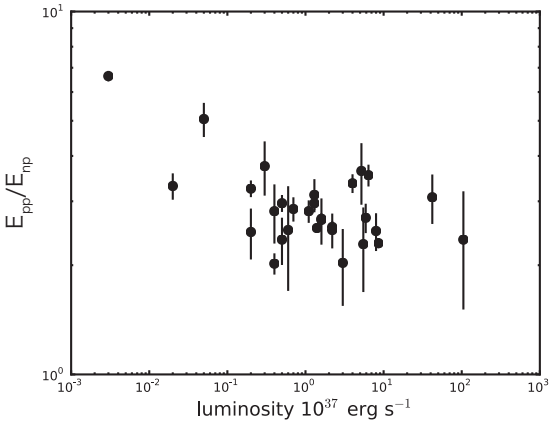

Figure 5.22: Correlation between L and the E_{pp}/E_{np} ratio

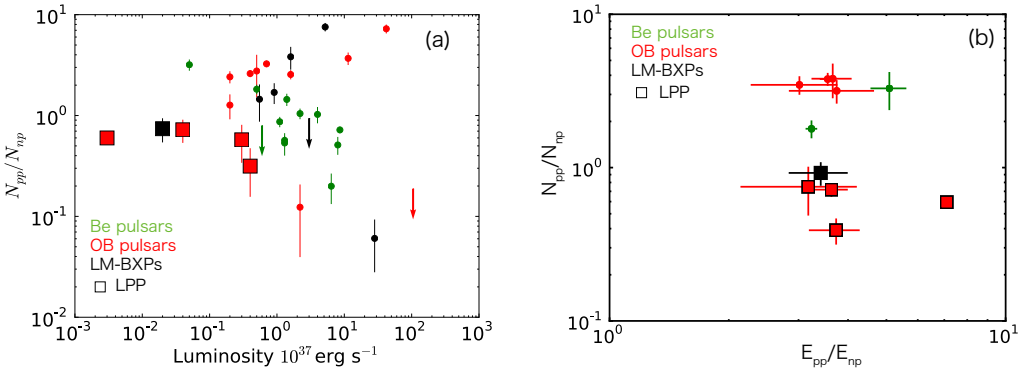

Figure 5.23: (a) A plot of the N_{pp}/N_{np} ratio against the luminosity of all our sample. (b) A scatter plot between the N_{pp}/N_{np} ratio and the E_{np}/E_{pp} ratio,for 11 objects with $L < 5 \times 10^{36}$ erg s^{-1}.

Table 5.2: Results of the **NPEX** model fitting

Object	ObsID	N_H $10^{22}cm^{-2}$	Γ_1/N_1 †	Γ_2/N_2 ‡	kT (keV)	E_{cyc},D,W (keV)	χ^2_ν (d.o.f)
SMC X-1	706030050	<0.04	2.0	0.30±0.10	8.0±2.0	—	1.17(353)
			<0.60	4.00±0.20			
Her X-1	405058030	<0.06	2.0	0.90±0.20	6.6±0.3	35.8±0.4	1.12(329)
			43.00±4.00	7.20±0.40		1.3±0.1	
						11±1	
	407051020	<0.06	2.0	0.38±0.02	6.9±0.3	36.6±0.3	1.39(560)
			40.00±5.00	10.0±0.40		1.4±0.1	
						11±1	
4U 1822−37	401051010	0.29±0.07	2.0	0.03±0.08	6.0±1.0	33.0±2.0	1.14(281)
			<5.0	1.80±0.10		$0.4^{+0.2}_{-0.1}$	
						$5.0^{5.0}_{-0.3}$	
Cen X-3	403046010	1.25±0.09	2.0	0.52±0.05	4.9±0.3	25.4±0.4	1.32(345)
			70.00±8.00	12.00±1.00		$1.0^{+0.2}_{-0.1}$	
						13^{+2}_{-1}	
LMC X-4	702036020	<0.04	2.0	0.70±0.20	6.0±0.1	—	1.13(241)
			6.10±0.40	1.30±0.10		—	
KS 1947+300	908001010	0.40±0.01	2.0	0.39±0.03	12.0±1.0	—	0.97(552)
			1.00±0.20	8.10±0.20		—	
EXO 2030+375	402068010	1.89±0.03	2.0	0.87±0.03	13.3±0.6	—	0.99(453)
			0.30±0.10	32.00±1.00		—	
	407089010	3.28±0.07	2.0	0.72±0.04	9.9±0.7	—	1.16(420)
			0.40±0.10	4.70±0.10		—	
4U1626-67	400015010	<0.02	2.0	0.25±0.05	7.6±1.4	36.0±1.0	1.23(359)
			1.00±0.40	0.67±0.02		$2.0^{+0.4}_{-0.3}$	
						$5.0^{+1.6}_{-1.2}$	
	405044010	<0.02	2.0	0.50±0.04	7.9±0.8	36.5±1.0	1.20(337)
			4.00±1.00	2.10±0.10		2.2±0.3	
						$6.1^{+1.4}_{-1.1}$	
GX 1+4	405077010	14.5±0.6	2.0	0.55±0.05	11.3±0.5	—	1.06(283)
			0.05±0.006	5.0±0.6		—	
GRO J1008−57	902003010	2.3±0.1	2.0	0.65±0.01	10.0±0.3	78.5 (fix)	1.50(446)
			1.00±0.10	9.50±0.20		0.9 (fix)	
						12 (fix)	
	907006010	0.95±0.02	2.0	0.26±0.01	8.9±0.2	78.5±2.0	1.42(470)
			14.00±1.00	27.70±0.40		0.9±0.2	
						12 (fix)	
XTE J1946+274	405041010	1.08±0.04	2.0	0.40±0.10	9.0±2.0	38.0±2.0	1.08(257)
			0.17±0.17	0.92±0.04		$1.3^{+0.5}_{-0.3}$	
						$7.0^{+4.0}_{-3.0}$	
OAO 1657−415	406011010	32±1	2.0	0.40±0.07	14.0±1.0	—	1.10(287)
			0.03±0.02	1.50±0.20		—	
Vela X-1	403045010	2.00±0.10	2.0	0.38±0.05	9.0±1.0	25.6±0.4	1.05(881)
			5.50±3.00	10.00±0.50		0.09±0.03	
						$5.5^{+2.5}_{-2.0}$	
A 0525+26	404054010	1.1±0.1	2.0	0.96±0.03	10.8±0.5	40.0±2.0	1.34(370)
			0.40±0.07	3.6±0.1		1.6±0.3	
						$15.0^{+5.0}_{-3.0}$	
A 0535+26	404055010	0.65±0.10	2.0	0.42±0.03	10.1±0.1	39.0±1.0	1.08(266)
			16.00±2.00	33.00±2.00		0.74±0.04	
						17±1	
4U 1907+09	401057010	2.2±0.2	2.0	0.81±0.06	4.5±0.1	18.6±0.2	1.15(304)
			17.00±1.00	5.60±0.30		0.58±0.04	
						2.5±0.4	

	402067010	2.53±0.07	2.0	0.65±0.06	4.7±0.1	18.6±0.5	1.02(228)
			6.30±0.80	1.90±0.10		0.49±0.07	
						3.0±1.0	
4U 1538−52	407068010	1.42±0.03	2.0	0.60±0.10	5.0±0.1	21.4±0.2	1.01(312)
			15.00±1.00	3.50±0.10		0.65±0.04	
						$3.2^{+0.6}_{-0.5}$	
1A 1118−61	403049010	1.17±0.06	2.0	0.02±0.02	8.5±0.4	50.0±1.0	1.28(410)
			11.00±2.00	7.10±0.20		1.0±0.1	
						15±2	
	403050010	2.5	2.0	0.3	8.2	50 (fix)	3.82(410)
			0.77	2.3		1.0 (fix)	
						15 (fix)	
GX 304−1	905002010	1.8±0.1	2.0	0.43±0.02	7.7±0.2	51.0±1.0	1.31(407)
			35.00±4.00	53.00±2.00		0.8±0.1	
						7.0±2.0	
	406060010	1.48±0.05	2.0	0.58±0.02	8.1±0.4	51.0±1.0	1.31(580)
			9.00±1.00	27.00±1.00		$7.0^{+1.5}_{-1.3}$	
						0.50±0.05	
GX 302−1	403044010	51±3	2.0	0.51±0.04	5.5±0.1	37.0±0.5	0.92(247)
			10.00±3.00	3.00±1.00		12.0 (fix)	
						0.7±0.2	
	403044020	31±1	2.0	0.30±0.20	6.2±0.4	37.0±2.0	1.08(555)
			59.00±5.00	16.00±1.00		12.0 (fix)	
						0.52±0.06	
4U 0114+65[LPP]	406017010	5.1±0.3	2.0	0.37±0.04	9.3±0.6	—	1.54(307)
			0.14±0.05	0.90±0.05		—	
4U 2206+54[LPP]	402069010	0.65	2.0	0.52	6.8	—	2.7(378)
			0.45	1.6		—	
4U 0352+30[LPP]	407088010	1.1	2.0	1.2	9.4	—	6.24 (397)
			0.3	16		—	
4U 1954+317[LPP]	407088010	3.1±0.1	2.0	0.15±0.01	7.1±0.4	—	1.13 (494)
			0.30±0.01	0.75±0.20		—	
4U 1909+07[LPP]	407088010		2.0	0.60±0.08	8.2±1.0	—	1.17 (227)
			0.2±0.1	1.6±0.1		—	

†: 10^{-5} photons cm^{-2} s^{-1} keV^{-1} at 1 keV.
‡: 10^{-2} photons cm^{-2} s^{-1} keV^{-1} at 1 keV.

Table 5.3: Same as Table 5.2 but with the modified NPEX model.

Object	ObsID	N_H 10^{22}cm^{-2}	Γ_p/N_p†	Γ_n/N_n‡	kT_p/kT_n (keV)	E_{cyc},D,W (keV)	χ^2_ν (d.o.f)
SMC X-1	706030050	< 0.04	2.0	0.25±0.1	6.6±0.7	—	1.06(352)
			<4.6	4.0±0.2	7.1±1.3	—	
Her X-1	405058030	<0.06	2.0	$0.87^{+0.06}_{-0.09}$	6.5±0.3	35.8±0.4	1.12(328)
			35±4.0	16±1.0	11.2±2.3	1.3±0.1	
						11±1	
	407051020	<0.06	2.0	-1.0±0.4	6.4±0.3	36.6±0.3	1.39(559)
			60±6.0	3.8±1.0	2.5±0.4	1.4±0.1	
						11±1	
4U 1822−37	401051010	0.29±0.07	2.0	0.03±0.08	6.0±1.0	33.0±2.0	1.14(280)
			<5.0	1.80±0.10		$0.4^{+0.2}_{-0.1}$	
						$5.0^{5.0}_{-0.3}$	

Cen X-3	403046010		2.0	0.52±0.05	4.9±0.3	25.4±0.4	1.32(344)
			70.00±8.00	12.00±1.00		$1.0^{+0.2}_{-0.1}$	
						13^{+2}_{-1}	
LMC X-4	702036020	<0.04	2.0	$0.83^{+0.14}_{-0.08}$	$4.9^{+0.2}_{-0.5}$	—	1.11(241)
			$4.5^{+0.8}_{-0.4}$	1.2±0.1	$7.1^{+3.0}_{-2.0}$	—	
KS 1947+300	908001010	0.41±0.02	2.0	0.45±0.1	11.5±0.8	—	0.97(551)
			0.9±0.4	8.2±1.0	12.0±2.0	—	
EXO 2030+375	402068010	1.9±0.1	2.0	0.85±0.04	13.6±0.7	—	0.97(452)
			0.27±0.10	32±1	13.0±0.6	—	
	407089010	3.0±0.2	2.0	0.55±0.1	$9.1^{+0.7}_{-0.5}$	—	1.16(419)
			0.7±0.25	4.1±0.4	$7.7^{+1.3}_{-1.0}$	—	
4U1626-67	400015010	<0.03	2.0	$0.28^{+0.14}_{-0.17}$	$7.7^{+2.1}_{-1.1}$	36.0±1.0	1.23(358)
			0.9±0.6	0.68±0.05	$8.2^{+3.3}_{-2.2}$	$2.0^{+0.4}_{-0.3}$	
						$5.0^{+1.6}_{-1.2}$	
	405044010	<0.02	2.0	$0.37^{+0.15}_{-0.13}$	7.7±0.7	36.4±0.5	1.20(336)
			$4.7^{+1.7}_{-1.0}$	1.9±0.3	6.3±1.8	2.2±0.3	
						$6.1^{+1.4}_{-1.1}$	
GX 1+4	405077010	14.5±0.6	2.0	0.55±0.05	11.3±0.5	—	1.06(282)
			0.05±0.006	5.0±0.6		—	
GRO J1008−57	902003010	1.5±0.1	2.0	0.21±0.07	11.0±2.0	78.5 (fix)	1.15(445)
			0.9±0.6	6.1±0.4	6.3±0.4	0.9 (fix)	
						12 (fix)	
	907006010	0.86±0.02	2.0	-0.22±0.07	8.9±0.2	78.5±2.0	1.42(469)
			24.0±4.0	18±1.0	5.2±0.3	0.9±0.2	
						12 (fix)	
XTE J1946+274	405041010	1.08±0.04	2.0	0.40±0.10	9.0±2.0	38.0±2.0	1.08(256)
			0.17±0.17	0.92±0.04		$1.3^{+0.5}_{-0.3}$	
						$7.0^{+4.0}_{-3.0}$	
OAO 1657−415	406011010	32±1	2.0	0.40±0.07	14.0±1.0	—	1.10(285)
			0.03±0.02	1.50±0.20		—	
Vela X-1	403045010	2.00±0.10	2.0	0.38±0.05	9.0±1.0	25.6±0.4	1.05(880)
			5.50±3.00	10.00±0.50		0.09±0.03	
						$5.5^{+2.5}_{-2.0}$	
A 0535+26	404054010	0.50±0.03	2.0	0.30±0.03	8.0±2.0	42±1	1.07(369)
			0.84±0.1	2.2±0.1	4.84±0.3	1.3±0.2	
						11^{+4}_{-3}	
A 0535+26	404055010	0.5±0.10	2.0	0.24±0.13	9.8±0.2	37.6±1.3	1.06(265)
			2.5±0.6	29±3.0	$7.6^{+1.6}_{-1.1}$	0.74±0.04	
						17±1	
4U 1907+09	401057010	1.8±0.2	2.0	0.28±0.2	4.4±0.1	18.6±0.2	1.15(303)
			21.5±2.5	4.4±0.3	$2.8^{+0.7}_{-0.4}$	0.58±0.04	
						2.5±0.4	
	402067010	2.53±0.07	2.0	0.65±0.06	4.7±0.1	18.6±0.5	1.02(227)
			6.30±0.80	1.90±0.10	2.6±0.6	0.49±0.07	
						3.0±1.0	
4U 1538−52	407068010	1.42±0.03	2.0	0.45±0.28	5.0±0.1	21.4±0.2	1.01(311)
			16±2.0	3.35±0.2	$4.2^{+1.8}_{-0.8}$	0.65±0.04	
						$3.2^{+0.6}_{-0.5}$	
1A 1118−61	403049010	0.78±0.04	2.0	-0.73±0.13	7.1±0.2	45.5±0.7	1.14(409)
			37.5±4.0	4.1±0.4	3.7±0.3	1.0±0.1	
						15±2	
1A 1118−61	403050010	0.9±0.1	2.0	-1.3±0.1	6.6±0.1	45.5 (fix)	1.15(409)
			5.3±0.3	0.66±0.06	2.5±0.1	<0.14	
						12 (fix)	
GX 304−1	905002010	1.3±0.1	2.0	0.0±0.1	8.0±0.2	49.0±0.8	1.19(406)
			62±10	36±4	4.9±0.5	0.8±0.1	
						7.0±2.0	

	406060010	1.48±0.05	2.0	0.26±0.07	7.1±0.2	51.0±1.0	1.29(579)
			12±2	25±1	6.7±0.6	$7.0^{+1.5}_{-1.3}$	
						0.50±0.05	
GX 302−1	403044010	51±3	2.0	-0.8±1.0	$6.0^{+0.6}_{-0.4}$	36.6±2.0	0.92(246)
			14±5	1.1±0.7	$2.8^{+2.8}_{-0.9}$	12.0 (fix)	
						0.7±0.2	
	403044020	31±1	2.0	$-0.57^{+0.3}_{-0.5}$	6.2±0.4	37.0±2.0	1.08(554)
			78±5	7.0±2.0	2.6±0.4	12.0 (fix)	
						0.52±0.06	
4U 0114+65	406017010	5.1±0.3	2.0	0.20±0.07	14±2	—	1.16(306)
			$0.05^{+0.04}_{-0.02}$	0.73±0.06	8.3±0.7	—	
4U 2206+54	402069010	0.8±0.1	2.0	0.33±0.09	8.0±0.5	—	1.27(378)
			0.4±0.1	1.5±0.1	5.2±0.5	—	
4U 0352+30	407088010	0.7±0.03	2.0	0.91±0.02	12.3±0.3	—	1.38 (395)
			0.20±0.02	12±1	6.8±0.1	—	
4U 1954+317	407088010	2.9±0.1	2.0	$0.51^{+0.18}_{-0.15}$	$6.4^{+0.4}_{-0.3}$	—	1.12 (493)
			2.6±0.02	1.5±0.4	$5.0^{+1.0}_{-0.7}$	—	
4U 1909+07	407088010	5.8±0.2	2.0	$0.14^{+0.21}_{-0.25}$	$7.7^{+1.4}_{-0.9}$	—	1.12 (226)
			$0.55^{+0.5}_{-0.3}$	1.1±0.2	$5.3^{+1.3}_{-1.0}$	—	

†: 10^{-5} photons cm^{-2} s^{-1} keV^{-1} at 1 keV.

‡: 10^{-2} photons cm^{-2} s^{-1} keV^{-1} at 1 keV.

Table 5.4: The values of $E_{\rm np}$, $E_{\rm pp}$, $N_{\rm np}$, and $N_{\rm pp}$ in 11 objects with L below 5×10^{36} erg s^{-1}.

Objects	$E_{\rm np}$ keV	$E_{\rm pp}$ keV	$N_{\rm np}$ keV^2 cm^{-2} s^{-1} keV^{-1}	$N_{\rm pp}$ keV^2 cm^{-2} s^{-1} keV^{-1}
4U 1538−52	$6.5^{+0.9}_{-0.7}$	19.6±4.0	0.127±0.01	0.44±0.05
4U 1907+09 (402067010)	$4.7^{+0.4}_{-0.2}$	17.6±4.0	0.12±0.02	0.38±0.02
4U 1907+09 (401057010)	4.7±0.5	17.2±0.8	0.05±0.01	0.19±0.03
Vela X-1	8.3±0.3	29.5±0.8	0.90±0.07	3.4±0.2
A 0535+26 (404054010)	8.1±0.3	$41.2^{+4.0}_{-3.2}$	0.14±0.02	0.46±0.11
1A 1118−61 (403050010)	8.1±0.2	26.2±0.6	0.24±0.03	0.43±0.02
4U 0352+30$^{\rm LPP}$	7.1±0.1	50.4±1.6	0.37±0.02	0.22±0.01
4U 0114+65$^{\rm LPP}$	15.0±0.5	56±8	0.41±0.03	0.16±0.03
4U 2206+54$^{\rm LPP}$	$8.7^{+0.4}_{-0.3}$	31.6±2.8	0.11±0.01	0.079±0.004
4U 1954+317$^{\rm LPP}$	7.5±0.5	25.6±4.0	0.13±0.02	0.12±0.01
4U 1909+07$^{\rm LPP}$	$9.7^{+1.4}_{-0.7}$	$30.8^{+9.0}_{-5.0}$	0.12±0.04	0.09±0.01

5.4 Fe Lines

As shown in Figures 5.9 and 5.10, Fe lines appear at $\sim$ 6.4 keV in most of the spectra. By studying the lines, we are able to know distributions of matters surrounding the NSs and estimate the distance between the X-ray source and the illuminated matter. In some cases, not only the neutral iron line but also ionized lines were detected at somewhat higher energies.

5.4.1 Neutral Fe-Kα lines

To study the spectral continua in §5.3, we fitted wide band spectra with the **NPEX** model. In this section, we focus on the Fe lines and fit the spectra over a narrow range between 5 and 8 keV with **phabs**×**cutoffPL** and Gaussians, for the continuum and the lines, respectively. The column densities were fixed to the values obtain in §5.3.4 (Table 5.2 and 5.3) and all parameters of the **cutoffPL** are left free. In most of the sample spectra, two Gaussians were employed to explain Fe-Kα ($\sim$6.4 keV) and Kβ ($\sim$7.05 keV) lines. When Ni-Kα line appears at $\sim$7.5 keV, it was fitted by another Gaussian (Figure 5.12). Three parameters of the Gaussians, the center energy $E_{\rm N}$, the line width σ, and normalization $I_{\rm N}$ left free. The value of $I_{\rm N}$ ($\propto$ area) directly gives the line photon flux, in units of photons s^{-1} cm^{-2}, after correcting for the instrumental responses (i.e., the effective area, the quantum efficiency, and other factors). The obtained results on the neutral Fe-Kα lines are shown in Table 5.5.

When the fluorescence lines are emitted, we generally expect

$$I_{\rm N} = a \cdot g \cdot N_{\rm H} \cdot f_{7.1} \cdot \Delta E, \tag{5.12}$$

where $f_{7.1}$ is the continuum flux (ph cm^{-2} s^{-1} keV^{-1}) just above 7.1 keV, ΔE is an effective energy interval (somewhat depending on the continuum slope), which contribute to the fluorescence, g is a form factor of matter distribution defined to be unity for an isotropic and uniform case, $N_{\rm H}$ is a representative column density of the matter, and a is a constant of proportionality depending neither on the matter distribution on the continuum shape. Equation 5.12 may be rewritten as

$$g \cdot N_{\rm H} = \frac{1}{a \cdot \Delta E} \frac{I_{\rm N}}{f_{7.1}} = \frac{1}{a \cdot \Delta E} \frac{f_{6.4}}{f_{7.1}} \cdot W_{\rm eq} \tag{5.13}$$

where $W_{\rm eq} \equiv I_{\rm N}/f_{6.4}$, with $f_{6.4}$ the continuum flux at 6.4 keV, is a quantity called equivalent width (EW), and It has a dimension of energy. Since ΔE and $f_{6.4}/f_{7.1}$ depend only weakly on the continuum slope, we approximately expect

$$W_{\rm eq} \propto g \cdot N_{\rm H}. \tag{5.14}$$

To examine eq. 5.14, Figure 5.24 shows the EWs of the Fe fluorescence line against the

line-of-sight $N_{\rm H}$ determined in §5.3.4 (Table 5.2 and 5.3). Indeed, the EW is approximately proportional to $N_{\rm H}$ above $N_{\rm H} \sim 1{\times}10^{23}$ cm^{-2}, and is consistent with a prediction by assumption with isotropic and uniform distribution (Inoue 1985) indicated in Figure 5.24 by a dotted line. However, below $\sim 1{\times}10^{23}$ cm^{-2}, only a few objects (mostly, LPPs) keep the proportionality, and the EWs of the remaining majority of BXPs exhibit significant excess above the theoretical prediction, becoming nearly constant at several tens eV independent of $N_{\rm H}$. This reconfirms previous works (Inoue 1984; Makishima 1986), and implies that g increases as $N_{\rm H}$ falls below $\lesssim 1{\times}10^{23}$ cm^{-2}. In other words, the matter distribution is not isotropic in such a cases, and some thick materials and interred to be present in a certain direction that is out of our line-of-sight. Interestingly, and importantly, none of the 5 LPPs in our sample exhibits such and EW excess; they follow the simulation.

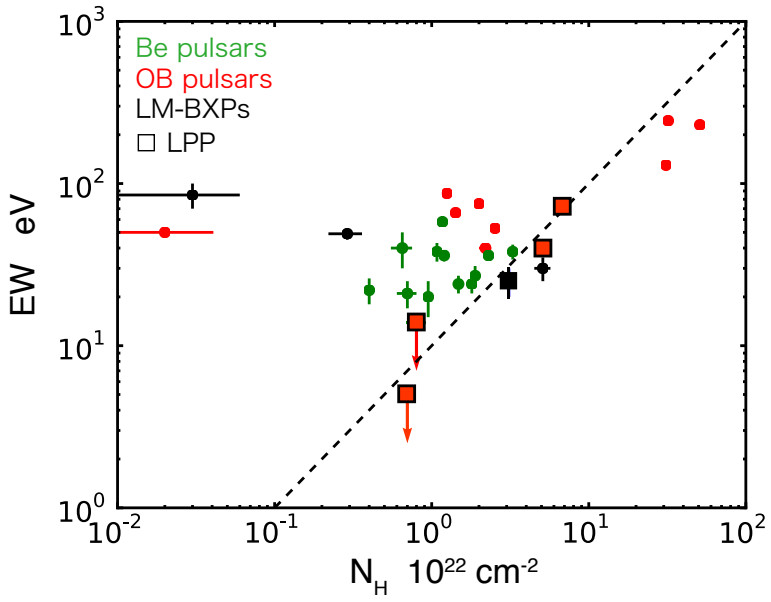

Figure 5.24: A plot of $N_{\rm H}$ vs EW of the Fe-K line. The dotted curve indicates a prediction for an isotropic and uniform matter distribution (Inoue 1985). Green points are Be pulsars, red OB pulsars, and black are LM-BXPs. The square marks are LPP objects.

5.4.2 Photoionized iron lines

In addition to the ubiquitous presence of the neutral Fe-K line, ionized iron lines have been detected in a past studies from some objects (§2.3.1), including Cen X-3, a luminous source, in particular. This is also the case with our sample (Figure 5.9 and 5.10, §5.3.1). Figure 5.25, shows the spectra of 7 particular sources in our sample that exhibit such ionized Fe-K lines. These are Cen X-3, GRO J1744−28, GRO J1008−57, KS 1947+300, EXO 2030+375, Her X-1, and GX304−1. In a large outburst (§4.3.2), GRO J1744−28 exhibited very complicated ionized line complex. For comparison, the figure also presents another source that does not

show clear ionized lines.

To evaluate the ionized lines quantitatively, we fitted all the spectra with a continuum component and Gaussians in the same way as in §5.4., but considering the ionized lines as well. If clear ionized lines are present in the spectra, the center energies of the Gaussians were left free while they were otherwise fixed to 6.7 keV and 6.93 keV for helium-like and hydrogen-like lines, respectively. The Gaussian width σ was constrained to be common among the three lines. The obtained fit results are summarized in Table 5.5, together with those for the neutral Fe-K lines. Overall, 6 objects (the 5 sources mentioned above plus 4U 1822−37) exhibited the 3 lines, while other nine sources showed He-like lines; two of them, Her X-1 and GX 304−1, are indicated in Figure 5.25. Thus, we were able to determine the intensity (or upper limit) of the He-like Fe-Kα line $I_{\rm He}$, and those of the H-like one, $I_{\rm H}$.

The presence of the ionized lines is strongly correlated with the source luminosity. In fact, the 6 objects with the three lines have an average luminosity of $\sim 5\times10^{37}$ erg s^{-1} erg s^{-1}, the 9 sources with the neutral and He-like lines have $\sim 5\times10^{36}$ erg s^{-1}, while the others are distributed at $<5\times10^{36}$ erg s^{-1}. Thus, the iron ionization is inferred to proceed as L increases. Then, how can we more quantitatively evaluate the measured $I_{\rm He}$ and $I_{\rm H}$?

As described in §2.3.1, so-called ionization parameter ξ is usually employed to evaluate the degree of ionization. The data cannot constrain ξ when it is rather small, $\log(\xi) < 2$, because the Fe-K line center energy is not very sensitive to ionization from neutral to Fe^{+15}. However, ξ becomes better constrained for $\log(\xi) > 3$, because He-like and H-like lines start to appear. For the simplicity, we define

$$\xi' = (I_{\rm He} + I_{\rm H})/I_{\rm N} \tag{5.15}$$

as an index of the degree of ionization, and use it instead of ξ. (This is because the presence of the 3 Fe-K lines cannot be expressed by a single value of ξ.) Considering the definition of ξ (eq.2.20), we expect that ξ' is also determined by the same three parameters, namely, L, the matter density n, and the distance r between the matter and the NS. Considering the definition of $\xi \equiv L/n \cdot r^2$, we expect ξ' to correlate positively with L, and negatively with $n \cdot r^2$. Since $n \cdot r^2$ is difficult to estimate, it may be replaced by the EW (summed over the ionization states) which is approximately determined by n times the depth of matter distribution. We hence studied whether ξ' is positively correlated with the L/EW ratio, and obtained the results shown in Figure 5.26. For objects, GRO J1008−57, EXO 2030+375, 1A 1118−61, and GX 304−1, were observed multiple times, at different L. Arrows In Figure 5.26 specify such change among the observations in a single. In whole, ξ' clearly exhibits a positive correlation against L/EW, and each object also follows the same correlation as it varied. Thus, a clear positive correlation seen in Figure 5.26 provides clear evidence for the progress of photoionization towards objects with higher luminosities and lower ambient-matter densities. (For reference, the correlation between ξ' and L is considerable worse than that between ξ' vs L/EW.) In this plot, the 5 LPPs

(all with upper limits on ξ') are located at lower-left of the correlation, and can be regarded as BXPs with the weakest signature of photoionization.

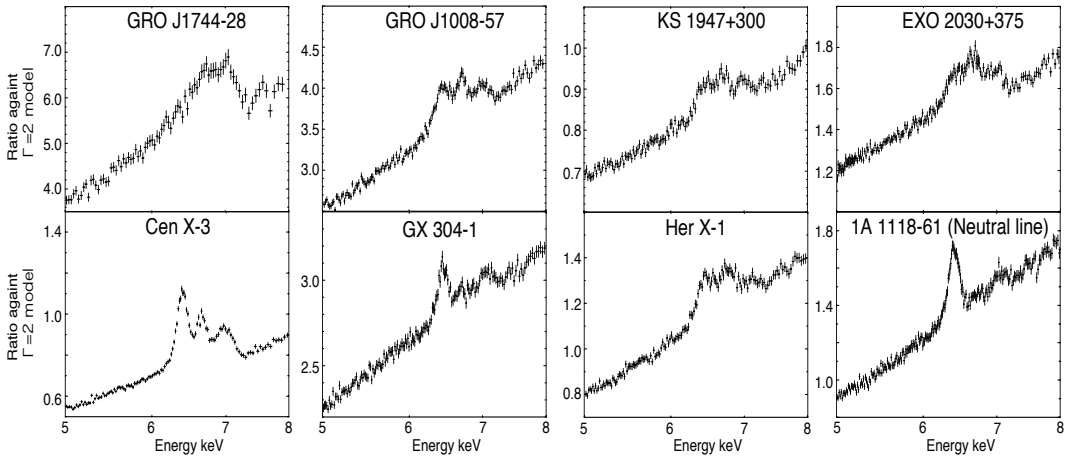

Figure 5.25: Expanded view of the spectra around the iron lines, observed from 8 BXPs in the sample.

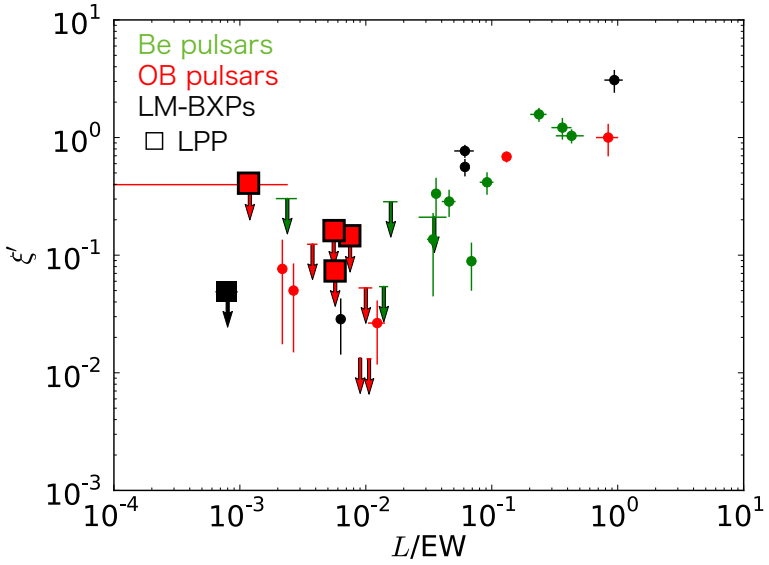

Figure 5.26: Dependences of ξ' on L/EW. The colors and mark are same as in Figure 5.24.

Table 5.5: The results of iron line parameters.

Object	ObsID	EW eV	E_N/I_N‡ keV	E_{He}/I_{He}‡ keV	E_H/I_H‡ keV	σ eV
Her X-1	405058030	37^{+5}_{-8}	6.44±0.01 12.5±0.7	6.75±0.02 5.6±0.7	— —	70±10
4U 1822−37	401051010	49^{+3}_{-4}	6.39±0.01 3.2±0.2	6.68±0.04 0.08±0.02	6.97±0.04 0.10±0.02	40±20
Cen X-3	403046010	87±5	6.39±0.01 16±0.05	6.65±0.01 8.0±0.5	6.96±0.01 1.4±0.5	27^{+6}_{-8}
LMC -4	702037010	47±5	6.35±0.02 1.6±0.3	6.65±0.04 1.1±0.3	6.95±0.09 0.5±0.3	70±30
KS 1947+300	908001010	22±4	6.42±0.02 4.2±0.6	6.68±0.02 3.7±0.6	6.97±0.03 1.4±0.5	<50
EXO 2030+375	402068010	23±3	6.39±0.01 8.9±0.9	6.65±0.01 10±1	6.97±0.03 4.0±0.8	70±10
	407089010	34±2	6.43±0.01 2.2±0.2	6.7 (fix) 0.3±0.2	—- —-	40^{+20}_{-30}
GRO J1008−57	902003010	20±5	6.38±0.01 2.7±0.4	$6.62^{+0.04}_{-0.07}$ 0.9±0.3	—- —-	<40
	907006010	36±2	6.42±0.01 2.9±0.2	6.69±0.01 2.2±0.3	6.98±0.02 8.0±2.0	40±20
XTE J1946+274	40504101	38±5	6.43±0.02 8.5±15	6.7 (fix) <2.4	— —	<100
OAO 1657−415	406011010	244±4	6.44±0.01 0.7±0.1	6.7 (fix) <0.035	— —	<10
Vela X-1	403045010	75±3	6.39±0.01 20±1	6.65±0.05 0.4±0.2	— —	<20
4U 1907+09	401057010	40±5	6.40±0.01 1.9±0.1	6.7 (fix) <0.1	— —	<10
	402067010	53±5	6.39±0.01 1.3±0.2	6.7 (fix) <0.16	— —	<50
4U 1538−52	407068010	66±3	6.40±0.01 3.2±0.2	6.7 (fix) <0.04	— —	<20
1A 1118−61	403049010	58±2	6.40±0.01 18±0.7	6.70±0.03 1.6±0.7	— —	30±20
	403050010	36±3	6.40±0.01 2.6±0.3	6.7 (fix) <0.15	— —	<40
GX 304−1	905002010	20±5	6.40±0.01 36±3	6.69±0.03 15±3	— —	<40
	406060010	24±3	6.39±0.01 14±1	6.70±0.04 5.6±0.7	— —	<40
GX 302−1	403044010	230±20	6.40±0.01 17±1	6.7 (fix) 1.3±1.0	— —	<20
	403044020	130±10	6.39±0.01 34±1	6.7 (fix) 0.9±0.5	— —	<20
A 0535+26	404054010	21±4	6.38±0.02 0.07±0.02	6.7 (fix) <0.023	— —	<20
	404054020	40±10	6.39±0.01 3.2±0.9	6.7 (fix) <0.66	— —	<20
XTE J1946+274	405041010	38±5	6.40±0.01 0.085±0.015	6.7 (fix) < 0.024	— —	<20
4U 0114+65	406017010	40±4	6.39±0.01 0.07±0.01	6.7 (fix) < 0.01	— —	<20
4U 0352+30	407088010	<5.0	6.39±0.01 0.042±0.018	6.7 (fix) < 0.017	— —	20 (fix)
4U 2206+54	402069010	<14.0	6.39±0.01 0.015±0.01	6.7 (fix) < 0.01	— —	20 (fix)
4U 1909+07	405073010	72±3	6.39±0.01 0.19±0.02	6.7 (fix) < 0.031	— —	<20

‡: 10^{-3} photons cm^{-2} s^{-1}

Chapter 6

DISCUSSION

In Chapter 5, we studied 25 BXPs observed with *Suzaku*, in terms of their luminosity, pulse properties, continuum shape of X-ray spectra, and Fe lines. Here, we summarize the obtained results and investigate several aspects of the physics of BXPs.

6.1 Properties of Long Period Pulsars

One of the goals of the present thesis is to examine whether LPPs (Long-Period Pulsars, BXPs those with $P_{\rm s} > 600$ s and no CRSF; §4.2.2) are different from the others, and if so, what is their nature. The present BXP sample includes 5 LPPs, which form a considerable fraction of this subsample, although several (e.g., AX J1631.9 $-$ 4752, RX J0146.9+6121) are missing. As revealed in Chapter 5, the LPPs are different from the other BXPs from the following five aspects.

1. As shown in Figure 5.2, they are much less luminous than the others. Assuming the torque equilibrium, the long $P_{\rm s}$ of LPPs may be attributed, via eq. 2.31, to their low values of L, or alternatively, to stronger B ($\sim 10^{15}$ G).

2. In terms of the pulse profile and the PF (pulse fraction; §5.2.2), LPPs are possibly different. While LPPs have as large PFs as that of the others, their PFs depend (at least in some cases) on the energy than those of BXPs from two methods, as shown in Figure 5.8.

3. From two LPPs in our sample, HXD-GSO detected significant signals, and allowed us to calculate their HXD-GSO vs HXD-PIN hardness ratios (§5.3.2). In the generally positive correlation between $P_{\rm s}$ and hardness ratio in Figure 5.11(b), the two LPPs are located at the highest-hardness end. This suggests that their spectra are extremely hard and possibly different.

From the quantitative evaluations with the **NPEX** or modified **NPEX** model, the spectra of LPPs have been reconfirmed to differ from those of the others. In their $\nu F\nu$ spectra, especially of 4U 0352+30 and 4U 0114+65, two peaks clearly appear at ~20 and 80 keV. In addition, LPPs are located on an extreme end of the L-$N_{\rm pp}/N_{\rm np}$ diagram (Figure 5.23a), and are spectated by other low L sources on the $E_{\rm pp}/E_{\rm np}$ vs.$N_{\rm pp}/N_{\rm np}$ plane (Figure 5.23b).

4. Iron line features of LPPs are also different. In Figure 5.24, all LPPs lies on the predicted EW $\propto N_{\rm H}$ proportionality line, while the other BXPs deviated from the line at low $N_{\rm H}$. From the results, the matter is considered to distribute spherically around LPPs, while more anisotropically around the other BXPs.

6.2 Correlations with Magnetic Filed Strengths

In §6.1, we have confirmed that LPPs differ in various aspects from the other BXPs, and that their low L is unlikely to be the origin of the difference. Then, from item1 of §6.1, another possibility is that they have stronger B. In this section, let us examine this hypothesis. In our sample, 13 BXPs show CRSFs in their spectra and their magnetic field strength have been measured. However, for the other sources including the 5 LPPs, it is difficult to measure B directly because of their lack of CRSF detection. Therefore, we here examine how the properties of our CRSF objects depend on their B, and use the obtained dependence to indirectly estimate the field strengths of the remaining objects including the LPPs.

First, we consider the two basic parameters, $P_{\rm s}$ and L. As described in §2.3.3, B should be proportional to $P_{\rm s} \cdot L^{3/7}$ if the torque equilibrium holds. Accordingly, we plot in Figure 6.1 the values of $P_{\rm s} \cdot L^{3/7}$ of our CRSF pulsars, as a function of their B as determined using the CRSF energy. Since our CRSF sample is incomplete, four more objects with the CRSF detetions were added (see caption of Figure 6.1). Thus, the values of $P_{\rm s} \cdot L^{3/7}$ largely deviate from the prediction from eq. 2.31, $P_{\rm s} \cdot L^{3/7} \propto B^{6/7}$, so that the assumption of the equilibrium may not be correct. Nevertheless, the 5 LPPs have significantly larger values of $P_{\rm s} \cdot L^{3/7}$ (blue arrows), and their distribution agrees with what would be exhibited by those BXPs which have $E_{\rm cycl}$ in the range 10^{2-3} keV, or B=10^{13-14} G from eq. 2.31. Thus, the LPPs are suggested to have rather strong B.

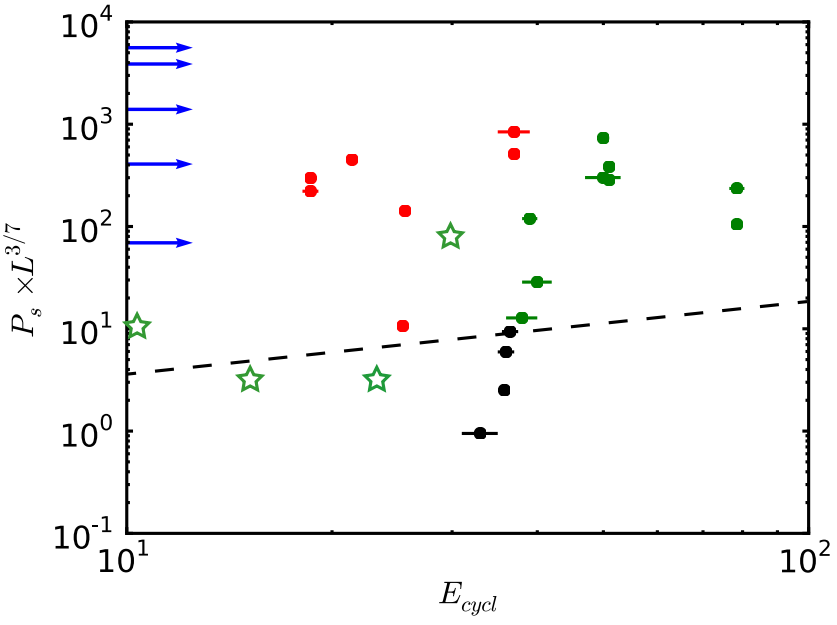

Figure 6.1: A scatter plot of $E_{\rm cycle}$ vs. $P_{\rm s} \times L_{37}^{3/7}$ for nearly complete CRSF pulsars. The colors are same as Figure 5.24. The stars mean results taken from literature (Mihara et al. 1991 for Cep X-4; Nakajima et al. 2010 for X0331+53; Nakajima et al. 2006 for 4U 0115+63). The blue arrows show $P_{\rm s} \times L^{3/7}$ values of the 5 LPPs, and the dashed line is the prediction by eq. 2.31.

In Figure 6.2(a), a good correlation was confirmed between $E_{\rm cycl}$ and $E_{\rm pp}$, as already re-

ported by Makishima et al. (1999). In addition, the $N_{\rm pp}/N_{\rm np}$ ratio also correlates with $E_{\rm cycl}$ as shown in Figure 6.2(b). From these two correlations, BXPs with stronger magnetic fields are inferred to have higher cutoff energy and weak Wien-hump components, so that $E_{\rm pp}$ and $N_{\rm pp}/N_{\rm np}$ approximately scale as

$$E_{\rm pp} \sim (4.8 \pm 0.8) \times E_{\rm cycl}^{1/2} \tag{6.1}$$

$$\frac{N_{\rm pp}}{N_{\rm np}} \sim 30 \times E_{\rm cycl}^{-1}, \tag{6.2}$$

respectively. Some objects (Vela X-1, XTE J1946+274, and A 0535+26) deviated from the eq. 6.1 while most of sample are close to the line represented by eq. 6.1. As one possibility, we consider $E_{\rm cyc}$ depend on not only $E_{\rm pp}$ but also other parameters. When we consider L as the parameter, similar luminous sources will deviate from the dotted line in Figure 6.2. Considering 4U 1538-52 and 4U 1907+09, which is similar to Vela X-1, they locate near the line so that $E_{\rm cyc}$ does not depend on L strongly. Until now, we can not find another parameter which have relation to $E_{\rm cyc}$ excluding $N_{\rm pp}/N_{\rm np}$. In Figure 6.2(a), the 5 LPPs are represented by horizontal blue stripes, as their $E_{\rm cyc}$ is not known. Although three of them shown similar values of $E_{\rm pp}$ as the others, the remaining the (4U 0352+30 and 4U 0114+65) are much deviated, and eq. 6.1 implies $E_{\rm cyc}$ = 80 - 300 keV for them. This translates, via eq. 2.22,

$$B = (8 - 30) \times 10^{12} G. \tag{6.3}$$

Similarly, in Figure 6.2(b), 4U 0352+30 and 4U 0114+65 show rather low $N_{\rm pp}/N_{\rm np}$ ratios, which give via eq. 6.2 $E_{\rm cyc}$ = 100 keV. This leads to

$$B = (3 - 10) \times 10^{12} G. \tag{6.4}$$

Thus, the scalings of eq. 6.1 and eq. 6.2 consistently (but may not be independent because of dependence among $E_{\rm pp}$, $N_{\rm pp}$, and $N_{\rm np}$) suggest the 5 LPPs to have $B \sim 10^{13}$ G, which is higher than those of typical BXPs. Although we derived eq. 6.1 empirically, let us consider physical meaning of the equation. In accretion column near a NS surface, photon pressure, which is proportional to temperature T^4 is much stronger than gas pressure and the pressure equals to magnetic field pressure B^2 (Basko & Sunyaev 1976). In the state, $B^2 \propto T^4$ is achieved and this is the same as eq. 6.1 because $E_{\rm pp}$, $E_{\rm cyc}$ is almost same as T and B. Thus, eq. 6.1 is supported physically.

In §6.1, LPPs have been shown to be clearly different from the other BXPs in many empirical aspects, including timing and spectral properties. In §6.2, we utilized the CRSF pulsars to calibrate how various properties of BXPs depend on B. It was then found that several parameters of the LPPs ($P_{\rm s} \cdot L^{3/7}$, $E_{\rm pp}$, and $N_{\rm pp}/N_{\rm np}$) can be reproduced if the corresponding parameters

of ordinary (B=1-7×10^{12} G) are scaled towards higher values of B, typically $B \sim 10^{13}$ G or higher. Combining these two sets of results, we conclude that LPPs generally have stronger magnetic fields ($B \sim 10^{13}$ G), and this particular property is responsible for their difference among the whole BXP population.

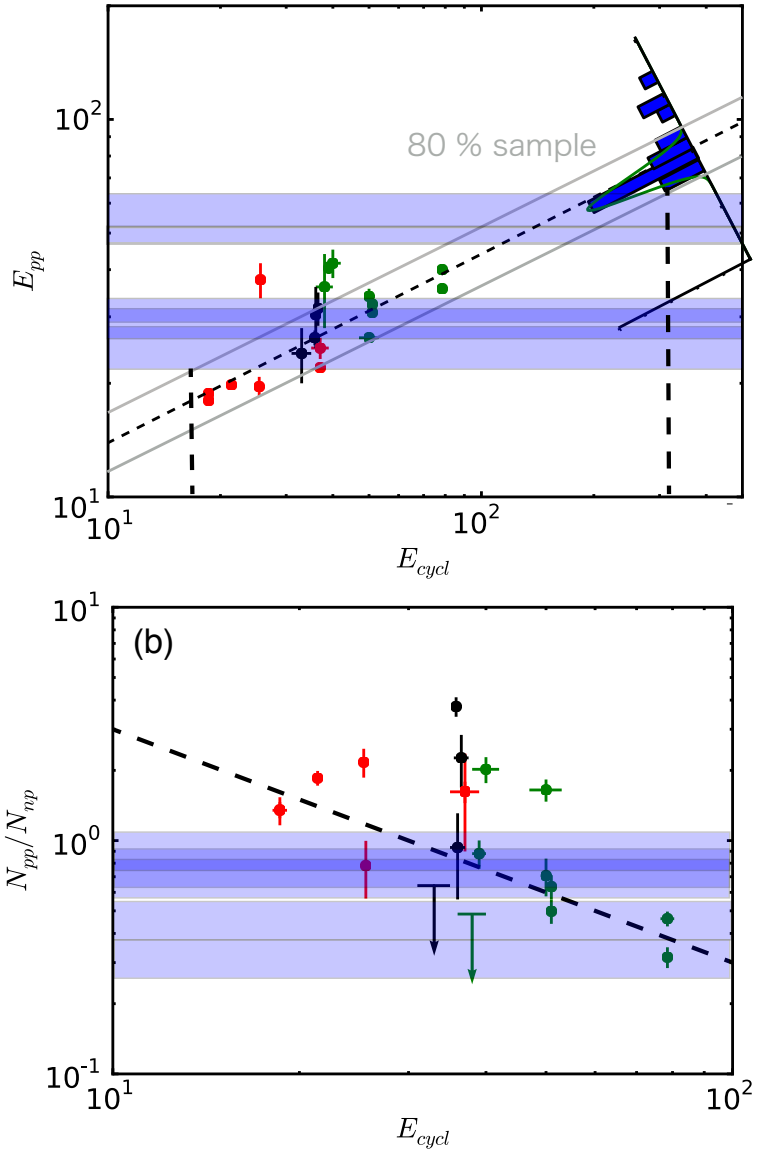

Figure 6.2: (a) A correlation between $E_{\rm cycl}$ and $E_{\rm pp}$ for the CRSF pulsars in our sample. Blue areas mean possible location of LPPs. (b) That between $E_{\rm cyc}$ and $N_{\rm pp}/N_{\rm np}$. In both panels, the five LPPs are indicated by blue stripes.

6.3 Other Properties of BXPs

In §6.1 and 6.2, we mainly focused our discussion on the correlations with B. Here, we examine some other parameters.

6.3.1 Continuum components with BXPs spectra

As described in Figure 6.2, $E_{\rm pp}$ and $N_{\rm pp}/N_{\rm np}$ are both correlated with $E_{\rm cycl}$. Of those two **NPEX** parameters, the cutoff energy $E_{\rm pp}$ is considered to represent the temperature in the accretion column, while the normalization ratio $N_{\rm pp}/N_{\rm np}$ are possibly related to the Compton optical depth τ (Makishima et al. 1999, Odaka et al. 2014). Expecting that $E_{\rm pp}$ and $N_{\rm pp}/N_{\rm np}$ should correlate with each other, we produced their scatter plot in Figure 6.3. As expected, the two quantities show a good correlation, which is described with an exponential function (the dashed line) as

$$N_{\rm p}/N_{\rm n} = 0.081 \exp\left(-\frac{E_{\rm pp}}{6.0}\right) \ . \tag{6.5}$$

On the other hand, Odaka et al. (2014) used a Monte-Carlo simulation to "calibrate" the physical meanings of the **NPEX** model, and derived a dependence as

$$N_{\rm p}/N_{\rm n} \propto \exp(\tau) \ . \tag{6.6}$$

Combining eq. 6.5 and eq. 6.6, we obtain a linear relation as

$$\tau = A - B \cdot E_{\rm pp} \tag{6.7}$$

where A and B are positive constants. Below, we consider physical meanings of eq. 6.7.

The Compton optical depth τ of the accretion column is expressed as

$$\tau = n_{\rm e} \cdot \sigma_{\rm T} \cdot R_0 \tag{6.8}$$

where $n_{\rm e}$, $\sigma_{\rm T}$, and R_0 are the electron number density, the Thomson cross section, and a typical size of the accretion column, respectively. Equation 6.7 means that the spectral cutoff $E_{\rm pp}$ somehow depends on $n_{\rm e}$ and R_0. Of the two, the dependence of $n_{\rm e}$ is easier to explain: an increased $\dot{M}$, without changes in R_0, would increase $n_{\rm e}$ and hence τ, but also enhance the radiative cooling in the accretion column, thus bringing $E_{\rm pp}$ to lower energies.

It is more difficult to consider how $E_{\rm pp}$ depends on R_0, and how R_0 itself it determined. Since R_0 will increase if the accreting matter can fall along larger number of magnetic field lines, it may be controlled by the matter distribution at the Alfven radius $r_{\rm A}$ defined in eq. 2.29. With this in mind, we made a scatter plot, Figure 6.4(a), between $E_{\rm pp}$ and the $r_{\rm A}/r_{\rm co}$ ratio.

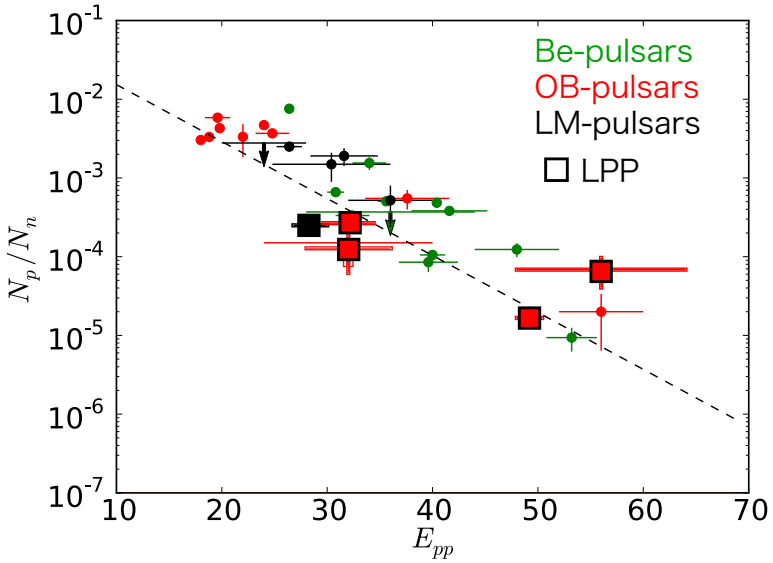

Figure 6.3: A plot of $N_{\rm p}/N_{\rm n}$ against $E_{\rm pp}$. The dashed line is the best-fit exponential function of eq. 6.5. Green points are Be pulsars, red OB pulsars, and LM pulsars. The square points means LPPs.

Surprisingly, a relatively tight correlation has appeared, with an $E_{\rm pp}$ peak at $r_{\rm A}/r_{\rm co} = 0.2 - 0.4$. One possible interpretation is as follows. If the matter is far away from co-rotation with the magnetosphere ($r_{\rm A}/r_{\rm co} \gg 1$ or $r_{\rm A}/r_{\rm co} \ll 1$) when it is caught by the field lines, the matter, rotating rapidly as seen from the magnetosphere, will find the easiest descending points (e.g., polar openings), to make R_0 smaller (thinner column). The consequent decrease in R_0 will be overwhelmed in eq. 6.8 by the associated increase in $n_{\rm e}$, leading to an increase in τ and decrease in $E_{\rm pp}$ due to cooling. If, in contrast, the matter is nearly in co-rotation with the magnetosphere, it will be forced to start descending to the NS from all azimuth angles along many different field lines. This will make the column thicker, and cause the opposite changes as the above case.

Assuming the above interpretation is correct, an interesting consequence is that the torque equilibrium condition is realized at $r_{\rm A}/r_{\rm co}$=0.1-0.4, rather than at ~1 as predicted by eq. 2.31. To further examine this, we produced in Figure 6.5 a histogram of the $r_{\rm A}/r_{\rm co}$ ratio of our sample BXPs. Interestingly, LM-BXPs, which are likely to be disk-fed, have the ratio ~1 or somewhat larger, in agreement with the theoretical prediction. In contrast, OB-pulsars (except the very luminous Cen X-3) which must be wind-fed have smaller ratios. Be-pulsars are distributed in between.

One possible interpretation of Figure 6.5 is that these OB-pulsars are actually all in the spin-up regime, because matter penetrating inside $r_{\rm co}$ would be rotating faster and faster than the NS as they fall, until they are finally guided to the magnetic poles at $r_{\rm A}$. This would cause the NS to spin up rapidly. However, these OB pulsars are known to exhibit both spin-up and spin-down behavior, with a typical spin-up/spin-down time scale of a few kyr which is much shorter than their typical age(100 kyr). Therefore, we must conclude that they are actually in

a torque equilibrium, and the small r_A/r_{co} ratio is due to their wind accretion dynamics. One possibility is that the accreting matter in this case has a considerably lower angular velocity thant the Keplerian rotation. Then the matter will be still rotating slower than the NS at the nominal r_{co}, and will become co-rotational at a considerably smaller radius Therefore, if we define a modified Alfven ratio as

$$r'_A \sim 5 \times r_A \ , \tag{6.9}$$

the magnetic vs. gravitational pressure balance may be expressed better as $r'_A \sim r_{co}$, rather than the conventional idea of $r_A \sim r_{co}$. If we use r'_A instead of r_A, the torque equilibrium condition, eq. 2.32, becomes

$$B = 4.9 \times 10^{-3} \times P_s^{7/6} L_{37}^{1/2} \times 10^{12} \ \text{G}. \tag{6.10}$$

If this modification is employes to source which $r_A/r_{co} < 0.3$, as presented in Figure 6.4(b), the magnetic field strength calculated from the torque equilibrium assumption comes into much better agreement with B measured with the CRSF and are consistent of the measured B within factor 10. This solve an issue raised in §2.3.3, that a straightforward application of eq. 2.31 would give unrealistically high values of $B = 10^{13-14}$ G for OB pulsars. This justifies the use of the modified Alfven radius.

This modification of r_A to r'_A has an important implication for LPPs. In Figure 6.4, the relatively high spectral cutoffs of the 5 LPPs suggest that these wind-fed objects are also in a co-rotation condition. Then, the modified estimate, eq. 2.32, gives $B \sim 10^{13-14}$ G (rather than the unrealistic previous estimate of $\sim 10^{15}$ G mentioned in §6.1.1).This strengthens our argument presented in §6.2.

6.3.2 Where Fe lines emitted

So far, we have been arguing that LPPs generally have $B \sim 10^{13}$ G. Here, we may invert the line of logic, and examine wheather this "strong B" assumption can explain, in a top-down manner, all the observed properties of LPPs.

In Figure 5.26, ionization of Fe lines ξ' is positively correlated to L/EW. In the correlation, we did not consider the distance r between the matter and the NS. To study location of the matter, r is very important information.

As candidates of the location, we consider two parameters, r_{co} and r'_A. As described in §2.3.1, and 5.4.2, ionization parameter are presented as eq. 2.20. From analogy of the parameter, ξ' is written as

$$\xi' = \frac{L}{\text{EW} \cdot r^2} \tag{6.11}$$

so that ξ' is able to be evaluated with observable quantities. We substitute the candidates in 6.11 and show a scatter plot of ξ' against $L/(\text{EW} \cdot r'^2_A)$ in Figure 6.6. The correlation between ξ'

and $L/(\mathrm{EW}\cdot r_{\mathrm{co}}^2)$ is not good. On the other and, the Figure exhibits proportionality therefore the Fe lines are emitted from alfven shell.

The idea of Fe-K line production at the Alfven shell (though not new; see Nagase 1989) can explain one important observational fact, that the Fe-K line flux (not EW) of an BXP is rather constant across its pulse phase (e.g., Odaka et al. 2013), even though the continuum has a high PF. In fact, the matter on the Alfven shell is considered to be approximately co-rotating with the NS in many BXPs (§6.3.3). Then, the continuum beam will be illuminating the same locations on the Alfven shell, thus producing a constant Fe-K line flux. This can reconcile the matter anisotropy implied by Figure 5.19 with the required pulse-phase independence of the Fe-K line flux.

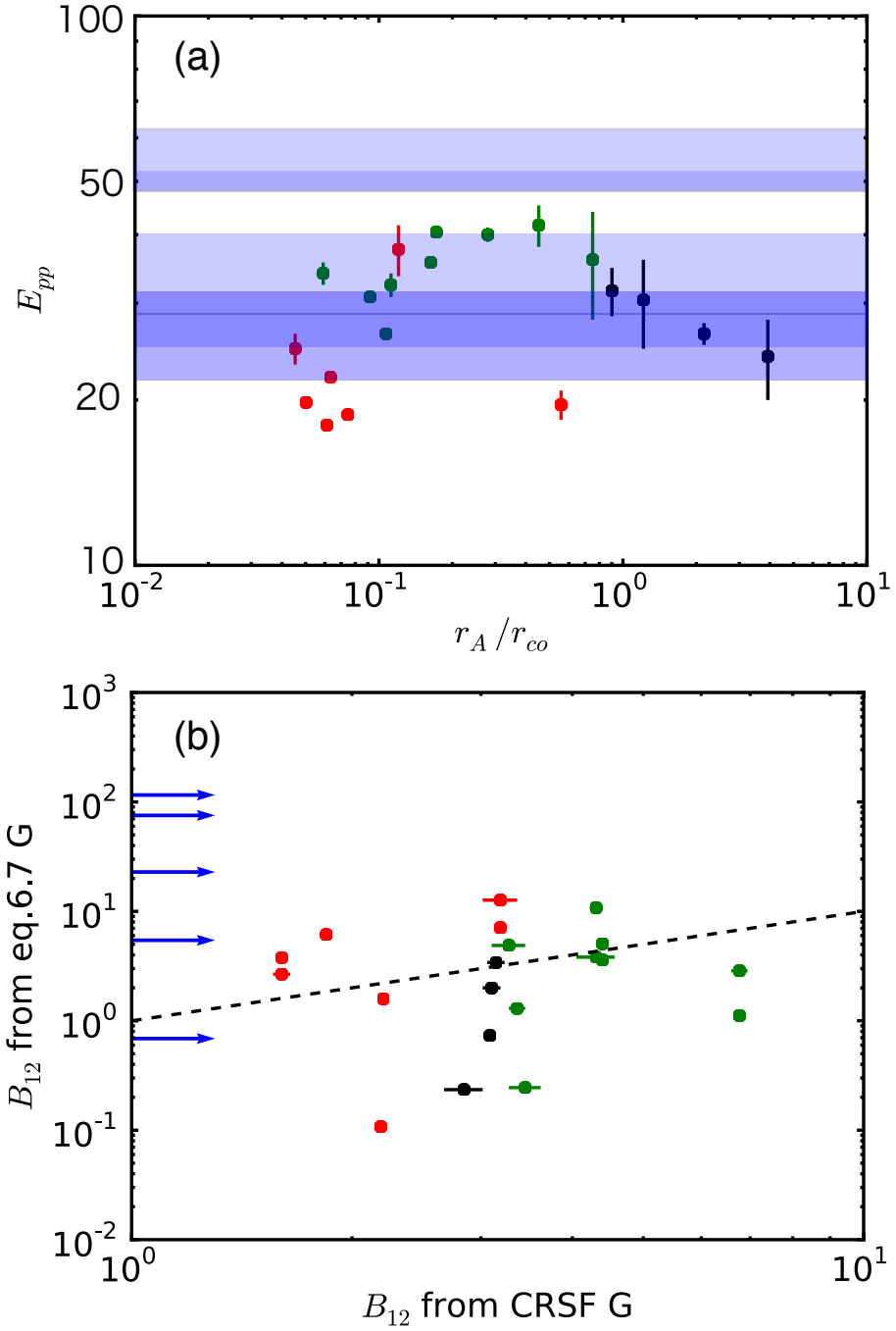

Figure 6.4: (a) A scatter plot of r_A/r_{co} vs. E_p. (b) A correlation between observed B and estimated B form eq. 2.32. dashed line means the observed B equals to the estimated B. The colors are the same as Figure 5.24.

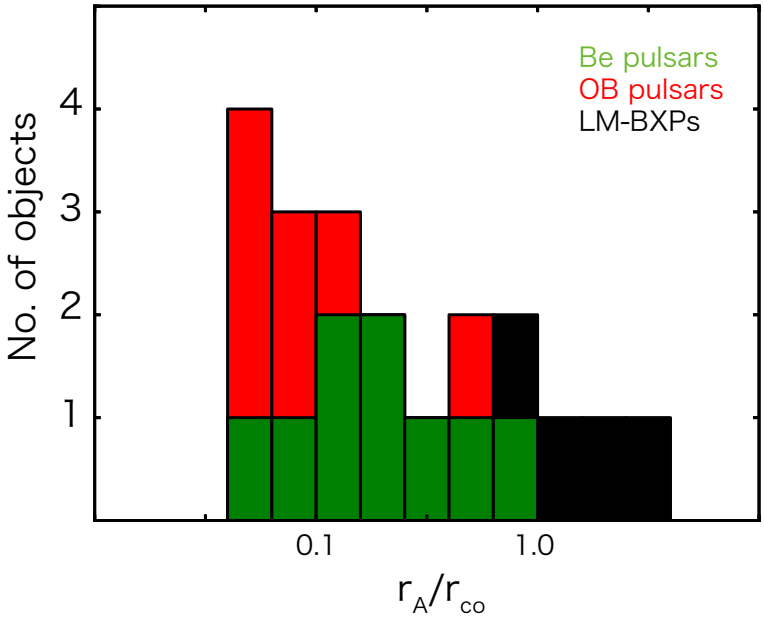

Figure 6.5: A histogram of the ratio between r_A and r_{co} of our sample BXPs

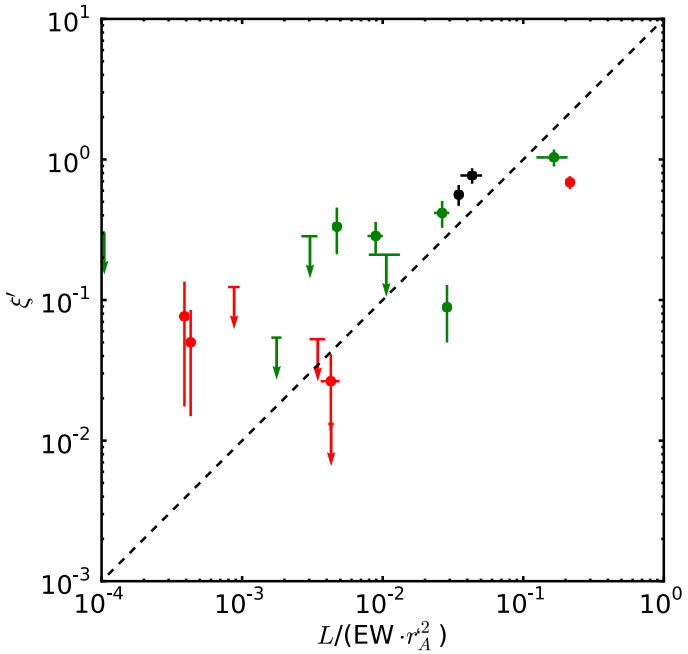

Figure 6.6: A scatter plot of $L/(\mathrm{EW}\cdot r_A'^2)$ vs. ξ'. The colors are the same as Figure 5.24.

6.4 Possible Scenarios of LPPs

6.4.1 Comparison among three radii

The process of stellar-wind accretion onto X-ray pulsars involve three characteristic radii. First of them is the co-rotation radii $r_{\rm co}$, already discussed extensively. In the case of LPPs, $P_{\rm s}$ are very long so that eq. 2.30 becomes

$$r_{\rm co} = 1.7 \times 10^{10} \times P_{\rm s,1000}^{2/3} \ \ {\rm cm} \tag{6.12}$$

where $P_{\rm s,1000}$ is the value of $P_{\rm s}$ in a unit of 1000 s. Typical LPPs have $P_{\rm s}$=1000-10000, which gives $r_{\rm co} \sim 10^{10-11}$ cm. The second is their modified Alfven radii defined in eq. 6.9. Because of the low L and the suggested high B, LPPs are expected to have

$$r'_{\rm A} = 1.2 \times 10^{10} \times L_{36}^{-2/7} \cdot B_{13}^{4/7} \ \ {\rm cm} \tag{6.13}$$

where L_{36} and B_{13} are the same as L_{37} and B_{12} but in a unit of 10^{36} erg s^{-1} and 10^{13} G, respectively. Comparing with typical BXPs, LPPs are thus considered to have one order of magnitude large $r'_{\rm A}$, which is indeed comparable to $r_{\rm ro}$. for BXPs. Then, we need to consider a third radius, namely, the Bondi radius of eq. 2.10, which is given as

$$r_{\rm B} = 3.7 \times 10^{10} \times v_{\rm w,1000}^{-2} \ \ {\rm cm} \tag{6.14}$$

where $v_{\rm w,1000}$ is the wind velocity units of 1000 km s^{-1}. Because $r'_{\rm A} \sim r_{\rm co}$ in LPPs, their accreting dynamics may depend on whether $r_{\rm B}$ is larger than the other two radii or not.

Among the three radii, $r_{\rm B}$ depends only on the property of the primary star, $v_{\rm w}$, of which distributions should be small because most of the primary stars in BXPs are high-mass ones with types of O or B. Thus, $r_{\rm B}$ should also have small dispersion among the BXPs in our sample, and hence can be used to normalize the other two parameters. Here and hereafter, we assume $v_{\rm w}$=1000 km s^{-1}. We show the correlation between $r_{\rm A}/r_{\rm B}$ and $r_{\rm co}/r_{\rm B}$ in Figure 6.7. Assuming $B = 10^{13-14}$ G, together with $L = 10^{35-36}$ erg s^{-1}, eq. 6.13 and eq. 6.14 predict them to have

$$r'_{\rm A}/r_{\rm B} = 0.3{-}2.5. \tag{6.15}$$

Therefore, LPPs are likely to fill in the vertical blue region indicated in Figure 6.7. On the other hand, the 5 LPPs, with their values of $P_{\rm s}$, also have

$$r_{\rm co}/r_{\rm B} = 0.3{-}3 \tag{6.16}$$

as shown by horizontal blue arrows. These considerations suggest strongly that the 5 LPPs

are likely to be located on the cross point of the three dashed lines on Figure 6.7, as long as $B \sim 10^{13}$ G is a correct estimate. We hence infer that LPPs are generally characterized by

$$r'_{\rm A} \sim r_{\rm B} \sim r_{\rm co}, \tag{6.17}$$

while $r_{\rm co}$ and $r'_{\rm A}$ of the typical BXPs are both smaller than $r_{\rm B}$.

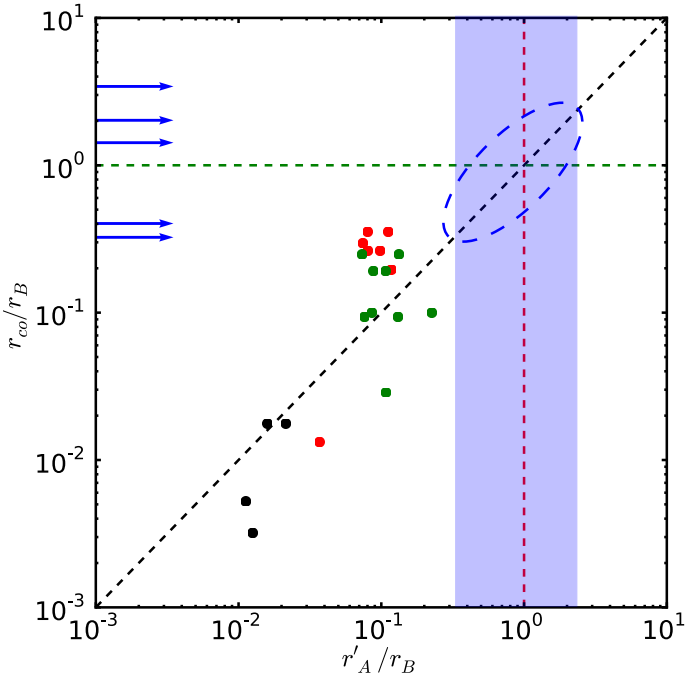

Figure 6.7: Correlation between the ratios $r'_{\rm A}/r_{\rm B}$ and $r_{\rm co}/r_{\rm B}$. The black dotted line means $r'_{\rm A}$ equals to $r_{\rm co}$, the green $r_{\rm co} = r_{\rm B}$, and the red $r'_{\rm A} = r_{\rm B}$. Vertical blue stripe shows the range of eq.6.15, while blue arrows indicate the 5 LPPs. The red, green, and black dots show the CRSF pulsars in the present sample, in the same color specification as Figure 5.24.

6.4.2 Explanations of LPP properties in terms of strong B

With a help of Figure 6.7, let us examine whether the strong B assumption can explain the known properties of LPPs in the following 5 aspects.

1. From eq. 2.31, the NS should have intrinsically long $P_{\rm s}$. Considering eq. 6.9, eq. 2.31 is rewritten as

$$P'_{\rm eq} = 33.6 \times L_{37}^{-3/7} \cdot \mu_{30}^{6/7} \ \ {\rm s}. \tag{6.18}$$

   Substituting $L_{37} = 0.1$ and $\mu_{30} = 100$ yields $P'_{\rm s}$~6500 s, which reproduces the observed spin periods of LPPs very well.

2. As shown in Figure 6.7, $r'_{\rm A}$ of strong B objects becomes comparable to $r_{\rm B}$. When $r_{\rm A} \gtrsim r_{\rm B}$, the magnetic field interrupts the wind capture, to reduce $\dot{M}$, because the NS can capture

the stellar wind only in a region outside $r'_{\rm A}$ but inside $r_{\rm B}$. Therefore, we can explain why LPPs are intrinsically low-luminosity objects (Figure 5.2).

3. No clear CRSF have been observed in the spectra of LPPs up to 100 keV. Since CRSF should appear above 100 keV when $B \geq 10^{13}$ G, the strong-B hypothesis is consistent with the absence of CRSF in the *Suzaku* spectra of LPPs. In addition, the very hard and flat spectra of LPPs, with high cutoff energies, can be explained empirically via eq.6.1 as a result of high values of B. This scaling may be explained, at least qualitatively (Mihara 1995), that the strong electron cooling via cyclotron resonance (including higher harmonics) will prevent their temperature to increase beyond $\sim E_{\rm cycl}$. As a result, LPPs have high cutoff energies and their spectra extend over 100 keV.

4. As shown in Figure 5.6 and 5.7, the PF spectra of the CRSF pulsars increase steeply near $E_{\rm cycl}$. By assuming that LPPshave $E_{\rm cycl}$ >100 keV ($B \gtrsim 10^{13}$ G), we can explain the fact described in §6.1.1, that the PF of LPPs depends more weakly on the energy than those of the other BXPs.

5. When $r'_{\rm A}$ is comparable to $r_{\rm B}$, the accreting matters will not be able to form a disk and should distribute rather spherically. This picture can explain the fact revealed in Figure 5.24, that the values of Fe-K EW are proportional to $N_{\rm H}$ in LPPs while those of the other BXPs are constant below $\sim 3\times10^{22}$ cm^{-2}.

As shown above, we have successfully explained the essential properties of LPPs in a top-down way, starting from a simple and single assumption that they have relatively strong magnetic fields of the order of 10^{13} G or higher.

6.5 Distribution of Magnetic Field Strengths

As described in §2.1.1, the distribution of B of NSs in Figure 1.1 exhibits three distinct peaks, at $\sim 10^8$, $\sim 10^{12}$, and $\sim 10^{15}$ G. The final step of the present thesis is an attempt to understand the origin of this distribution.

6.5.1 Selection effects

From Figure 1.1, it is clear that no BXPs above 10^{13} G are known. This reflect the fact that CRSFs have so far been detected all in energies below 100 keV. However, we should consider two selection effects and correct the distribution for the effects.

First, as shown in §6.4.1, X-ray pulsars with $B \sim 10^{13}$ G are intrinsically less luminous than the other BXPs, and are hence difficult to detect in principle. Therefore, the detection of strong-B pulsars should be limited to our closer vicinity than the ordinary ($B \sim 10^{12}$ G) objects. More quantitatively, assuming that luminosities of strong-B objects are 1/30 of those of the other BXPs (Figure 5.2) and those objects distribute in our Galactic disk uniformly, and if the latter can be detected to 20 kpc, then the former can be detected to only $20/\sqrt{30} \sim 3.6$ kpc; the former is therefore expected to be ∼30 times larger in number. In fact, the five LPPs in our sample are located at 1-4 kpc while the others are at 3-10 kpc.

Secondly, it is difficult to detect CRSFs at high energies with which we measure B, even though we knew candidates of $B \sim 10^{13}$ G X-ray pulsars. This is because the flux of the sources decrease, and detector sensitivities decrease, both towards higher energies. More quantitatively, let us compare ease of detection at 40 keV and 100 keV. When we approximate a BXP spectrum by single cutoff power-law $E^{-0.5}\exp[-E/(10\mathrm{keV})]$, photon number density at 100 keV is ∼1/1000 of that at 40 keV. In addition, the detection limit of the *Suzaku* HXD at 100 keV is 1.6 times as high as that at 40 keV as shown in Figure 3.10. Combining these effects, detection of a source at ∼100 keV would require a ∼1600 times higher source intensity (assuming the same spectrum) than its detected at 40 keV. In fact, the highest-energy CRSF, the $\sim$ 80 keV feature of GRO J1008−57 previously suggested by Shrader et al. (1999), was clearly confirmed by *Suzaku* in a bright outburst reaching 1 Crab (Yamamoto et al. 2014), but was not confirmed in a previous *Suzaku* observation made in 2007 in a smaller outburst up to $\sim$ 90 mCrab (Naik et al. 2011b). We therefore expect that a considerable number of high-B objects actually lurk among the currently known BXPs. Obvious candidate include LPPs (the 5 objects in our sample and a few more), GX 1+4 and EXO 2030+375 with their extremely hard spectra.

As discussed so far, we presume that the actual magnetic-field distribution of binary NSs is significantly more extend to the $B > 10^{13}$ G region, than is represented by Figure 1.1

6.5.2 Relation between LPPs and other BXPs

In §6.5.1, we argued that the B-distribution of BXPs, if corrected for the selection effects, is likely to extend towards higher values beyond $\sim 10^{13}$ G. Then, the next question is whether LPPs, which are thought to carry the distribution at $B > 10^{13}$ G (§6.2, §6.4), are genetically different from the other BXPs or not. On one hand, our discussion in §6.1.1 indicates that LPPs are different in several aspects from the other BXPs with $B \sim 10^{12}$ G. A particularly impressive different is seen in Figure 2.14, where few objects are found in the range $P_{\rm s}$=2000-5000 s. On the other hand, LPPs as a population show no particular differences from BXPs with massive companions. For example, these two subclasses have very similar values of $P_{\rm orb}$ (Figure 2.3), and they commonly have massive primaries of spectral type of O or B. Therefore, LPPs and the other BXPs (with massive companions) are likely to have been born in similar conditions, without a large intrinsic gap in their magnetic-field strength. Thus, we need to reconcile the tow conflicting requirements, namely, the apparent difference between LPPs from the other BXPs and their similar birth conditions

One possible scenario is to assume that LPPs were born simply at the highest end of the continuous B-distribution, but were separated over times from the rest, to form an apparently distinct subclass. We can consider the following two evolutionary branches,

1. B is strong so as to make $r'_{\rm A} > r_{\rm B}$.

   If a BXP is born by chance under this condition, the strong magnetic field would push away the stellar winds beyond the Bondi radius within which the NS's gravity can capture the winds (§6.2). Therefore, the object would remain in a low-luminosity condition. Ignoring the decay of B, the relation between $r'_{\rm A}$ and $r_{\rm B}$ will not change with time. Although the NS can initially be rotating rapidly, the implied large $r_{\rm co}$ will allow an efficient transfer of the angular momentum from the NS to the stellar winds.

2. B is not so strong, and $r'_{\rm A} < r_{\rm B}$

   If born under this condition, the NS can efficiently capture the stellar winds in regions between $r'_{\rm A}$ and $r_{\rm B}$, to become a luminous X-ray source. Once the accretion started, $r'_{\rm A}$ would shrink due to the accretion pressure, and hence the difference between $r'_{\rm A}$ and $r_{\rm B}$ would be enhanced. This will in tern accelerate the wind capture, thus causing positive feedback. Meanwhile, the angular momentum transfer between the NS and the captured (accreting) matter will bring $r'_{\rm A}$ and $r_{\rm co}$ close together, as seen in Figure 6.7

As argued above, X-ray pulsars boron with $r'_{\rm A} > r_{\rm B}$ will remain low-luminosity source with slow spin, namely LPPs, while those which initially had $r'_{\rm A} < r_{\rm B}$ are expected to become more and more luminous and acquire relatively fast rotations (i.e., ordinary BXPs). This picture can explain how a rather continuous distribution in B can generate the distinction between LPPs and the others.

6.5.3 Relations to magnetars

From our results obtained so far, LPPs is likely to be located between typical BXPs and magnetars in terms of B strength. Here, we compare LPPs with magnetars, and study relations between them.

In table 6.1, properties of LPPs and magnetars are summarized. The largest difference between them is their system, accretion-driven binaries vs. magnetically powered isolated objects: magnetars have never been discovered in binaries. Some magnetars are associated with SNR, and their age, are tightly constrained by the age of the SNRs ($\lesssim$ 10 kyr). The characteristic ages of magnetars can be somewhat larger, but much shorter than the typical age of LPPs constrained by the lifetime of their companion stars.

Another important of comparison is the magnetic field intensity B, of cource. Although LPPs are not considered to have as strong B as magnetars, this may not be a genetical difference between them. Actually, as shown in Figure 6.8, the dipole field of magnetars calculated with eq. 2.7 clearly decreases with their age, in agreement with the basic assumption that magnetars shine by consuming their magnetic energies. Then, in 10^{3-4} kyr (= the estimated LPP ages), the field strength of magnetars will have decreased to $\sim 10^{13}$ G, which is close to the values of LPPs. This inspires us of a hypothesis that NSs are born with various field intensities from $\sim 10^{12}$ G up to $\sim 10^{15}$ G, and magnetars and LPPs are the same class of NSs that carries the strongest end of the distribution, differing only in their birth environment (binary or single).

Table 6.1: Comparison between LPPs and magnetars.

Properties	LPPs	Magnetars
System	Binaries	Isolated
Mangetic field strength (G)	10^{13} or higher	10^{14-15}
Age (kyr)	$<10^{3-4}$	$\lesssim$100
Association with SNR	No in 5 objects	3-4 in $\sim$20 sources
Energy source	Accretion	Magnetic
Burst activity	No	High in younger sources

If we employ the above hypothesis, a scenario as illustrated in Figure 6.9 can be constructed. When an NS with strong B ($\sim 10^{15}$ G) is born, it may evolve along two separate tracks, depending on whether it is binary of isolated.

1. Birth in a binary system

   Immediately after the birth, the NS should show similar properties to typical magnetars. Because the strong B prevents stellar winds from the primary star to accrete onto the NS, so that the system remains X-ray faint (except the magnetically drive activities), as long

as $r'_{\rm A} > r_{\rm B}$ holds. Meantime, the angular momentum of the NS is transfered to the stellar winds very effectively via magnetic propeller effects, thus making $P_{\rm s}$ extremely long.

As shown in Figure 6.8, B decays with time and becomes 10^{13} G at ∼100-1000 kyr. Then, $r'_{\rm A}$ gradually decreases, and become $< r_{\rm B}$ where accretion starts. After , the NS will acquire the properties of LPPs. In this process, LPPs do not generally show the magnetar-like burst activity because they are older than typical magnetars.

2. Birth as an isolated NS.

   The object becomes a typical magnetars. Some magnetars are in fact observed in SNRs, and they are really young (Tian & Leahy 2008, Sasaki et al. 2004).

   As the NS becomes older, the activity and X-ray emission become weaker because of the object is not accreting. Finally, the object stops emitting strong X-rays and becomes undetectable.

If this scenario is correct, the apparent gap at $B = 10^{13-14}$ G seen in the magnetic field distribution of Figure 1.1 is likely to be an artifact caused by selection effects. If the object is isolated, its activity will decreases as B decays from 10^{14} G to 10^{13} G, and hence will become more difficult to detect as magnetars. If, instead, the object is in a binary system, the accretion will not start before B has decayed to 10^{13} G or lower. Thus, objects with $B = 10^{13-14}$ G are intrinsically difficult to detect, regardless of their environment.

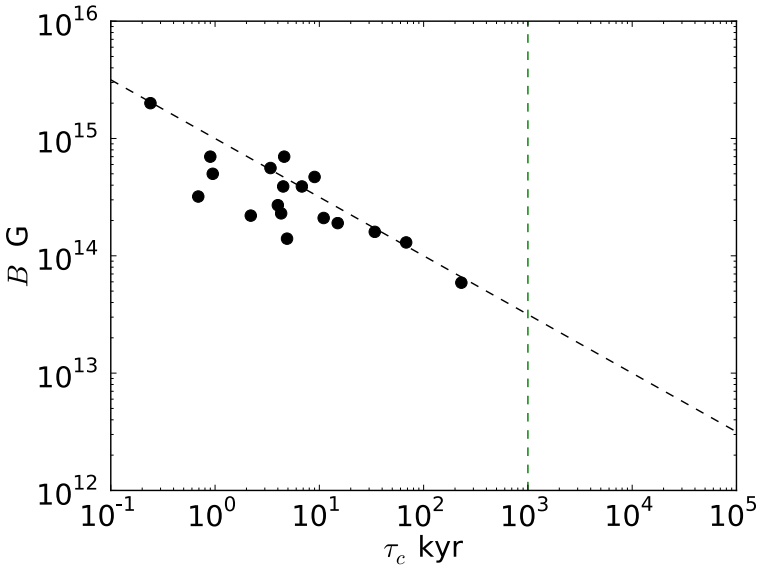

Figure 6.8: A correlation between characteristic age and B of magnetars calculated from the McGill catalog. Black dotted line indicates the bet-fitted power-law ($B \propto \tau_{\rm c}^{1/2}$)results and green the typical life time of high-mass stars (1000 kyr).

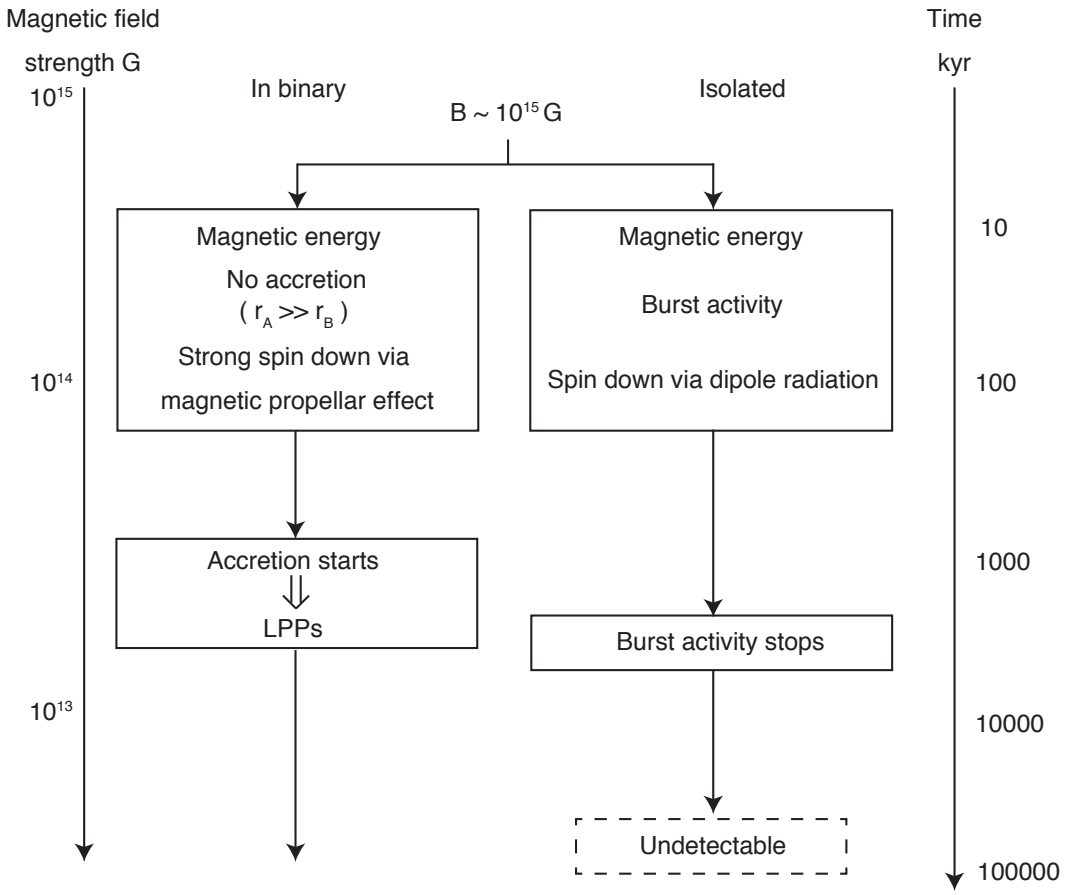

Figure 6.9: A schematic block diagram of possible evolution of NSs born with $B \sim 10^{15}$ G. The evolution of B and the system age are show on the left and right ordinate, respectively.

Chapter 7

CONCLUSION

In the present thesis, we analyzed 42 *Suzaku* data sets of 25 BXPs, mainly from the viewpoint of their magnetic field strength. The derived results can be summarized in the following 5 points.

1. Among BXPs, LPPs including 5 in out sample are clearly different. In addition to their defining properties of longer $P_{\rm s}$ ($\gtrsim 10^3$ s), LPPs have systematically lower luminosities, low energy dependent but high pulse fractions, and harder spectra with two peeks (at ∼20 keV and ∼80 keV, 4U 0352+30 and 4U 0114+65), as compared to the other objects. In addition, the Fe-K line-producing matter is more isotropically distribution around LPPs than around the others.

2. We estimate that LPPs have stronger magnetic field ($B \sim 10^{13}$ G) than the others. This is because some properties of LPPs can be explained by extrapolating B-dependences of these parameters (calibrated using BXPs showing CRSFs) toward higher values of B.

3. The observed properties of LPPs can be all explained consistently and naturally by presuming that they have $B \sim 10^{13}$ G, and hence they are in condition of $r'_{\rm A} \sim r_{\rm B} \sim r_{\rm co}$.

4. Some long period pulsars should fill in the X-ray observational gap between 10^{12} G and 10^{15} G in the measured B-distribution of BXPs, and are considered to provide a missing link between typical BXPs (10^{12} G) and magnetars (10^{15} G). The gap is possibly caused by selection effects that makes if difficult to detect or identify that such high-field binary NSs.

5. We can consistently explain LPPs and magnetars (with 10^{14-15} G), by assuming that new-born NSs have a B-distribution up to $\sim 10^{15}$ G, and the field decays in 10^6 yr down to $\sim 10^{13}$ G, or lower.

These results are expected to give a high impact on the study of X-ray pulsars.

Acknowledgement

I would like to express my best gratitude to my supervisor Prof. Kazuo Makishima for leading me with enthusiasm and perseverance. I am proud of working with him for five years and feeling his devotion to physics. Not only for astrophysics, he taught me many things about not only astrophysics but also experimental techniques. Especially, I stand out the stories of past satellite mission in my memory and study difficulty of the satellite mission. Outside of life in laboratory, ii is very good memory that we enjoyed to climb Mt. Makihata and playing ski at Hokkaido or Iwate.

I wish to thank my colleagues, Dr. Soki Sakurai and Dr. Toshio Nakano. For five yeas, they helped me very kindly and I could spend very good life in laboratory. I also thank my senior, Mr. Shunsuke Torii, Mr. Kenta Nakajima, Mr. Hiroyuki Nishioka, and Dr. Hirofumi Noda, and laboratory members, Mr. Hiroaki Murakami, Mr. Shogo Kobayashi, Mr. Kazuma Miyake, Mr. Yuichi Kato, Mr. Ko Ono, Mr. Daigo Umemoto. For SOI experiment, Mr. Yoshihiro Furuta and Ms. Yuki Murota help me greatly and I wish to thank them. I have been supported by many people not only for this thesis but for experiment and I would like to express my gratitude. For this thesis, Dr. Teruaki Enoto in RIKEN greatly helped me and provided me a valuable comments and I enjoyed to discussing with him. Assitant-Prof. Junko S Hiraga in RESCUE give a chance to treat CMOS camera and I could study many things about CCD and CMOS camera. Lect. Kazuhiro Nakazawa teach me many things about many subjects.

Finally, I would like to appreciate my parents, my brother and my grandparents living in Akita. They help my life and give a chance to accomplish research for five years. I hope to pay my debt to them.

Appendix A

Contours among Parameters of the Modified NPEX Model

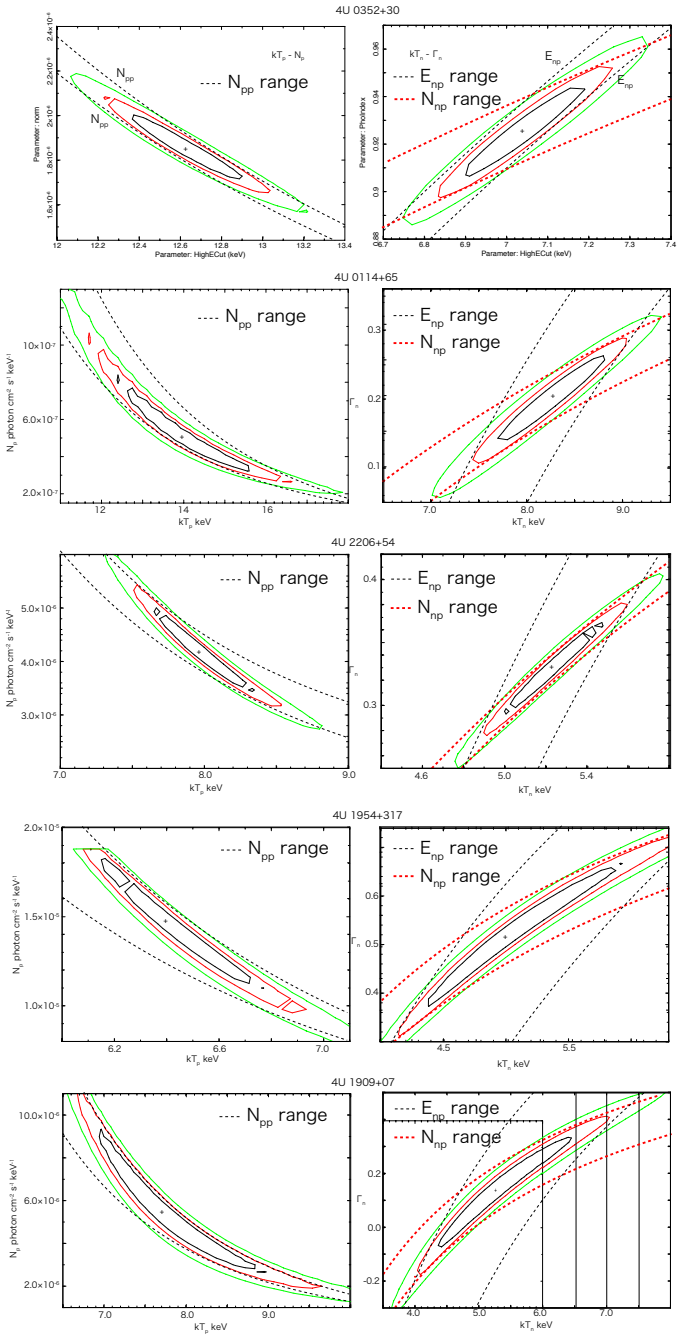

Figure 7.1: Contours between $kT_{\rm p}$ and $N_{\rm p}$ and those between $kT_{\rm n}$ and $\Gamma_{\rm n}$ of 5 objects. The dashed lines on $kT_{\rm p}$ vs. $N_{\rm p}$ map are error range of $N_{\rm pp}$, the black dashed lines on $kT_{\rm n}$ vs. $\Gamma_{\rm n}$ map are error range of $E_{\rm np}$, and the red dashed lines on $kT_{\rm n}$ vs. $\Gamma_{\rm n}$ map are nearly the same as error range of $N_{\rm np}$, Green lines show 99% error, red 90%, and black 64%.

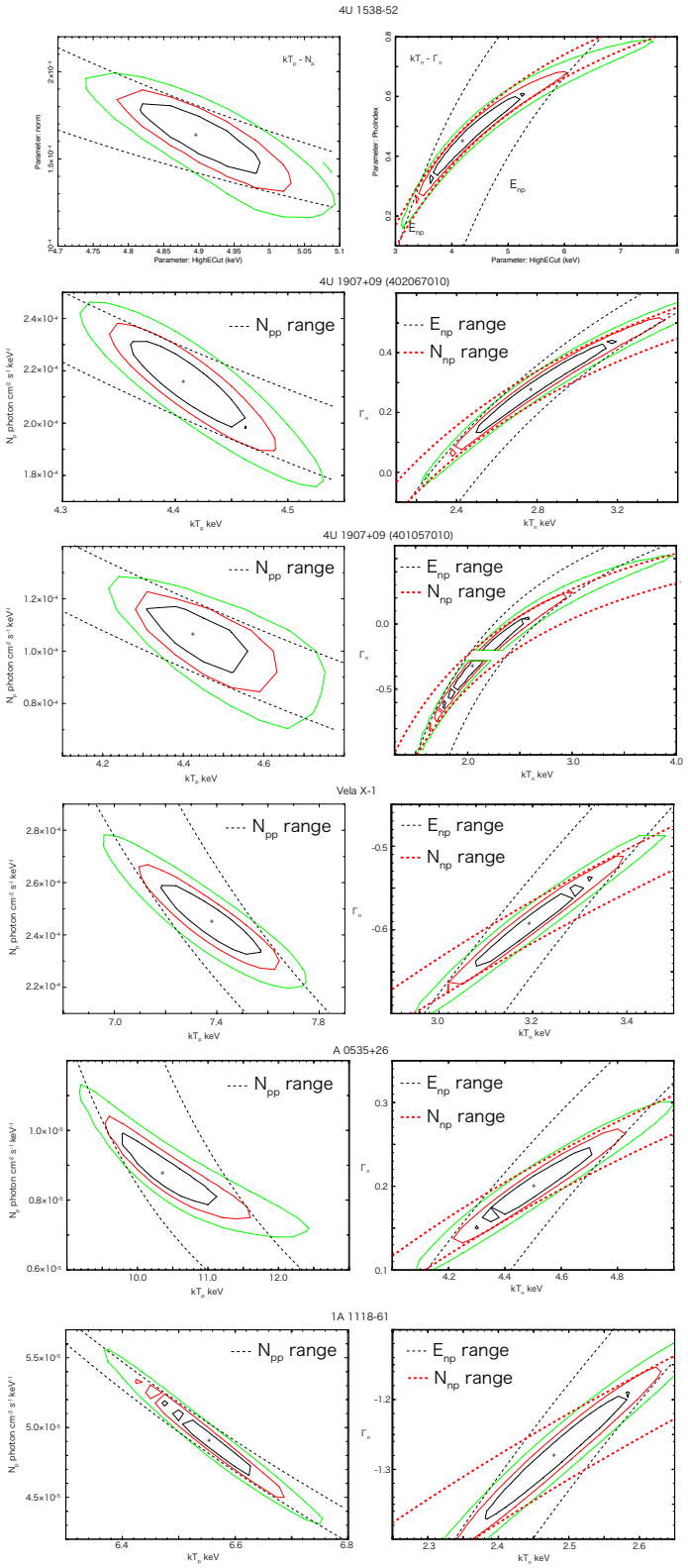

Figure 7.2: Same as 7.1 but for the other 6 low luminosity objects. Colors are also same as 7.1. The lines are also same as the figure

Bibliography

Asami, F., Enoto, T., Iwakiri, W., et al. 2014, Publications of the Astronomical Society of Japan, 66, 44

Audley, M. D., Nagase, F., Mitsuda, K., Angelini, L., & Kelley, R. L. 2006, Monthly Notices of the Royal Astronomical Society, 367, 1147

Basko, . & Sunyaev, . 1976, Monthly Notices of the Royal Astronomical Society, 175, 395

Becker, P. A., Klochkov, D., Schönherr, G., et al. 2012, Astronomy & Astrophysics, 544, A123

Blay, P., Negueruela, I., Reig, P., et al. 2006, Astronomy and Astrophysics, 446, 1095

Camero Arranz, A., Wilson, C. A., Connell, P., et al. 2005, Astronomy and Astrophysics, 441, 261

Chakrabarty, D. 1998, The Astrophysical Journal, 492, 342

Clark, G. W., Woo, J. W., Nagase, F., Makishima, K., & Sakao, T. 1990, The Astrophysical Journal, 353, 274

Cowley, A. P., Schmidtke, P. C., Hutchings, J. B., & Crampton, D. 2003, The Astronomical Journal, 125, 2163

Cox, N. L. J., Kaper, L., Foing, B. H., & Ehrenfreund, P. 2005, Astronomy and Astrophysics, 438, 187

Di Salvo, T., Burderi, L., Robba, N. R., & Guainazzi, M. 1998, The Astrophysical Journal, 509, 897

Doroshenko, V., Santangelo, A., Kreykenbohm, I., & Doroshenko, R. 2012, Astronomy & Astrophysics, 540, L1

Doroshenko, V., Santangelo, A., & Suleimanov, V. 2011, Astronomy & Astrophysics, 529, A52

Duncan, R. C. & Thompson, C. 1992, The Astrophysical Journal, 392, L9

Ebisawa, K., Day, C. S. R., Kallman, T. R., et al. 1996, Publications of the Astronomical Society of Japan, 48, 425

Endo, T., Nagase, F., & Mihara, T. 2000, Publications of the Astronomical Society of Japan, 52, 223

Enoto, T., Sasano, M., Yamada, S., et al. 2014, The Astrophysical Journal, 786, 127

Enoto, ., Makishima, ., Terada, ., et al. 2008, Publications of the Astronomical Society of Japan

Finger, M. H., Ikhsanov, N. R., Wilson-Hodge, C. A., & Patel, S. K. 2010, The Astrophysical Journal, 709, 1249

Finger, M. H., Koh, D. T., Nelson, R. W., et al. 1996, Nature, 381, 291

Fukazawa, Y., Mizuno, T., Watanabe, S., et al. 2009, Publications of the Astronomical Society of Japan, 61, S17

Fürst, F., Pottschmidt, K., Kreykenbohm, I., et al. 2012, Astronomy & Astrophysics, 547, A2

Ghosh, P. & Lamb, F. K. 1978, The Astrophysical Journal, 223, L83

Giacconi, R., Gursky, H., Kellogg, E., Schreier, E., & Tananbaum, H. 1971, The Astrophysical Journal, 167, L67

Giles, A. B., Swank, J. H., Jahoda, K., et al. 1996, The Astrophysical Journal, 469, L25

Heindl, W. A., Coburn, W., Gruber, D. E., et al. 2001, The Astrophysical Journal, 563, L35

Hemphill, P. B., Rothschild, R. E., Markowitz, A., et al. 2014, The Astrophysical Journal, 792, 14

HEWISH, A., BELL, S. J., PILKINGTON, J. D. H., SCOTT, P. F., & COLLINS, R. A. 1968, Nature, 217, 709

Hinkle, K. H., Fekel, F. C., Joyce, R. R., et al. 2006, The Astrophysical Journal, 641, 479

Hung, L.-W., Hickox, R. C., Boroson, B. S., & Vrtilek, S. D. 2010, The Astrophysical Journal, 720, 1202

Inoue, H. 1985, Space Science Reviews, 40, 317

Iwakiri, W. B., Terada, Y., Mihara, T., et al. 2012, The Astrophysical Journal, 751, 35

Janot-Pacheco, ., Ilovaisky, ., & Chevalier, . 1981, Astronomy and Astrophysics, 99, 274

Kallman, T. R. & McCray, R. 1982, The Astrophysical Journal Supplement Series, 50, 263

Kaper, L., van der Meer, A., & Najarro, F. 2006, Astronomy and Astrophysics, 457, 595

Kendziorra, ., Kretschmar, ., Pan, ., et al. 1994, Astronomy and Astrophysics (ISSN 0004-6361), 291

Kokubun, M., Makishima, K., Takahashi, T., et al. 2007, Publications of the Astronomical Society of Japan, 59, S53

Koyama, K., Tsunemi, H., Dotani, T., et al. 2007, Publications of the Astronomical Society of Japan, 59, S23

Maitra, C. & Paul, B. 2013a, The Astrophysical Journal, 771, 96

Maitra, C. & Paul, B. 2013b, The Astrophysical Journal, 763, 79

Makishima, K., Mihara, T., Ishida, M., et al. 1990, The Astrophysical Journal, 365, L59

Makishima, K., Mihara, T., Nagase, F., & Tanaka, Y. 1999, The Astrophysical Journal, 525, 978

Makishima, K., Ohashi, T., Sakao, T., et al. 1988, Nature, 333, 746

Masetti, N., Orlandini, M., Palazzi, E., Amati, L., & Frontera, F. 2006, Astronomy and Astrophysics, 453, 295

Meszaros, P. & Nagel, W. 1985, The Astrophysical Journal, 298, 147

Mihara, T., Makishima, K., Kamijo, S., et al. 1991, The Astrophysical Journal, 379, L61

Mihara, . 1995, Ph.D. thesis

Mitsuda, K., Bautz, M., Inoue, H., et al. 2007, Publications of the Astronomical Society of Japan, 59, S1

Morel, T. & Grosdidier, Y. 2005, Monthly Notices of the Royal Astronomical Society, 356, 665

Mowlavi, N., Kreykenbohm, I., Shaw, S. E., et al. 2006, Astronomy and Astrophysics, 451, 187

Nagase, . 1989, Astronomical Society of Japan, 41, 1

Nagase, ., Hayakawa, ., Sato, ., Masai, ., & Inoue, . 1986, Astronomical Society of Japan, 38, 547

Naik, S., Dotani, T., Terada, Y., et al. 2008, The Astrophysical Journal, 672, 516

Naik, S., Maitra, C., Jaisawal, G. K., & Paul, B. 2013, The Astrophysical Journal, 764, 158

Naik, S., Paul, B., & Ali, Z. 2011a, The Astrophysical Journal, 737, 79

Naik, S., Paul, B., Kachhara, C., & Vadawale, S. V. 2011b, Monthly Notices of the Royal Astronomical Society, 413, 241

Nakajima, M., Mihara, T., & Makishima, K. 2010, The Astrophysical Journal, 710, 1755

Nakajima, M., Mihara, T., Makishima, K., & Niko, H. 2006, The Astrophysical Journal, 646, 1125

Negoro, ., Sugizaki, ., Krimm, ., et al. 2014, The Astronomer's Telegram

Negueruela, I., Israel, G. L., Marco, A., Norton, A. J., & Speziali, R. 2003, Astronomy and Astrophysics, 397, 739

Nishimura, O. 2008, The Astrophysical Journal, 672, 1127

Nishiuchi, M., Koyama, K., Maeda, Y., et al. 1999, The Astrophysical Journal, 517, 436

Odaka, H., Khangulyan, D., Tanaka, Y. T., et al. 2013, The Astrophysical Journal, 767, 70

Odaka, H., Khangulyan, D., Tanaka, Y. T., et al. 2014, The Astrophysical Journal, 780, 38

Orlandini, M., Dal Fiume, D., Frontera, F., et al. 1998, The Astrophysical Journal, 500, L163

Parkes, ., Murdin, ., & Mason, . 1980, Monthly Notices of the Royal Astronomical Society, 190, 537

Reig, ., Chakrabarty, ., Coe, ., et al. 1996, Astronomy and Astrophysics

Reynolds, ., Bell, ., & Hilditch, . 1992, Monthly Notices of the Royal Astronomical Society (ISSN 0035-8711), 256, 631

Reynolds, ., Quaintrell, ., Still, ., et al. 1997, Monthly Notices of the Royal Astronomical Society, 288, 43

Riquelme, M. S., Torrejón, J. M., & Negueruela, I. 2012, Astronomy & Astrophysics, 539, A114

Rivers, E., Markowitz, A., Pottschmidt, K., et al. 2010, The Astrophysical Journal, 709, 179

Santangelo, ., delSordo, ., Segreto, ., et al. 1998, Astronomy and Astrophysics

Sasaki, M., Plucinsky, P. P., Gaetz, T. J., et al. 2004, The Astrophysical Journal, 617, 322

Sasano, M., Makishima, K., Sakurai, S., Zhang, Z., & Enoto, T. 2014, Publications of the Astronomical Society of Japan, 66, 35

Serlemitsos, P. J., Soong, Y., Chan, K.-W., et al. 2007, Publications of the Astronomical Society of Japan, 59, S9

Sherwood, . & Plaut, . 1975, Symposium sponsored by the International Astronomical Union Dordrecht

Shrader, C. R., Sutaria, F. K., Singh, K. P., & Macomb, D. J. 1999, The Astrophysical Journal, 512, 920

Staubert, R., Shakura, N. I., Postnov, K., et al. 2007, Astronomy and Astrophysics, 465, L25

Steele, I. A., Negueruela, I., Coe, M. J., & Roche, P. 1998, Monthly Notices of the Royal Astronomical Society, 297, L5

Suchy, S., Fürst, F., Pottschmidt, K., et al. 2012, The Astrophysical Journal, 745, 124

Suchy, S., Pottschmidt, K., Rothschild, R. E., et al. 2011, The Astrophysical Journal, 733, 15

Takahashi, T., Abe, K., Endo, M., et al. 2007, Publications of the Astronomical Society of Japan, 59, S35

Telting, J. H., Waters, L. B. F. M., Roche, P., et al. 1998, Monthly Notices of the Royal Astronomical Society, 296, 785

Terada, Y., Mihara, T., Nakajima, M., et al. 2006, The Astrophysical Journal, 648, L139

Terada, ., Enoto, ., Miyawaki, ., et al. 2008, Publications of the Astronomical Society of Japan

Tian, W. W. & Leahy, D. A. 2008, The Astrophysical Journal, 677, 292

Torrejón, J. M., Schulz, N. S., Nowak, M. A., & Kallman, T. R. 2010, The Astrophysical Journal, 715, 947

Truemper, J., Pietsch, W., Reppin, C., et al. 1978, The Astrophysical Journal, 219, L105

Verrecchia, F., Israel, G. L., Negueruela, I., et al. 2002, Astronomy and Astrophysics, 393, 983

Voges, W., Pietsch, W., Reppin, C., et al. 1982, The Astrophysical Journal, 263, 803

Westerlund, . 1997, Book

Wheaton, W. A., Doty, J. P., Primini, F. A., et al. 1979, Nature, 282, 240

White, N. E., Swank, J. H., & Holt, S. S. 1983, The Astrophysical Journal, 270, 711

Yamada, S., Makishima, K., Nakazawa, K., et al. 2011, Publications of the Astronomical Society of Japan, 63, S645

Yamamoto, T., Mihara, T., Sugizaki, M., et al. 2014, Publications of the Astronomical Society of Japan, 66, 59

Yamamoto, T., Sugizaki, M., Mihara, T., et al. 2011, Publications of the Astronomical Society of Japan, 63, S751